Gran Sasso Science Institute

Scuola Internazionale Superiore di Studi Avanzati

The XENON project: backgrounds and new results

PhD thesis

submitted August 15, 2017

PhD Candidate

Federica Agostini

Advisor

Prof. Gabriella Sartorelli
Department of Physics and Astrophysics, University of Bologna and INFN-Bologna, Bologna, Italy

Tutors

Dr. Marco Selvi
INFN-Bologna, Bologna, Italy

Dr. Marco Garbini
INFN-Bologna, Bologna and Centro Fermi, Rome, Italy

Gran Sasso Science Institute

Ciclo XXIX

Abstract

Experimental observations tell us that the biggest amount of mass constituting the universe does not absorb or emit electromagnetic radiation; that is the reason why it is called *Dark Matter* (DM). The evidences for the existence of DM are based on gravitational effects, such as anomalies in rotation curves of spiral galaxies, gravitational lensing, CMB anisotropies, *etc.* A consistent theoretical model of particles that includes DM has not been developed yet, thus a DM candidate is generally called *Weakly Interacting Massive Particle* (WIMP).

There are mainly two dark matter detection techniques: indirect search, based on tagging the particles produced by the self-annihilation of WIMPs, and direct search, which consists in identifying elastic scatterings of WIMPs off target nuclei. The XENON project is a DM direct search detector, located at the Gran Sasso National Laboratories. The experiment is based on a xenon dual-phase (Liquid/Gas) Time Projection Chamber (TPC), exploiting both scintillation and ionization signals to identify and discriminate impinging WIMP particles from background. XENON100, operating up to 2016, published in 2012 the best exclusion limit, at that time, for spin-independent WIMP-nucleon elastic interactions, with a minimum cross section of 2.0×10^{-45}cm^2 for a WIMP mass of 55 GeV/c^2, at 90% confidence level. Moreover, from a combined analysis over three runs, a long period of 477 live days of data has improved the sensitivity by almost a factor 2. The subsequent experiment XENON1T is the first multi-ton scale dark matter direct search detector to date, and, on May 18^{th} 2017, the Collaboration released the results from the first science run, setting the limit for spin-independent WIMP-nucleon elastic scattering cross section, to 7.7×10^{-47}cm^2 for a 35 GeV/c^2 WIMP mass at 90% confidence level. This limit is, at the moment, the best one.

The work of this thesis is based both on XENON100 and XENON1T experiments. In XENON100 a study on the *electromagnetic background*, due to electrons or gammas scattering off xenon electrons, has been developed. The calibration data from Xe activation lines by neutron inelastic scattering, ^{232}Th and CH_3T sources have been compared with the Monte Carlo (MC) simulations. In particular, when a particle interacts with the detector, releases a certain amount of energy, which is converted into photons and electrons; the number of photons and electrons emitted per unit of energy is called *light* and *charge yield* respectively. The model used to predict the light and charge yield is Noble Element Simulation

Technique (NEST) and consists of a phenomenological description of the xenon response to an ionizing radiation, through a collection of target-related parameters obtained by fitting up-to-date experimental results. A refined matching between MC and measured data has been achieved within a Bayesian statistical approach. For this purpose, the light and charge yield obtained by NEST have been improved by using the data from tritium calibration as input. That topic is of fundamental importance for XENON1T, where the large self-shielding power of the liquid xenon does not allow to reach the inner *fiducial volume* through usual calibration sources located outside the TPC.

In the case of XENON1T, an active *Muon Veto* (MV) has been employed in order to reduce the muon-induced neutron background. It consists of a cylindrical tank, containing the TPC, filled with water and equipped with 84 photomultiplier tubes (PMTs), to tag the Cerenkov light emitted from a muon, or its daughters, crossing the water tank. I took care of the MV system since the very beginning, from the installation of the PMTs inside the water tank to its operation in the final state. Moreover, a muon analysis to tag neutron-induced muon events over the first science run of data is object of this work. 63 single scatterings off xenon nuclei inside 1 ton fiducial volume have been found in the low energy region, that is of interest for WIMP search; no one of them has been vetoed by MV, but they have been discriminated as electromagnetic background.

Contents

Introduction

From experimental observations, it is known, since several decades, that only ∼4% of the Universe is constituted by ordinary matter, *i.e.* luminous and baryonic. The rest of the matter is in form of *dark energy* (with an amount of 72%) and *Dark Matter* (DM, around 24%). The non-luminous DM does not absorb or emit electromagnetic radiation, but interacts only through gravitational forces and, likely, weak forces. Thus, DM would be constituted by neutral and massive particles. Experimental evidences for the existence of dark matter, described in Section 1.1, are based on gravitational interactions with big masses in the Universe. An example is given by the rotational velocity of spiral galaxies, gravitational lensing effect, redshift measurements of the galaxy clusters, *etc.* Those experimental observations have revealed anomalies that can only be explained by a deviation from the theory of gravity, or by assuming the existence of a large amount of non-luminous massive particles.

A consistent theoretical model of particles which includes dark matter requires an extension of the Standard Model and has not been developed yet. Thus, a dark matter candidate is generally called *Weakly Interacting Massive Particle* (WIMP), meaning it is massive, neutral and can interact through gravitational and weak forces only. As introduced in Section 1.2, when the primordial Universe expanded and cooled, the production and annihilation rate of particles was suppressed and their relic abundance was fixed (*thermal freeze-out*). Therefore, in order to accomplish the correct abundance of DM, the dark matter cross section would be in the electroweak scale and mass in the range of GeV. One of the best dark matter candidates is the *neutralino*, the lightest stable particle defined in the frame of the Supersymmetry; it can have a mass in the range of 100 GeV and 1 TeV, and interacts weakly. Neutralino is a new particle predicted independently in a theory beyond the Standard Model and follows the requirement for a WIMP candidate. Anyway, up to date, no experimental result supports the existence of Supersimmetry.

We can mainly distinguish two dark matter detection techniques, explained in Section 1.3: indirect search, based on tagging the particles produced by the decay of self-annihilation of WIMPs, and direct search, which consists in identifying elastic scatterings of WIMPs off target nuclei. As already mentioned, the cross section for dark matter interactions is extremely small, in the weak scale and the expected event rate is also

very low (around 1 event/ton/year). For this reason, in order to direct detect dark matter, big detectors with a high amount of target mass are required. Moreover, the active mass has to be ultra pure, the intrinsic radioactivity of detector materials has to be very low and also the environment radioactivity, where the detector is placed, has to be mantained at the minimum level. In order to reduce the background from cosmic rays, the direct dark matter detectors are typically located in underground laboratories.

Noble liquids based detectors are common in astroparticle physics experiments due to their properties of being pure, chemically inert and excellent insulators. Among the other features, xenon is a perfect choice for dark matter search thanks to its high atomic mass and density, which makes it a very efficient media to stop penetrating radiation, reduce external background and increase the elastic WIMP-nucleus scattering cross section. In Chapter 2 are introduced the main properties of xenon, focusing on its response to incident radiation and its usage as target detection media.

The XENON project is a dark matter direct detector located at the Gran Sasso National Laboratories (LNGS), below 1.4 km of rock, providing about 3600 meters of water equivalent shielding that reduces the muon flux by a factor 10^6. The experiment is based on a xenon dual-phase (Liquid/Gas) Time Projection Chamber (TPC). It exploits both scintillation and ionization signals to calculate the recoiling energy released by an impinging particle scattering off liquid xenon target and to discriminate nuclear from electron recoil background. The detection principle of a direct dark matter experiment using a dual-phase TPC filled with xenon is presented in Section 3.1.

The prototype of the XENON project, XENON10, filled with 15 kg of xenon, published in 2008 the best limits at the time for a WIMP-nucleon elastic scattering. The subsequent detector XENON100, 161 kg of target mass, run from 2008 to 2016 and set in 2012 the most stringent limit for spin-independent elastic WIMP-nucleon scattering, with a minimum cross section of 2.0×10^{-45}cm^2 for a WIMP mass of 55 GeV/c^2, at 90% confidence level (C.L.). Moreover, from a combined analysis over three runs, a long period of 477 live days of data has improved the sensitivity. In the fall of 2013 the design and construction of XENON1T has started. With 3.3 tons of target mass, it is the first multi-ton scale direct dark matter detector using xenon to date. This year, 2017, XENON1T has released the results from the first science run, setting the best limit for spin-independent WIMP-nucleon elastic scattering, to 7.7×10^{-47}cm^2 cross section for a 35 GeV/c^2 WIMP mass at 90% C.L. Most of the subsystems of the XENON1T experiment have been designed such that it can easily be upgraded to XENONnT, an instrument featuring a larger target mass of liquid xenon ($\sim$ 7 tons). The detector design of the XENON project, together with the experimental results, is described in Section 3.3.

The work of this thesis is based both on XENON100 and XENON1T.

In XENON100 a detailed study on the *electromagnetic background*, due to electrons or gammas scattering off xenon electrons and inducing Electron Recoils (ERs), has been developed. Low energy Nuclear Recoils (NRs), due to neutrons or WIMPs scattering off xenon nuclei, delimit a region of interest for dark matter search. Since xenon responds differently to ERs and NRs, we have an efficient discrimination parameter to reject electromagnetic background. Anyway, the fraction of ERs falling into the nuclear recoil *discrimination band* can not be discarded and represents a dangerous background, subject of this work. Moreover, the electromagnetic background is of fundamental importance for XENON1T, in which the large self-shielding power of liquid xenon does not allow to reach the inner fiducial volume through usual ER calibration sources located outside the TPC.

In Section 4.1 a Monte Carlo (MC) simulation that predicts the electromagnetic background in XENON100 has been developed and described in detail. The model used to predict the number of photons, or *light yield* and electrons, or *charge yield* emitted by a particle interacting with the detector is called Noble Element Simulation Technique (NEST). It consists in a phenomenological description of the xenon response to an ionizing radiation, through a collection of target-related parameters obtained by fitting up-to-date experimental results. The MC has been validated through a comparison with ER calibration data in XENON100. In particular, we have simulated the detector response to

- gamma rays from Xe excited isotopes activated by neutron inelastic scattering from AmBe (Section 4.2);
- low energy Compton electrons from ^{232}Th source, uniformly distributed in the energy range of interest for WIMP search (Section 4.3);
- electrons from CH_3T (tritium), which dissolves uniformly in xenon inside the TPC and decays with endpoint 18.6 keV (Section 4.4).

The quantities considered are mainly the light yield and the ER band.

The conclusions drawn from this work suggest us to tune the MC model for ERs. Thus, a refined study on the electromagnetic background has been developed within a Bayesian statistical approach, presented in Chapter 5. The idea is to build a phenomenological parameterization of the photon yield and its fluctuation, as function of the energy released in the detector (*photon yield map*). The input model used to predict the number of photons and electrons, produced by the interaction of impinging radiations with target material, is again NEST. Then, the conversion between photons and electrons into measurable signal is closely related to the physics of the detector and is part of the likelihood. Finally, using a Markov Chain Monte Carlo (MCMC) scheme we converged to a posterior distribution for the photon yield map. In particular, the MCMC has been fed with data coming from the previous tritium calibrations.

The XENON1T experiment has been meant to improve the sensitivity to WIMP interactions set by the former XENON100 by about two order of magnitude. For this reason, about 10 times the liquid xenon target mass of XENON100 is required in XENON1T. Also, a careful control of the background is needful; very low radioactive materials have been used in building the detector, an efficient purification system for the liquid xenon is employed, an ultra pure cylindrical water shield (or *water tank*) is installed around the TPC with the aim of suppressing the neutron and gamma flux from rock radioactivity, *etc.* In particular, the muon-induced neutrons, due to muon spallation of nuclei or electromagnetic and hadronic cascades generated by muons, have enough energy to reach the TPC and produce the same signal as expected by WIMPs. In order to tag those events the water tank has been equipped with 84 Hamamatsu photomultipliers and acts as a Cherenkov detector, the *Muon Veto* (MV), described in Section 6.1. I have been responsible of the MV system since the very beginning, from the installation of the PMTs inside the water tank in 2014, to the hardware setup, calibrations, trigger, *etc.*, up to its operation in the final state. A synchronization among MV and TPC using the fast muons which crosses both the water tank and the TPC has been accomplished and reported in Section 6.2. Finally, a muon analysis to tag muon-induced neutron events is described in detail in Section 6.3, and is part of the results released by the the XENON1T Collaboration for the first science run of 34.2 live days of data, the *Science Run 0*, acquired between November 2016 and January 2017.

Chapter 1

Particle Dark Matter

The Dark matter (DM) is one of the most challenging topics in the last years, studied in astronomy, cosmology and astroparticle physics. It is a kind of matter that does not emit electromagnetic radiation, but interact trough gravitational and, likely, weak forces only; this means it can not be directly "seen". The way to prove the existence of dark matter is thus through the effect of gravitational interactions with big masses in the universe, such as anomalies in the rotation curves of spiral galaxies, lensing effects, CMB anisotropies, *etc.*

In 1933 the Swiss astrophysicist Fritz Zwicky [1] found the first evidence of DM, while observing the motion of Coma and Virgo clusters. In fact, the velocity of the galaxies were about one order of magnitude higher than the expected one, estimated from the total luminous mass, as if there was a non-visible amount of mass acting on the gravitational field. The explanation to such effect was the introduction of an high massive invisible object, gravitationally interacting, baptized by the astrophysicist as *dark matter*.

Theoretical efforts have been done in order to find the proper model of particles to include dark matter, that requires an extension of the Standard Model. Some dark matter candidates have been generally called *Weakly Interacting Massive Particles* (WIMP), meaning they interact through gravitational and weak forces only (*i.e.* Weakly Interacting) and are massive (*i.e.* Massive Particles). One of the most favored dark matter candidate is the *neutralino*, a particle defined in the frame of the Supersymmetry. Several experiments have been desined so far with the aim of discovering dark matter. The detection techniques are intended to inspect different regions in the DM parameter space, and basically consist of production at accelerators, indirect and direct detection.

1.1 Evidence for the existence of Dark Matter

The experimental evidence to the existence of dark matter consist of gravitational effects that are not due to luminous objects, in the field of astrophysics and cosmology.

1.1.1 Galaxy rotation curves

The quantity of matter in the universe can be estimated by the measurement of the speed of stars and galaxies. It also allows to retrieve the local density of dark matter $\rho(r)$.

In spiral galaxies with a symmetric matter distribution, where M is the mass of the galaxy, mostly contained in the center, the rotation speed $v(r)$ scales with $r^{-1/2}$, where r is the distance from the center of the galaxy. In fact, by applying the Virial Theorem to a gravitational system, we have:

$$\langle \frac{GM(r)}{r^2} \rangle = \langle \frac{v^2(r)}{r} \rangle \,, \quad \langle v(r) \rangle = \left(\frac{GM(r)}{\langle r \rangle} \right)^{1/2} , \tag{1.1}$$

where G is the gravitational constant; $M(r)$ is the mass contained inside a radius r and has the following distribution in a galaxy with a density $\rho(r)$:

$$M(r) = 4\pi \int_0^R \rho(r) r^2 dr \,. \tag{1.2}$$

In order to verify the rotation curve of a spiral galaxy, *i.e.* its speed at a certain distance from the center, the Doppler effect is used: the galaxy disk moving away from the observer emits a red-shifted spectrum, while the galaxy disk moving toward the observer emits a blue-shifted spectrum. Figure 1.1 shows the rotation curve of the dwarf spiral galaxy NGC6503 [2]; it does not agree with expectation from theory. In fact, the central part of the galaxy rotates as a rigid body (*i.e.* the rotation speed scales with r up to about 3 kpc), while slightly outside the center one can notice a peak in the rotation speed due to a central group of stars. Finally, far away from the center the rotation speed becomes constant, despite the quantity of baryonic matter is almost negligible. As a conclusion, from experimental results it has been discovered that the galaxy mass increases with the distance from the center and its density scales with r^{-2}.

Thus, based on experimental results on the galaxy rotation curves, there is a no visible halo of matter contributing to the galaxy mass, the dark matter. From this observation one can also retrieve the dark matter density. In fact, since the rotation speed is constant at high distances from the center, while it scales with r close to the center, $\rho(r) \propto r^{-2}$ at

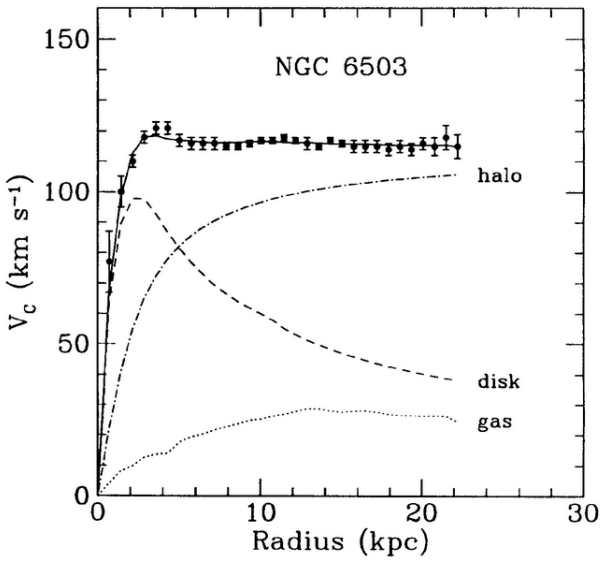

Figure 1.1: Rotation curve of the dwarf spiral galaxy NGC6503 [2]. The dashed line (disk) is the shape expected from theory, the fitted dots are the experimental results, while *halo* is the invisible mass required to match the experimental results.

high distances and $\rho(r) \propto \rho_0$ at small distances; then, the dark matter density distribution can be parametrized as:

$$\rho(r) = \frac{\rho_0}{1 + (r/a)^2}\,, \tag{1.3}$$

where ρ_0 is the local dark matter density and a is the size of the galactic center, obtained by experimental fit [3].

Thus, the dark matter is supposed to be spherically distributed around the galactic center. Based on these observations, one can retrieve the local density of DM in the Milky Way galaxy, around $\sim$0.3 GeV/cm^3.

1.1.2 Gravitational lensing

From General Relativity we know that strong gravitational fields bend the space-time, changing the trajectory of the light. The big massive object that causes such effect acts as a refractive lens, for this reason it is called *gravitational lensing*. This phenomenon is often used in astronomy in order to evaluate the intensity of gravitational fields due to galaxies.

The relation between the deflection angle $\Delta\Phi$ of the light, that has an impact parameter b on the gravitational source with mass M, is:

$$\Delta\Phi = \frac{4GM}{b}\,, \tag{1.4}$$

where G is the gravitational constant. For instance, the light passing close to the Sun has impact parameter equal to its radius, $b = r_\odot$ and

$M = M_{\odot}$, and will be deflected with angle $\Delta\Phi \sim 1.75''$. Such effect has been observed for the first time by the astronomer Eddington in 1919 during a total solar eclipse [4]. In fact, the total eclipse acted as screen from the solar light, allowing to determine the apparent position of a star located behind the Sun. The exact location of this star can be directly measured from the Earth, when it stands in the opposite side with respect to its position during the eclipse, and the light is not bended.

Also galaxy clusters, being very massive, can act as gravitational lenses. In 1979 the observation of the Twin QSO, a quasar that appears as two images from the gravitational lensing of the galaxy YGKOW G1, confirmed this effect as due to a galaxy [5]. Moreover, the gravitational lensing in galaxy clusters or quasars can be explained with a big amount of invisible mass interposed between the object and the Earth, the dark matter. The more the image of galaxy clusters or quasars is bend, the higher is the amount of dark matter. Figure 1.2 shows the scheme of gravitational lensing principle and the distorted image of the galaxy cluster Abell 2218 [6].

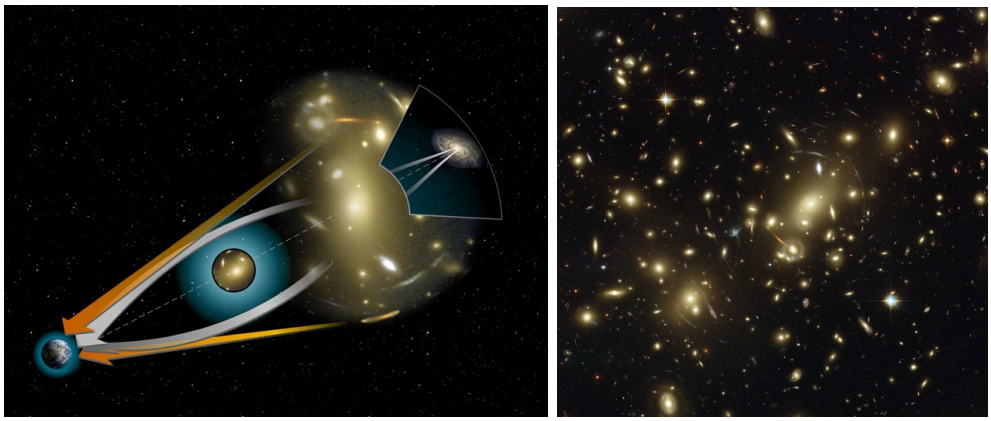

Figure 1.2: Scheme of gravitational lensing principle, where a big massive object bend the space-time changing the trajectory of the light (left) and distorted image of the galaxy cluster Abell-2218 [6] (right).

1.1.3 Bullet cluster

The *bullet cluster* is the collision of two galaxy clusters. Since galaxies are made of stars and hot gasses, during the collision the stellar component is decelerated by the gravitational field of the other cluster, while the two gaseous components behave as a collision particle fluid. The main baryonic mater is in the gas, then, by mapping the hot gas through the emission of X-rays during the galaxy collision, scientists mapped the main baryonic component. Moreover, the distribution of the optical light obtained by the stars in the galaxies, matches that of gravitational potential from the lensing effect. However, stars themselves can not explain gravitational lensing, due to their small mass; thus, there should

be a non-luminous matter in these clusters with the distribution of mass similar to the distribution of stars.

In 2004 it has been measured the collision of the subcluster 1E 0657-558 [7], from which has been observed a discrepancy between the baryonic matter distribution, measured from the X-ray emission and the gravitational field distribution obtained from lensing (Figure 1.3). The separation among the two areas can be explained by the fact that after the collision the hot gas still interact while the dark matter does not decelerate and just follow inertially its initial path. It suggests us that DM has a non-collisional nature and is not in form of gas.

1.1.4 CMB anisotropies

Another strong experimental evidence to the existence of dark matter comes from the Cosmic Microwave Background (CMB) power spectrum measurement of the primordial universe through radiotelescopes. The CMB is made of photons from the early universe, as soon as it has become transparent to the radiation. It happened when the temperature dropped to about 3000 K and electrons recombined with protons emitting photons that had not enough energy to ionize hydrogen.

Before the primordial nucleosynthesis, quantum fluctuations caused a not uniform matter distribution. In particular, the hypothesis is that gravity caused the compression of dark matter, while the the pressure of photons decompressed baryonic matter. When the gravitational pressure became higher than the one of photons, the dark matter decompressed and the baryonic one was compressed. This process affected also the temperature of baryonic matter (increasing with its compression), but not the one of dark matter, that does not interact with photons. The

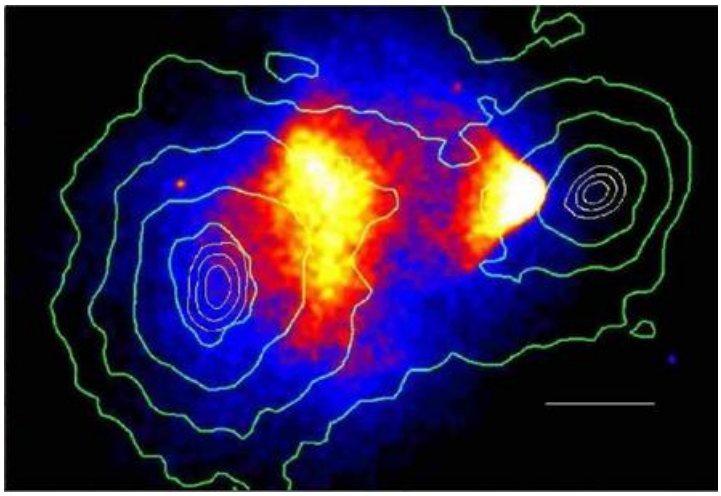

Figure 1.3: Collision of the subcluster 1E 0657-558 [7]. The red object is the baryonic matter measured from X-ray emission and the green curves indicate the gravitational potential measured with gravitational lensing.

CMB, in thermal equilibrium with matter at the time of the recombination, brings information on the anisotropies through the characteristic peak structure of its spectrum. The angular power spectrum of the fluctuations in temperature is obtained by decomposing the anisotropy map (Figure 1.4) into spherical harmonics $Y_{lm}(\theta, \phi)$ as follows:

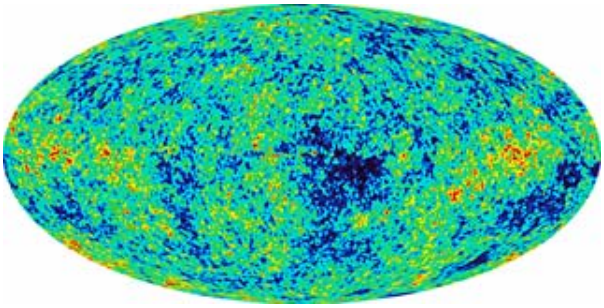

Figure 1.4: Map of the primordial universe, in which the temperature variations have been revealed through the microwaves from CMB.

$$\frac{\delta T}{T}(\theta, \phi) = \sum_{l=0}^{\infty} \sum_{m=-l}^{l} a_{lm} Y_{lm}(\theta, \phi)\,, \tag{1.5}$$

$$\Delta \left(\frac{\delta T}{T} \right)_{\theta} \approx \sqrt{l(l+1)C_l/2\pi}\,, \tag{1.6}$$

where a_{lm} are the complex coefficients of the spherical harmonics, C_l is their variance and l indicates the multipole moment.

A plot of the temperature angular power spectrum is shown in Figure 1.5 [8]. The amplitude on the CMB do not fit the expectations if consider-

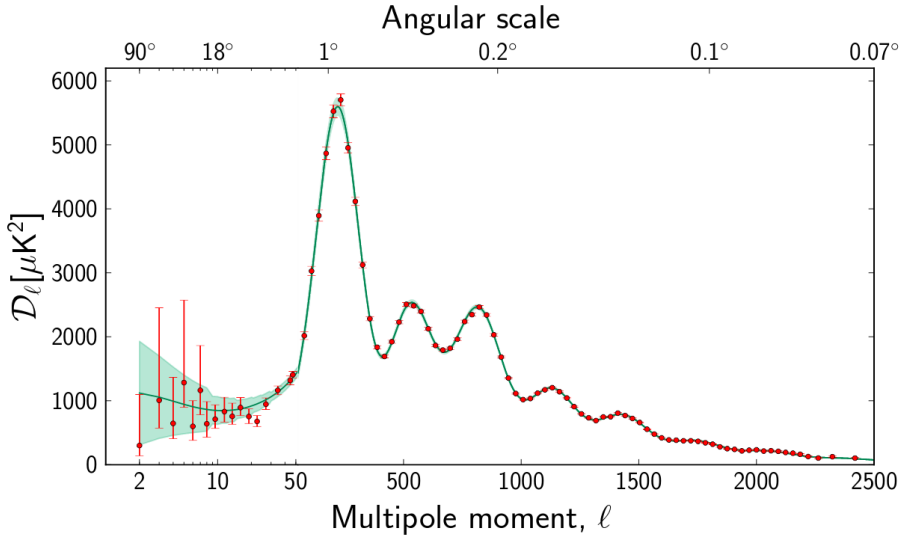

Figure 1.5: The 2013 Planck CMB temperature angular power spectrum [8].

ing the baryonic matter only. With the assumption that the temperature fluctuations would begin well before the ones of the baryonic matter, inducing higher amplitudes in the spectrum at the recombination time, the experimental results on the temperature angular power spectrum would fit the expectations. Then, the hypothesis of the existence of dark matter is very strong. Moreover, from the size and the position of the peaks in the CMB power spectrum, one get information on cosmological parameters, such as the curvature and energy-matter composition of the universe. The abundance of the several component of the universe is:

$$\Omega_\Lambda = 0.707 \pm 0.010\,, \tag{1.7}$$

$$\Omega_m = 0.293^{+0.056}_{-0.010}\,, \tag{1.8}$$

$$\Omega_b h^2 = 0.02211 \pm 0.00034, \tag{1.9}$$

$$\Omega_{DM} h^2 = 0.1162 \pm 0.0020. \tag{1.10}$$

From the values of the cosmological parameters it is clear that the dark energy (Λ) accounts for about 70% of the universe constituents while the majority of the matter content is in the form of non-baryonic dark matter.

1.2 Dark Matter candidates

Since the evidence of the existence of dark matter is based on gravitational interactions only, one could suggest to modify the gravitational laws instead of introducing a dark matter particle. However, any modification to gravitational laws always fails in proving some of the evidence. For instance, the Modified Newtonian Dynamics (MOND) [9] can successfully describe the galactic rotation curves, but can not account for the large scale structure of the cosmos or explain the details of the CMB. Some of these problems are solved with the relativistic generalization of Tensor-Vector-Scalar gravity (TeVeS) [10], but fails to explain galactic dynamics. Moreover, the matter distributions resulting from the bullet cluster are incompatible with any current theory of modified gravity.

Baryonic candidates to dark matter that emit a few or no radiation are categorized as Massive Astrophysical Compact Halo Objects (MACHOs) and include black holes, neutron stars, brown dwarfs, *etc.* Anyway, this possibility has been ruled out by a measurement of MACHOs in the Milky Way through gravitational lensing [11], moreover not enough baryons could have been produced in the early universe to account for dark matter.

If we exclude big massive galactic objects, a possible dark matter candidate is a neutral elementary particle. The only particle that account for dark matter requests in the Standard Model is neutrino, that however, due to its relativistic speed in the early universe (in fact is also called

hot dark matter), would not have induced such a large scale structure observed today [12].

Then, the remaining possibility is that dark matter is an undiscovered particle belonging to a theory beyond the Standard Model.

1.2.1 The WIMP miracle

The dark matter particle is assumed to be a Majorana particle, *i.e.* is equal to its own antiparticle. The DM, as other particles in the primordial universe, would have been in a thermal equilibrium through creation and annihilation processes. When the universe expanded and cooled, the temperature of particles fell down below their production energy (in case of WIMPs $T \sim \frac{1}{20} m_{WIMP}$), thus the particles were not created anymore. At a certain point, during expansion the annihilation rate of a particle is also suppressed and the relic abundance is fixed (*freeze-out*) to:

$$\Omega \approx \frac{G^{3/2} T_0^3}{H_0^2 \langle \sigma v \rangle} = \frac{3 \cdot 10^{-27} cm^3/s}{\langle \sigma v \rangle}, \tag{1.11}$$

where $\langle \sigma v \rangle$ is the average self-annihilation cross section multiplied by the particle velocity (in case of WIMP $\langle \sigma v \rangle \sim \alpha^2 / 8\pi m_{WIMP}^2$). In order to accomplish the correct abundance of dark matter Ω_{DM} in the universe, it should have a cross section in the electroweak scale and a mass in the range of GeV and TeV. Those are exactly the aspects required by a WIMP particle.

Some extensions of the Standard Model includes a new particle that could be dark matter, even though there are not experimental results confirming the existence of one of them. For instance, Supersymmetry (SUSY) [13] aims at unifying the electromagnetic, weak and strong fundamental forces at high energies. The Lightest Supersymmetric Particle (LSP) in several SUSY models is called *neutralino*, with a mass in GeV-TeV range. Then, this particle has the same mass and interaction scale as the one retrieved independently by thermal calculations from relic abundance of dark matter: for this reason it is called *WIMP miracle*.

1.3 Dark Matter searches

Three different methods are used for detecting dark matter: production at the accelerators, indirect and direct detection.

1.3.1 Production in colliders

The dark matter can be directly produced in laboratory, in high energy accelerators. The Large Hadron Collider (LHC), is the highest energy accelerator, that exploits proton-proton collisions and reached in 2015 13 TeV in the center-of-mass. The production of dark matter can be detected in different channels, such as (Figure 1.6):

- search for SUSY LSP, through decay products in events where there is an amount of energy missing, plus 4 jets and 4 leptons;
- search of general events with only one jet.

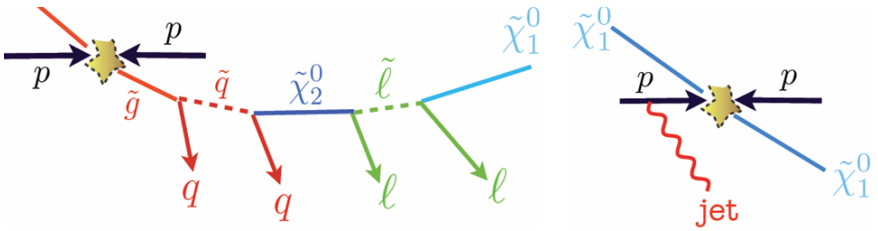

Figure 1.6: Production of WIMP in accelerators in two channels: 4jets + 4leptons + missing energy (left) and 1jet (right).

Up to date, there are no evidences of dark matter production at LHC [14].

1.3.2 Indirect detection

This technique aims at searching the particles product by the self-annihilation of WIMPs. For instance, if the dark matter would be a Majorana particle, it would annihilate producing two gamma rays or a gamma-ray and a Z-boson.

Most of the experiments based on the indirect detection technique search for dark matter accumulated around massive astrophysical objects, such the Sun or the Milky Way, where the high density should favor the annihilation. The gamma rays coming from dark matter annihilation have to be detected from the space, since their interaction length is 38 g/cm^2 (for energies between GeV and TeV), too low for reaching the Earth surface. In experiments such as *Fermi* [15], the telescope is sent in the space and detects the electromagnetic shower produced in the detector, when gamma rays coming from dark matter annihilation interact with the atmosphere. Moreover, the neutrinos and antineutrinos produced in the Sun from the dark matter annihilation can be revealed from telescopes installed in water or ice, such as *Ice Cube* [16]. Positrons and antiprotons coming from WIMP annihilation in the galactic center or in the halo are efficiently discriminated from background and detected by satellites in the space, such as *AMS* [17]. Up to date, there are no experiments of WIMP indirect detection strongly claiming the existence of dark matter.

1.3.3 Direct detection

The direct detection principle is of fundamental importance for this work, since it is the basis for the XENON experiment.

The direct detection technique consists in the identification of recoils in ordinary matter caused by the scattering of dark matter particles off a target material. In fact, the WIMPs have a speed lower than the escape velocity from Milky Way, then are trapped in the galactic halo. Given the low scattering cross section, WIMPs can cross several layer of materials (in galaxy and in Earth) and interact at most only once in the detector (*single scatter event*).

The differential rate of the elastic WIMP-nucleon interaction as function of the recoil energy E_R is [18]:

$$\frac{dR}{dE_R} = \frac{\rho_0 \sigma^p}{2\mu_p^2 m_\chi} A^2 F^2(q) \int_{v_{min}}^{v_{esc}} \frac{\rho(\vec{v} + \vec{v}_{Sun})}{v} d\vec{v}\,, \tag{1.12}$$

where ρ_0 is the local WIMP density, μ_p is the reduced WIMP-proton mass, m_χ is the WIMP mass, σ^p is the WIMP-proton cross section, A is the mass number of the target nucleus, F(q) is the nuclear form factor, $\rho(\vec{v})$ is the Maxwell-Boltzmann velocity distribution, $\vec{v}$ is the WIMP velocity respect to the laboratory, $\vec{v}_{Sun}$ is the Earth velocity respect to the galactic frame, v_{esc} is the escape velocity from the Milky Way and v_{min} is the minimum velocity of the WIMP hitting the target. Some parameters are known from astrophysics (ρ_0=0.3 GeV/cm^3, v_{Sun}=220 km/s, v_{esc}=544 km/s), other parameters are known from nuclear physics (m_p=938.272 MeV/c^2, A=131 in xenon, $F(q)$ described in Section 3.2), while the WIMP mass m_χ and cross section σ^p has to be determined from experiments.

The recoil energy of an elastic scattering is:

$$E_R = \frac{\mu_N^2 v^2 (1 - cos\theta')}{m_N}\,, \tag{1.13}$$

where μ_N is the reduced WIMP-nucleus mass, m_N is the mass of target nucleus and θ' is the angle between the recoiling nucleus and the WIMP direction after the scattering in the center of mass. In order to have a recoiling nucleus, the minimum velocity of the WIMP (θ'=180°) is:

$$v_{min} = \sqrt{\frac{m_N E_{Rmax}}{2\mu_N^2}}\,. \tag{1.14}$$

The Spin Independent (SI) WIMP-nucleus cross section at zero momentum transfer depends on the coupling of dark matter with protons f_p and neutrons f_n:

$$\sigma_{SI}^N = \frac{4\mu_N^2}{\pi}[Z f_p + (A - Z) f_n]^2\,. \tag{1.15}$$

If we assume the two constant are similar, the cross section become:

$$\sigma_{SI}^p = \frac{4\mu_p^2}{\pi} f_p^2\,. \tag{1.16}$$

Thus, the differential cross section, dependent by the recoil energy, is:

$$\frac{d\sigma_{SI}(E_R)}{dE_R} = \frac{m_N}{2\mu_N^2 v^2}\sigma_{SI}^N F^2(q^2)\,. \tag{1.17}$$

The WIMP velocity distribution follows an isotropic Maxwell-Boltzmann distribution, that describes a gas of particles in thermal equilibrium and in the semi-classical limit:

$$\rho(v_a) = \left(\frac{m_\chi}{2\pi KT}\right)^{\frac{1}{2}} e^{-\frac{m_\chi v_a^2}{2KT}} = \frac{1}{\sqrt{2\pi}\sigma} e^{-\frac{v_a^2}{2\sigma^2}}\,, \tag{1.18}$$

where K is the Boltzmann constant, T is the absolute temperature and v_a is the velocity component ($a = x, y, z$). The distribution is clearly a Gaussian in each coordinate, with mean value $\langle v_a \rangle$=0 and standard deviation σ=$\sqrt{KT/m_\chi}$. By maximizing the distribution one get the most likely value of the WIMP velocity, equal to v_0=$\sqrt{2KT/m}$=$\sqrt{2}\sigma$. From astrophysics one get the most probable velocity, equal to v_0=220 km/s, and the velocity distribution results:

$$\rho(\overrightarrow{v}) = \frac{1}{\pi^{3/2} v_0^3} e^{-\frac{\overrightarrow{v}^2}{v_0^2}}\,. \tag{1.19}$$

In SI interactions, the WIMP-nucleon cross section scales with A^2. For this reason high mass target materials are favored, even though they have to combine with the effect of the nuclear form factor, that depends on the size of the nucleus. Figure 1.7 shows the differential rate of a

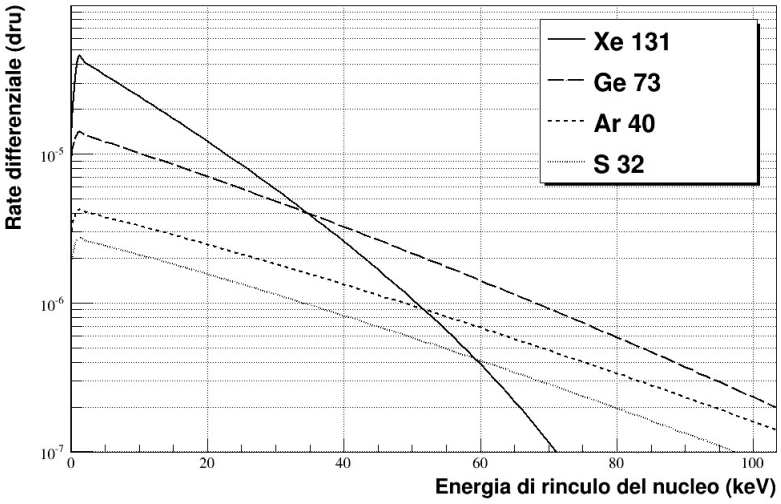

Figure 1.7: Differential event rate of WIMP-nucleus elastic scattering for different target materials: xenon (Xe), germanium (Ge), argon (Ar) and sulfur (S).

WIMP-nucleus interaction as function of the recoiling energy in unit

of dru (events/day·kg·keV), for different target materials, assuming a WIMP-nucleon cross section σ^p=10^{-45}cm^2 and a WIMP mass m_χ=100 GeV [19]. Xenon is the best target material at very low energies, sensitive for the WIMP search. As an example, by integrating the differential rate of a WIMP interaction with a xenon nucleus, in a typical recoiling electron equivalent energy range of [10,50] keVee, we would have only 3 events per year, if the WIMP mass is 100 GeV/c^2 and the cross section is 2×10^{-45}cm^2; it is clearly a rare event process and the detection is challenging.

In case of Spin Dependent (SD) interactions, the WIMP can be considered as a spin-1/2 and spin-1 field, coupling through quark axial current with protons or neutrons separately and the WIMP-nucleon cross section, Equation 1.17, would change accordingly (see Section 3.1.4). For this kind of detection, a nucleus with odd number of nucleons is required, and xenon is again a good choice as it has two isotopes with non-zero nuclear spin.

Chapter 2

Liquid xenon as a detection medium

Noble liquids are used in astroparticle physics experiments as a radiation detection medium, since they are pure, chemically inert and excellent insulators. In particular, the advantage of using Liquid Xenon (LXe) is the production of both ionization electrons and scintillation photons in response to an incoming particle, from which is possible to recognize its nature and energy. This property, together with the high atomic mass and scintillation/ionization yield, makes LXe the best target for dark matter direct detection experiments.

In this Chapter we report the main properties of xenon, focusing on its usage as a detection media.

2.1 Physical properties of LXe

The high atomic number and the high density of noble liquids make them very efficient media to stop penetrating radiation and to reduce the external background. In Table 2.1 are shown some xenon properties, compared with other noble elements [20, 21].

Among the noble gases, xenon is the heaviest element ($A \sim$131) before the radioactive Rn; this is fundamental for spin-independent interactions, whose cross section scales with A^2 (Section 1.3.3). Moreover, the large atomic number (Z2=54) and high density ($\rho \sim$2.86 g/cm^3) of LXe allows for a good *self-shielding*, meaning that the outer regions of the xenon volume absorb much of the external γ radiation, leaving the inner volume with an highly reduced background.

Xenon is present in the Earth's atmosphere with a very low concentration (below 0.1 ppm); it is obtained as a byproduct of the liquefaction of air and its separation into oxygen and nitrogen. ^{85}Kr, a radioactive element, is the main intrinsic contaminator, therefore in order to perform rare events experiments it has to be removed by a dedicated distillation system.

Natural xenon contains nine stable isotopes, two of them (^{129}Xe and

Property	He	Ne	Ar	Kr	Xe
Atomic number Z	2	10	18	36	54
Mean atomic weight A	4.00	20.18	39.95	83.80	131.29
Radius [pm]	31	38	71	88	108
Melting point T_m at 1 atm [K]	0.95	24.6	83.8	115.8	161.4
Boiling point T_b at 1 atm [K]	4.22	27.1	87.3	119.9	165.0
Gas density ρ_{gas} at 298 K [g/l]	0.16	0.82	1.63	3.43	5.40
Gas density ρ_{gas} at T_b [g/l]	16.6	9.56	5.77	8.89	9.99
Liq density ρ_{liquid} at T_b [g/cm^3]	0.12	1.21	1.40	2.41	2.94
Critical temperature T_c [K]	5.19	44.4	150.8	209.4	289.7
Critical pressure P_c [atm]	2.24	27.2	48.1	54.3	57.6
Critical density [g/cm^3]	0.0696	0.482	0.544	0.91	1.10
Triple point temperature T_t [K]	–	24.56	83.81	115.78	161.41
Triple point pressure P_t [atm]	–	0.424	0.68	0.722	0.805
Dielectric constant of liquid ϵ_l	1.0491	1.188	1.51	1.66	1.95

Table 2.1: Physical properties of noble elements.

^{131}Xe) with odd spin component, that allow to directly detect spin-dependent interactions of dark matter particles. Moreover, xenon is the second element with most stable isotopes and has no long-lived radioisotopes, besides ^{136}Xe, which undergoes double beta decay (half life of 2.17×10^{21} y) [22]. The second longest-lived radioisotope is ^{127}Xe with a half-life of 36.3 d. The absence of intrinsic radioactivity from xenon isotopes is one of the properties that makes this noble gas the best choice as a detection medium for rare events experiments.

Figure 2.1 shows a phase diagram of crystalline, liquid, and gaseous xenon [23]. Also the relatively easy xenon handling system makes xenon a very attractive material. In fact, at atmospheric pressure its boiling point is relatively high, ranging between 165 K (-108°C) to 187 K (-86°C). It allows to use a basic system made of copper cold finger with liquid nitrogen cooling bath, but for a more stable operation one can use a more sophisticated cryogenic Pulse Tube Refrigerator (PTR), that is efficient, practical and works with hundreds of kg of xenon.

Another advantage of using liquid xenon is the capability to transform the energy released by an impinging particle into measurable signals. In fact, it responds with both ionization electrons and scintillation photons to ionizing radiation and is a very efficient scintillator (yield of $\sim45\times10^3$ photons/MeV for relativistic electrons). Moreover, it is transparent to its own scintillation light and the high mobility of ionization electrons in the medium allows the drift and measurement of all the charge signal when applying an external electric field.

The technology that uses noble liquids has the big advantage of *scalability*. In fact, since the expected WIMP interaction rate increases linearly with the target mass, scaling up a detector reduces the run time required to achieve a certain sensitivity.

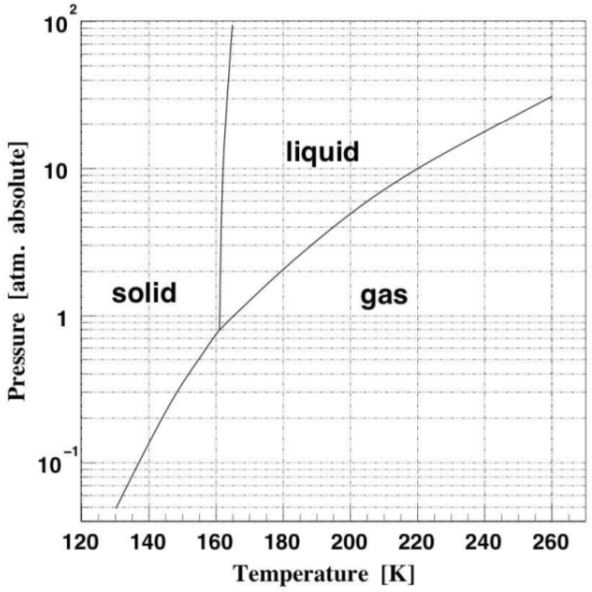

Figure 2.1: Phase diagram of xenon.

In Tab. 2.2 other physical properties of liquid xenon are summarized [24].

Property	Value
Abundance in atmosphere [ppm]	0.09
Compressing factor ρ_{liquid}/ρ_{gas}	544
Isotopes	^{124}Xe(0.09%), ^{126}Xe(0.09%), ^{128}Xe(1.92%), ^{129}Xe(26.44%), ^{130}Xe(4.08%), ^{131}Xe(21.18%), ^{132}Xe(26.89%), ^{134}Xe(10.44%), ^{136}Xe(8.87%)
W_{gas} [eV]	22
W_{liquid} [eV]	15.6
Ionization potential I [eV]	12.13
Energy gap E_{gap} [eV]	9.28

Table 2.2: Physical properties of liquid xenon.

2.2 Particle interaction of LXe

2.2.1 Main xenon parameters

Noble elements in solid phase are excellent insulators, with an electronic band structure, similar to the semiconductors. From the absorption spectroscopy it is possible to measure the energy gap E_{gap} between the valence and the conduction band. Direct measurements of E_{gap} in

xenon, argon and krypton proved that also the liquids have a band structure; atoms are joined by bonds, forming dimers and the large energy gap makes also noble liquids excellent insulators.

In LXe the energy deposited by impinging particles is converted into ionization, excitations and free electrons with a kinetic energy lower than the first excited state (*subexcitation electrons*). The excited atoms subsequently decay and emit scintillation photons. Some of the electrons from ionization will recombine leading to the scintillation, and the remaining ones can be collected by using an external electric field. The motion of free electrons is function of the applied electric field E; the *electron drift velocity* is defined as:

$$v_d = \mu E \,, \tag{2.1}$$

where μ is the *electron mobility*, equal to 2000 $\mathrm{cm}^2/(\mathrm{V}\cdot\mathrm{s})$ (similar to silicon). At high fields v_d saturates.

Actually, even without applying any electric field, some electrons might escape recombination and termalize far away from their parent ions. The recombination process is strongly dependent on the external electric field and the nature of impinging particle, as will be shown in the next Sections.

If we call N_i the electron-ion pairs and N_{ex} the excited atoms, the transfer of the deposited energy E_0 to the medium is dominated by the following equation, originally proposed by Platzman [25]:

$$E_0 = N_i E_i + N_{ex} E_x + N_i \epsilon \,, \tag{2.2}$$

where E_i is the average expenditure of energy to product an electron-ion pair, E_x is the average energy to excite an atom and ϵ is the average kinetic energy of subexcitation electrons. The W-value is defined as the average energy required to produce an electron-ion pair, that can be written as:

$$W = \frac{E_0}{N_i} = E_i + E_x \frac{N_{ex}}{N_i} + \epsilon \,. \tag{2.3}$$

The electronic band structure of noble liquids allows us to rewrite the equation in terms of E_{gap} (instead of the ionization potential of gas I):

$$\frac{W}{E_{gap}} = \frac{E_i}{E_{gap}} + \frac{E_x}{E_{gap}} \frac{N_{ex}}{N_i} + \frac{\epsilon}{E_{gap}} \,. \tag{2.4}$$

For xenon, argon and krypton, the calculated ratio is $W/E_{gap} \simeq 1.65$, in agreement with the measured value; this supports the electronic band structure assumption for noble liquids. The conversion efficiency from the absorbed energy E_0 to a measurable signal is related to the W-value and the average energy required to produce a scintillation photon, W_{ph}. We can obtain the relation between the average energy required to produce an electron-ion pair W and a scintillation photon W_{ph} as follows:

$$W_{ph} = \frac{E_0}{N_{ex} + N_i} = \frac{W}{N_{ex}/N_i + 1}. \tag{2.5}$$

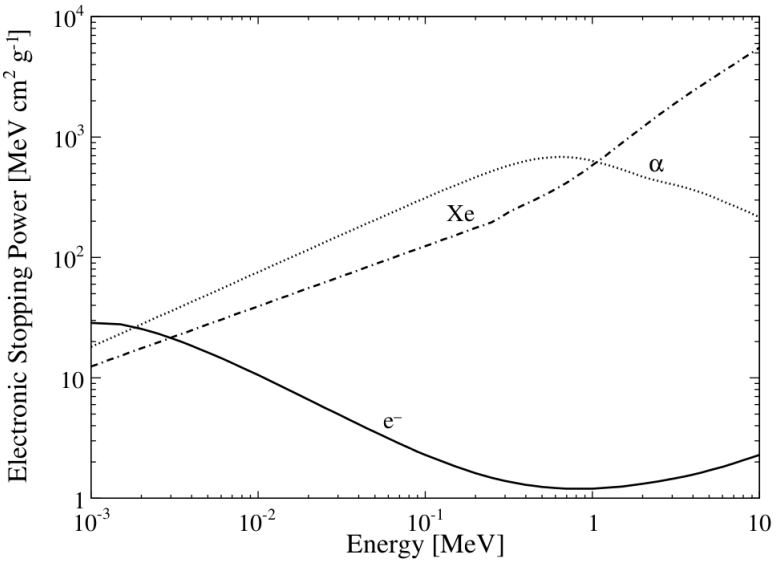

Figure 2.2: Electronic stopping power for electrons, α particles and nuclear recoils in xenon.

The lowest W-value that characterize liquid xenon (W_{liquid}=15.6 eV) among the other noble liquids make it the better medium for the detection of ionizing radiation. The ratio of excitons to electron-ion pairs in LXe is about N_{ex}/N_i ∼0.06, estimated by using the oscillator strength spectrum of solid xenon obtained from photo-absorption spectra [26]. A more recent result indicates a higher value of N_{ex}/N_i ∼0.20 [27] and allows to retrieve the maximum energy required to produce a scintillation photon, equal to W_{ph}(max)=13.8±0.9 eV.

2.2.2 Electronic stopping power

The type of interaction and the amount of energy lost in a xenon detector depends on the energy and nature of the incident radiation [28]. In the energy range of interest for dark matter direct search, between 1 and 100 keV, charged particles, such as α and electrons, lose their energy by interacting with orbital electrons and nuclei of the xenon atom, mediated by electromagnetic forces. In Figure 2.2 is shown the *electronic stopping power* of xenon for electrons, α particles and nuclear recoils [29, 30, 31], defined as the amount of energy lost in interactions with atomic electrons, by an incoming particle, per unit of path length.

The inelastic collision with atomic electrons produce excitation and ionization both called *electronic excitation*. Electrons show a higher stopping power at lower energies, meaning that they have a higher density of electronic excitations; for nuclear recoils the behavior is the opposite. In the WIMP-search region, electron recoils have tracks shorter than ∼100μm and can thus be considered essentially point like. It means that external background from α and β emitters is shielded by the outer part

of liquid target, and will not reach the inner one (*fiducial volume*).

For nuclear recoils one can define the *nuclear stopping power*, as the probability for an elastic collision with target nuclei to occur. It requires that the energy lost is also due to atomic motion, *i.e.* heat. Since heat does not give any measurable signal in dark matter direct detectors based on liquid xenon, the *nuclear quenching* is one of the most important quantities to measure.

α particles

As already mentioned, since α particles are positively charged, they will interact with orbital electrons of the xenon atom, through the Coulomb force. Thus, the orbital electron can either jump to higher level shell (excitation), or can be completely ejected from the atom (ionization); an α particle crossing the detector material will interact many times producing excitation and ionization. The typical track of an α particle is a straight line.

electrons

In case of e^- the interaction principle with the detector material does not differ from the one with α particle, but the mass of the impinging particle is the same as the orbital electrons of the xenon atom. This makes the path of relativistic electrons quite tortuous.

2.2.3 γ-ray interactions

γ rays can mainly interact in three different ways: *photoelectric absorption*, *Compton scattering* and *pair production*.

The photoelectronic absorption happens when a γ ray is completely absorbed by an atom and as a consequence an electron is ejected from one of the bound shells. The cross section of this process is maximum for low energy γ rays, such as 122 keV from ^{57}Co. The Compton scattering occurs when the γ ray changes its trajectory while transferring part of its energy to an orbital electron of a xenon atom. The energy range of this interaction is around 1 MeV; the 662 keV γ ray from ^{137}Cs is an example of this kind of interaction. The pair production is the creation of an electron-positron pair due to an incident γ ray. This process requires a minimum energy that is twice the rest-mass of an electron (1.02 MeV), but is dominant for γ rays of several MeV in energy.

In the three processes, the produced energetic electrons (and positrons in the case of pair production) will lose energy through electronic excitation. In Figure 2.3 is shown the attenuation coefficient and length in liquid xenon as function of the particle energy, for γ interactions (using ρ_{LXe}=2.86 g/cm^3) [32]. We can recognize the L-shell (around 5 keV) and K-shell (around 30 keV) of xenon from the photoelectric absorption

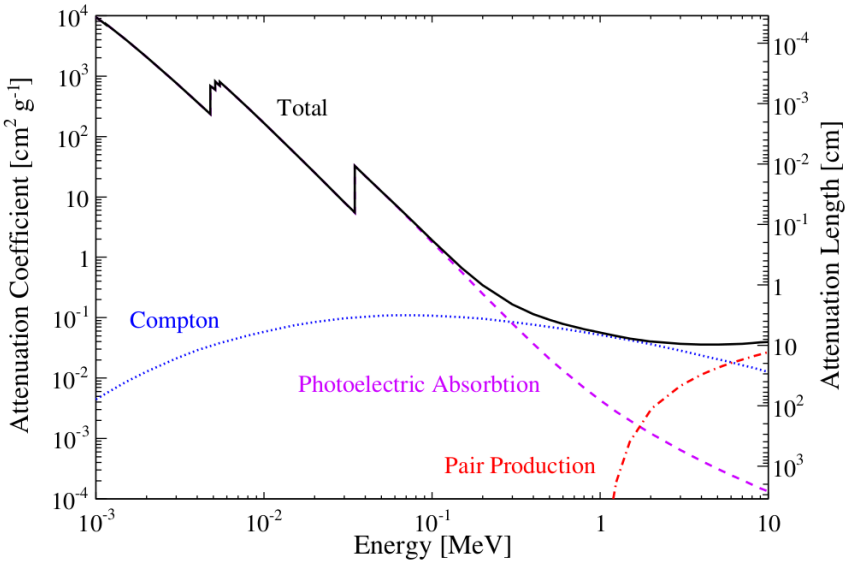

Figure 2.3: Total (solid black), photoelectric absorption (dashed violet), Compton scattering (dotted blue), and pair production (dash-dotted red) γ ray attenuation coefficients and lengths in LXe, as a function of energy.

shape. Moreover, the attenuation length of 1 MeV γ ray is about 6 cm, meaning that γ rays are absorbed in the outer layer of the detector.

The main external background producing electronic recoils in the energy region of interest for dark matter searches is due to low-energy single Compton scatters.

2.2.4 Neutron interactions

Neutrons interact with the nucleus of xenon and the type of interaction depends on their energy. In fact, fast neutrons transfer their energy via *elastic scattering* to a nucleus of the target material. In case of enough energy, the neutron can also interact via *inelastic scattering*, spending part of its energy to excite the nuclei of the target; the decay by emission of a γ ray happens in a very short time, below 1 ns. On the other hand, *slow neutrons* interact mainly via elastic scattering and *radioactive capture* (n,γ). Most of those neutrons are *thermal neutrons*, with an average energy of 0.025 eV at room temperature. Figure 2.4 reports the neutron total elastic scattering, total inelastic scattering and radiative capture cross sections on xenon as a function of energy [33].

The inelastic scattering do not constitute a dangerous background, since the γ ray emitted during the nuclear de-excitation has an energy above the WIMP search region. Long-lived meta-stable states induced by inelastic processes (*i.e.* ^{125m}Xe with half-life of 57 s, ^{131m}Xe with half-life of 11.8 d) can be used to uniformly calibrate the inner part of the detector, where the external γ source can not penetrate. However, neutron

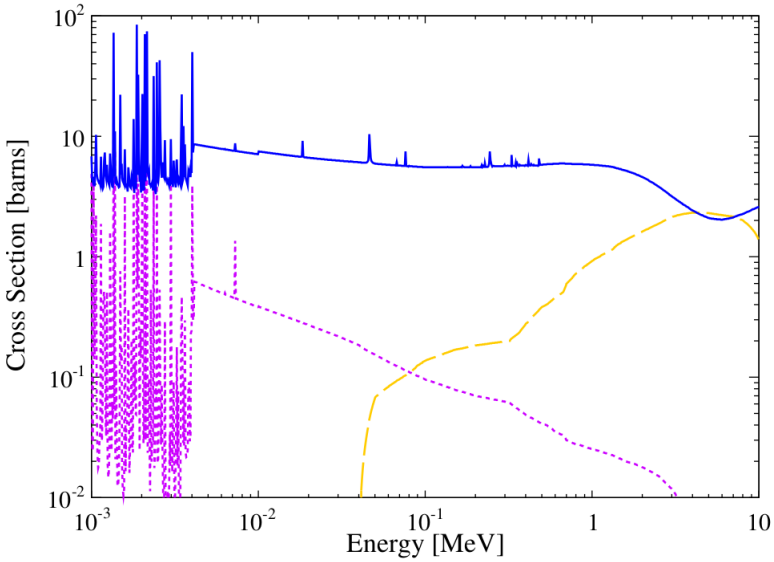

Figure 2.4: Neutron total elastic scattering (solid blue), total inelastic scattering (long dashed orange), and radiative capture (dashed violet) cross sections on xenon.

elastic scatters mimic the expected dark matter signal, representing an irreducible background. Neutrons with 100 keV energy which elastically scatter with xenon nuclei have a mean free path of around 13 cm (and 20 cm for 10 MeV energy neutrons); it means that fast neutrons are very likely to scatter multiple times in large scale detector, allowing to reject this kind of background.

2.3 Particle detection

The aim of a LXe direct detectors is to convert in the most efficient way the energy released by an impinging particle that collides with atomic electrons or nuclei of the target material, into a measurable signal. In Table 2.3 are summarized some properties of liquid xenon related to its response to an external radiation [27, 34, 35, 36, 37, 38].

2.3.1 Scintillation signal

The scintillation consists in the emission of photons from an atom. In xenon, it is originated on the decay of the dimer Xe_2^* to the ground state. Both the products of electron-ion recombination (Xe^+) and direct excitation (Xe^*) result in the creation of excited dimers. In fact, as a first step, a ionized atom Xe^+ interacts with Xe atom in the ground state and

Property	Value
Ionization [e^-/keV]	64
Scintillation [γ/keV]	46
Scintillation wavelength λ [nm]	177.6
Excimer singlet lifetime τ_s [ns]	2.2
Excimer triplet lifetime τ_t [ns]	27
Rayleigh scattering length (178 nm) λ_0 [cm]	29
Refractive index (178 nm)	1.69
Exciton-to-ion ratio N_{ex}/N_i	0.06
W_{ph} (max) [eV]	13.8
W_{ph} (α) [eV]	17.9
W_{ph} (β) [eV]	21.6
Fano factor F	0.059

Table 2.3: Properties of the signal coming from LXe.

generates one exciton Xe^* in the following chain [39]:

$$\begin{aligned} Xe^+ + Xe &\rightarrow Xe_2^+ \\ Xe_2^+ + e^- &\rightarrow Xe^{**} + Xe \\ Xe^{**} &\rightarrow Xe^* + heat\,. \end{aligned} \tag{2.6}$$

Then, the exciton coming from either ionization or direct excitation, collides with neighboring atom and the photons are emitted according to the interaction:

$$\begin{aligned} Xe^* + Xe &\rightarrow Xe_2^* \\ Xe_2^* &\rightarrow 2Xe + \gamma\,. \end{aligned} \tag{2.7}$$

However, when the target material is in gas phase, the scintillation comes mostly from direct excitation because the collision process that results in the recombination occurs with a low probability.

Figure 2.5 shows the scintillation light curve as a response to electrons, α particles and fission fragments, in the absence of electric field (top) [40]. The bottom plot is the electronic recoil scintillation curve at zero and 4 kV/cm electric field [39]. It is possible to distinguish two different components depending by two nearly degenerate "molecular" (Xe_2^+) states of spin: the shorter decay shape is produced by the de-excitation of singlet states, while the longer one is produced by the de-excitation of triplet states. In particular, the triplets and singlets decay time is respectively 2.2 ns and 27 ns for relativistic electrons that interact with liquid xenon; this medium is the fastest above all noble liquid scintillators. Another noble liquid which shows the same behavior is argon. When liquid argon is excited by different particles, the scintillation decay time is easily distinguishable between singlet and triplet states (for instance, the singlets and triplets decay time is 6 ns and 1.5 μs for relativistic electrons interacting with LAr). This feature makes argon an effective medium for the

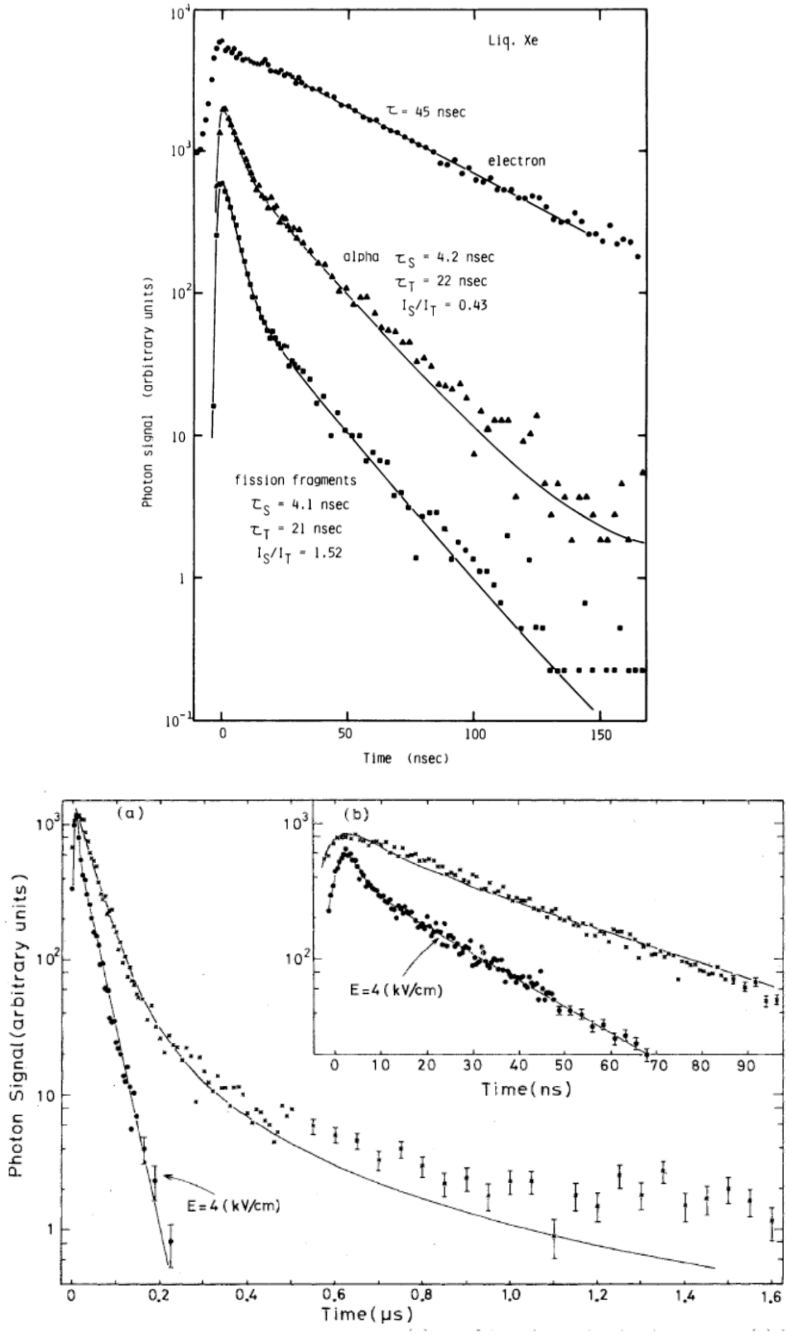

Figure 2.5: Top: decay curves of scintillation from liquid xenon excited by electrons, α particles and fission fragments, without an applied electric field. Bottom: same decay curves, but for electron recoils at zero and 4 kV/cm electric field (long and short time scale).

Pulse Shape Discrimination (PSD), see Section 3.1.3. In particular, the singlet states are favored in nuclear recoils, while they are reduced in the case of electron recoils.

Due to the different configuration of the energy levels of dimers and atoms in noble liquids, the scintillation photons produced will not be re-

absorbed by the atoms, making the target material totally transparent. Moreover, the scintillation light is emitted in all the three phases of the noble liquid in the UV region. The emission spectrum of LXe is quite broad, with $\Delta\lambda$=14 nm and a peak at 178 nm, that corresponds to a 7 eV energy photon. Dedicated photomultipliers (PMTs) with high quantum efficiency, that are able to operate in low temperature condition, have been developed in order to detect the xenon wavelength. This is a big advantage related to xenon detectors among the other noble liquids, since for instance the wavelength of LAr (128 nm) requires a wavelength shifter in order to be detected, resulting in a worsen resolution.

Scintillation yield

The *scintillation yield* is the number of photons produced per unit of recoil energy (γ/keV$_r$). The scintillation yield of liquid xenon and argon is similar to the one of NaI, allowing to operate in low threshold condition, sensitive to the dark matter energy region.

The scintillation yield depends on the type of particle and on the energy released in the medium. Since a precise measurement of the absolute (nuclear and electron recoils) light yield is difficult, because nuclear recoils are affected by a quenching effect (see Section 2.3.3), the most used quantity is the so called *relative scintillation efficiency* $\mathcal{L}_{eff}$ for nuclear recoils. It consists in the scintillation signal released by scattering with a target nucleus, function of the recoil energy E_{nr}, and is defined as the ratio between the scintillation yield of nuclear recoils $L_{y,nr}$ to that of electron recoils $L_{y,er}$ in absence of electric field:

$$\mathcal{L}_{eff}(E_{nr}) = \frac{L_{y,nr}}{L_{y,er}} = \frac{E_{er}}{n_{\gamma,er}} \frac{n_{\gamma,nr}}{E_{nr}} = \frac{1}{L_{y,er}} \frac{n_{pe,nr}}{E_{nr}} = \frac{E_{ee}}{E_{nr}}\,, \tag{2.8}$$

where $n_{\gamma,nr}$ and $n_{\gamma,er}$ are the number of primary photons from nuclear and electronic recoil respectively and $E_{ee} = n_{pe,nr}/L_{y,er}$ is the *electron-equivalent* energy. $L_{y,er}$ is typically obtained from the electron recoil of the photoabsorbed 122 keV γ rays from ^{57}Co source as reference. $\mathcal{L}_{eff}$ is fundamental for the determination of the sensitivity of direct dark matter detectors. Two methods are used to measure $\mathcal{L}_{eff}$ for nuclear recoils: an indirect method, by comparing the measured energy spectra from neutron source with Monte Carlo (MC) predictions, and a direct method, by using monoenergetic neutron fixed-angle scatters. Figure 2.6 shows the scintillation efficiency as function of the recoil energy, obtained by fitting the MC simulation of the expected nuclear recoil energy spectrum in liquid xenon to ^{241}AmBe data [41]. In the same plot, direct measurements of $\mathcal{L}_{eff}$ down to 3 keV$_r$ and a global fit to them have been reported as reference. In fact, using a collimated beam of neutrons with known energy E_n, it is possible to retrieve the $\mathcal{L}_{eff}$ through elastic scattering on Xe atoms [42]:

$$E_{nr} \approx 2E_n \frac{m_n\, M_{Xe}}{m_n + M_{Xe}} (1 - cos\theta)\,, \tag{2.9}$$

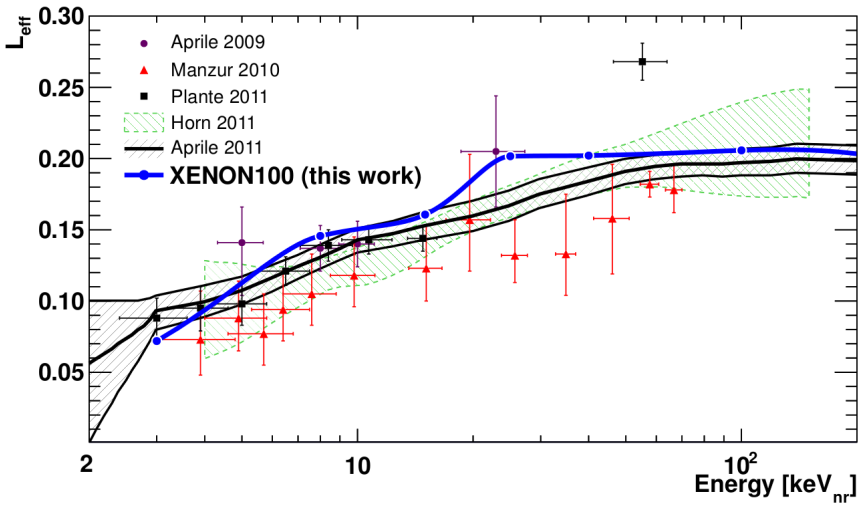

Figure 2.6: Energy dependent scintillation efficiency $\mathcal{L}_{eff}$ for nuclear recoils obtained from fitting the MC spectrum to the liquid xenon response to an ^{241}AmBe source (blue line), together with direct measurements down to 3 keV$_r$ (data points) and global fit to them (black line) [41].

where m_n and M_{Xe} are the masses of the neutron and Xe nucleus respectively and θ is the scattering angle. The elastic scatters of monoenergetic neutrons E_{nr} can be tagged by organic liquid scintillator detectors located at fixed angles θ, and one can retrieve the corresponding $\mathcal{L}_{eff}$. The spread in measured recoil energies in direct measurements mostly comes from the energy spread of the neutron source and the angular acceptance of the LXe and neutron detectors due to their finite sizes.

Light absorption

Even though noble liquids are transparent to their scintillation light, minuscule amount of impurities may absorb a large fraction of light, reducing the light yield. The light attenuation as function of the path x can be described as:

$$I(x) = I(0)e^{-x/\lambda_{att}}\,, \tag{2.10}$$

where λ_{att} is the *photon attenuation length*. λ_{att} depends by the absorption length λ_{abs} and the elastic scattering length of photons λ_{sca} (*Rayleigh scattering*), as follows: $\frac{1}{\lambda_{att}} = \frac{1}{\lambda_{abs}} + \frac{1}{\lambda_{sca}}$.

The most serious impurity is the water vapor, that has to be minimized. For future ton-scale or multi ton-scale noble liquid detectors a photon attenuation length longer than 10 m is required, corresponding to less than 10 ppt (part per trillion) of water vapor contamination. Moreover, the good property of liquid xenon to have a relatively high liquefaction temperature allows a more simple operation handling of the system, but does not freeze impurities.

2.3.2 Ionization signal

The ionization consists in the production of electron-ion pairs as response of an impinging particle. Since the W-value in noble liquids is smaller than in the gas phase, the liquids are excellent for the ionization. The smallest W-value that characterize LXe among the other noble liquids, guarantees the largest ionization yield, making xenon the best choice as detector media for ionization radiation.

The electron-ion pair production is strongly dependent, as in the scintillation case, on the way in which the ionizing particles dissipate their energy into the medium. In fact, the behavior of heavy particles (velocity down to $\beta \approx 0.1$) is explained by the Bethe-Bloch formula [43], that says the energy is released to the medium through inelastic scattering on atomic electrons and induces ionization. In the velocity range $0.01 \lesssim \beta \lesssim 0.1$ some assumptions of the Bethe-Bloch equation are not valid anymore and different interactions, such as electron capture, start to dominate. At lower velocities ($\beta < 0.01$) the energy is transferred totally to atoms via inelastic scattering and the ionization has low efficiency; a good explanation of the energy transfer in this energy regime has been provided by Lindhard [44].

Ionization yield

The *ionization yield* is the number of electron-ion pairs produced per unit of recoil energy (e^-/keV_r). In case an external electric field is applied, the ionization signal is visible through the photons emitted from both recombination between electron-ion pairs and interaction of ion with target atoms, as described in the Equation 2.6.

An aspect that decreases the efficiency of detecting ionization is given by the production of subexcitation electrons, whose energy is converted into heat and can not be measured. On the other hand, one can detect the produced electrons by applying an external electric field that drift them toward the electrode, where they can be collected and measured. This technique is used in Time Projection Chamber (TPC) detectors, as will be widely described in the next Chapter.

Fano limit to energy resolution

When a ionizing particle loses all its energy in a target material, the standard deviation δ of the production of electron-ion pairs (N_i) does not follow a Poisson statistics, as demonstrated by Fano [45]. In fact, the ionization process is not statistically independent, since the number of ways an atom may be ionized is limited by the discrete electron shells, resulting in a better energy resolution:

$$\delta^2 = \langle (N - N_i)^2 \rangle = F \times N_i, \tag{2.11}$$

where F is a constant smaller than 1 that depends on the target material, also called *Fano factor*. When F=1 the process becomes Poissonian. The Fano factor in LXe is equal to 0.059 [38].

Using the ionization channel only, the energy resolution in liquid xenon, expressed as full width at half maximum, is:

$$\Delta E(\text{keV}) = 2.35\sqrt{F\,W(\text{eV})\,E(\text{MeV})}, \tag{2.12}$$

where E is the energy of the impinging particle.

The Fano-limit to the energy resolution in liquid xenon has not yet been achieved, but by using the summed signals of ionization and scintillation measured simultaneously one can strongly improve the sensitivity (Section 2.3.4).

Electron attachment

In order to perform an efficient measurement of the ionization signal using a TPC, the presence of electronegative impurities in the medium has to be minimized. In fact, during its path, an electron could be trapped by an impurity AB through one of the following processes:

- radiactive attachment

$$e^- + AB \rightarrow AB^- + h\nu \tag{2.13}$$

- dissociative attachment

$$e^- + AB \rightarrow A + B^- \tag{2.14}$$

- three-body attachment

$$\begin{aligned} e^- + AB &\rightarrow (AB^-)^* \\ (AB^-)^* + Xe &\rightarrow AB^- + Xe \end{aligned} \tag{2.15}$$

As a consequence, a negative ion would be created, decreasing the electron concentration $[e]$ and the capability of measuring all the electrons produced by ionization. The electron concentration depends on the time t as follows:

$$[e(t)] = [e(0)]e^{-(\sum_i K_{S_i}[X]_i)t} = [e(0)]e^{-t/\tau}\,, \tag{2.16}$$

where K_{S_i} is the attachment rate constant and $[X]_i$ is the concentration of the impurity i. The following quantity:

$$\tau = (\sum_i K_{S_i}[X]_i)^{-1} \tag{2.17}$$

is the so called *electron lifetime* and represents the mean free time after which an electrons is catched by an impurity. The decreasing in the electron concentration is also expressed by the *electron attenuation length*:

$\lambda_{att} = \mu E \tau = v_d \tau$, where μ is the electron mobility, E is the external electric field and v_d is the drift velocity of electrons in the medium (Equation 2.1). This equivalence is true only for low electric field, while for higher values the drift velocity saturates. In case of TPC detectors, the fact that an electron can be catched by electro-negative impurities during the path toward the anode, introduces a position dependence of the signal, that has to be corrected by the electron lifetime if one wants to reconstruct the z-point where the interaction is occurred (Section 3.1). The small cloud of electrons created by the ionizing particle remains localized during its drift along the electric drift line, however electrons tend to diffuse from the high-density part; this process affects the *(x-y)* position resolution in liquid xenon detectors. The diffusion is characterized by the longitudinal component (D_L) and the transverse component (D_T) with respect to the electric field direction, and their relation is typically $D_L \sim 1/10\ D_T$. The standard deviation of the electron cloud in the transverse component is [28]:

$$\sigma_{D_T} = \sqrt{D_T\, t}\,, \tag{2.18}$$

where $t = d/v_d$ is the drift time of the electron after a path d.

The attachment of electrons to impurities is considered one of the most dangerous factors for the performance of large scale detectors that measure the ionization signals. For instance, in order to achieve an attenuation length longer than 1 m, the concentration of impurities has to be maintained lower than 1 ppb level O_2 equivalent. Also outgassing from the detector materials contribute to the total concentration of impurities, through a diffusion process. The main electronegative impurities in liquid xenon are oxygen, water and carbon dioxide. Figure 2.7 shows the electric field dependence of the rate constants of electron attachment K_S to SF_6, N_2O and O_2 in liquid xenon [46]. Several methods have been developed in order to remove impurities, such as, absorption and chemical reactions, filtration, separation, electrical discharges and irradiation with gamma-rays.

2.3.3 Quenching effect for nuclear recoils

Compared to the scintillation yield of recoiling electrons, with almost all their energy transferred to measurable electronic excitation, the scintillation yield of nuclear recoil excitation is significantly reduced by the *nuclear quenching*. An explanation to this phenomenon can be searched in the higher ionization density track due to nuclear recoil than the electron recoil.

Heavy α particles and nuclear recoils create a cylindrical track in which most of the energy is lost in an inner dense region, or *core*, where a high recombination rate occurs. The core is surrounded by a low density *penumbra* of delta rays. Due to a high recombination quenching in the core region, a complete charge collection is difficult. In fact, less than 20% of the total charge is typically collected. On the other hand,

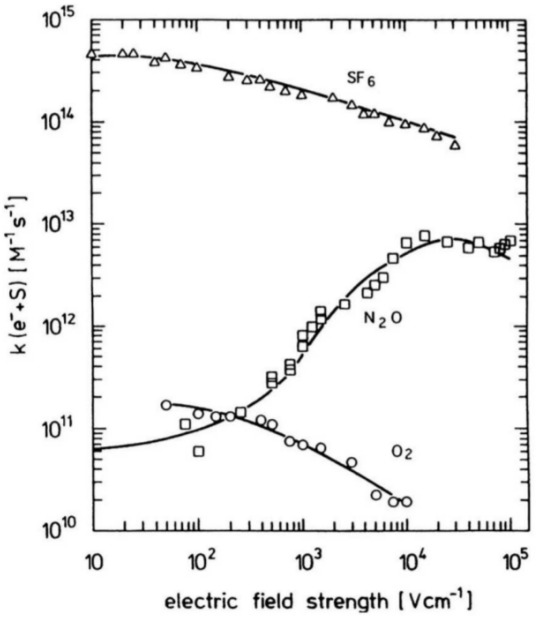

Figure 2.7: Electric field dependence of the rate constants of electron attachment to different solutes in LXe [46].

electrons create a less dense track, thus the quenching is much lower. Almost complete charge collection at modest electric field is possible for Minimum Ionizing Particles (MIP).

At the atomic level, the quenching could be generated before the collision between an exciton and a neighboring atom. In fact, according to the *bi-excitonic quenching* mechanism [47], two excitons could produce a free electron, resulting in one final scintillation photon only, instead of two (Figure 2.8). Since the excitons need to collide with each other in order to give rise to this mechanism, it occurs only in a very dense tracks, as the ones produced by nuclear recoils. Another contribution to the quenching is given by low values of Linear Energy Transfer (LET), such as relativistic electrons and γ rays that induce electronic recoils, for which after the ionization some electrons (*escape electrons*) do not recombine in a timescale useful for the detection.

Lindhard factor

A parameterization of the expected fraction of nuclear recoil energy E_r that is transfered to electrons, is given by the Lindard factor [44]:

$$\mathcal{L} = \frac{kg(\epsilon)}{1 + kg(\epsilon)}\,, \tag{2.19}$$

where $k = 0.133Z^{2/3}A^{1/2}$ is the proportionality constant between the electronic stopping power and the velocity of the recoiling xenon atom, $g(\epsilon) = 3\epsilon^{0.15} + 0.7\epsilon^{0.6} + \epsilon$ and $\epsilon = 11.5E_r(keV)Z^{-7/3}$. The Lindhard parameterization provides an accurate prediction of the nuclear quenching

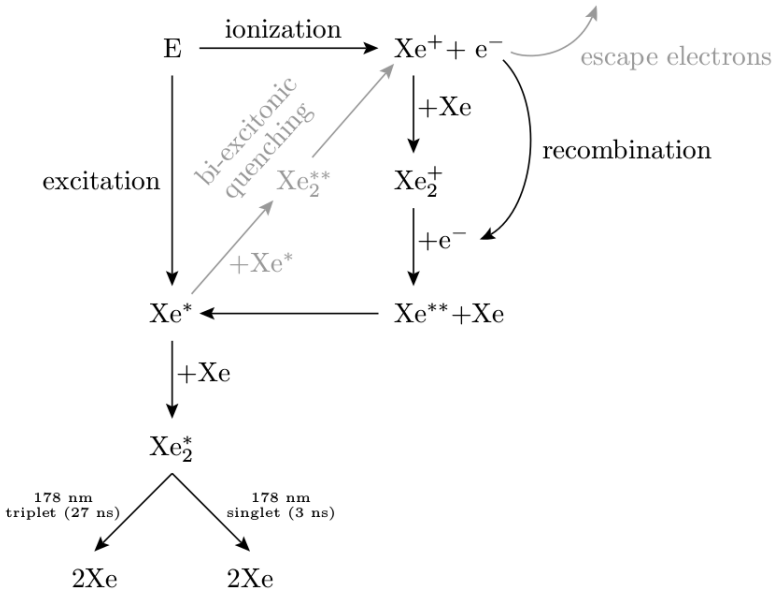

Figure 2.8: Scintillation mechanism in LXe (black) and different processes that can lead to the quenching of scintillation light (gray).

of the ionization signal in semiconductors, but it is however not in agreement with the observed scintillation yield at low energies in liquid xenon [48]. If both scintillation and ionization signals are taken into account, the Lindhard prediction is compatible with the observed quenching. In fact, the lower scintillation yield is due to a different fraction of energy that goes into ionization instead of scintillation [49]. Since a direct measurement of the Lindhard factor is complicated, the experimental quantity that is considered is the relative scintillation efficiency of nuclear recoils $\mathcal{L}_{eff}$ (already discussed in Section 2.3.1).

2.3.4 Anti-correlation

The application of an external electric field in the liquid drastically reduces the recombination probability of electron-ion pairs, resulting in a reduction of a scintillation signal and as a consequence increasing the charge signal [35]. The scintillation quenching due to electric field is even stronger for electron recoils. In fact, while in higher ionization density tracks like those of nuclear recoils more electrons can still recombine even in presence of a strong electric field, the electron recoil tracks with lower ionization density are much more affected by electric field. This is actually the basis of electronic and nuclear recoil discrimination capability of noble liquids (Section 3.1.2).

When an external electric field E is applied, the *relative scintillation yield* $S(E)/S_0$ is the resulting scintillation yield relative to that at zero field S_0, while the *relative charge yield* $Q(E)/Q_0$ is the charge collected relative to the one at infinite field (*i.e.* without recombination). Again,

the dependence from the electric field is explained by the different rate of recombination, that is related to the ionization density of the track: a strong recombination occurs at low fields and in more dense tracks. In fact, when the electric field increases the recombination is suppressed due to the fact that free electrons, generated by ionization, are drifted in the electric field and collected as a charged signal, while if the ionization density is high the recombination is favored and the observed ionization electrons tends to be reduced. A theory that keep into account these complex processes, combining ionization and scintillation in an electric field, is the Thomas and Imel model [49]. At high fields, the scintillation light yield for ERs is less than 40% the one with zero field. Figure 2.9 shows the experimental results of the scintillation and ionization quenching factors for nuclear and electron recoils as function of the electric field [50].

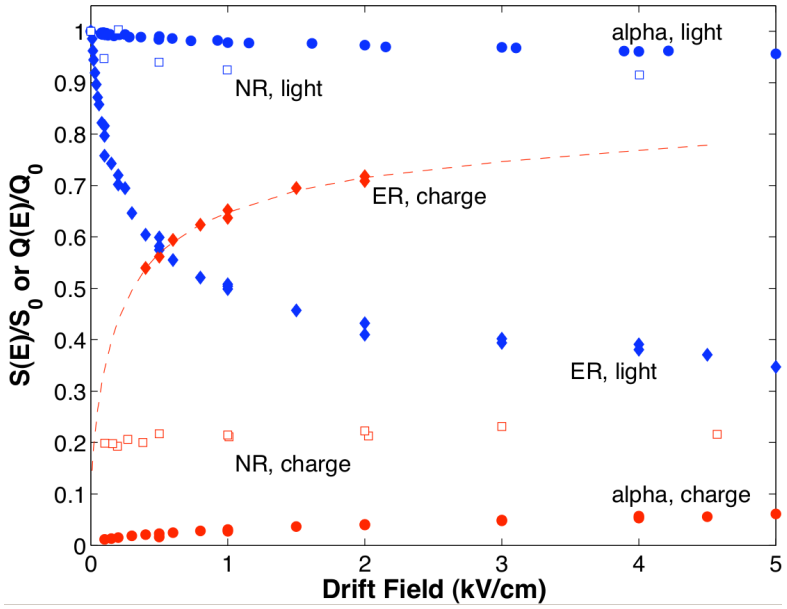

Figure 2.9: Field dependence of relative scintillation (blue) and ionization (red) yield in liquid xenon for 122 keV electron recoils (ER), 56 keVr nuclear recoils (NR) and α.

It has been measured that for a certain electron recoil energy and at a given electric field, the smaller scintillation light signal in liquid xenon is always accompanied by a larger ionization yield [51]. This phenomenon of anti-correlation between ionization and scintillation signals makes possible to improve the energy resolution in a liquid xenon detector. The anti-correlation of ionization and scintillation fluctuations has been measured for different energy of γ rays, giving an improvement to the energy resolution of liquid xenon, that has reached to the level predicted by the Fano factor [52].

Chapter 3

The XENON project at LNGS

The Time Projection Chamber (TPC) is a detector that uses an electric field in order to reconstruct a three-dimensional position of an event and to measure the energy deposited. The dual-phase (liquid and gas) xenon TPC exploits both scintillation and ionization signals; since the sum of light and charge is constant with applied electric field, a combined analysis on the photons emitted from the noble liquid and the number of collected electrons is used in order to improve the energy resolution. For dark matter searches, at keV energies, the dual-phase TPC additionally provides a discrimination between nuclear and electron recoils.

The XENON project is a dark matter direct search detector, based on a dual-phase TPC. It started with the prototype XENON10 [53, 54], located at Gran Sasso National Laboratories (LNGS), Italy, at an average depth of 3600 m water equivalent, that reduces the muon flux (from cosmic rays) by a factor 10^6 [55]. The subsequent detector XENON100, 100 kg mass scale, set in 2012 the most stringent limit for spin-independent elastic WIMP-nucleon scattering, with a minimum cross section of 2.0×10^{-45} cm^2 for a WIMP mass of 55 GeV/c^2, at 90% confidence level (C.L.) [56]. During the operation of XENON100, the design and construction of the largest dark matter direct search detector using noble liquid, XENON1T (1 ton mass scale), has started. XENON1T has set this year the best limit for spin-independent elastic WIMP-nucleon scattering, to 7.7×10^{-47} cm^2 cross section for a 35 GeV/c^2 WIMP mass at 90% C.L. [58]. Most of the subsystems of the XENON1T experiment have been designed such that it can easily be upgraded to an instrument featuring more than 7 tons of LXe.

In this Chapter we explain the detection principle of a direct dark matter experiment using a dual-phase TPC filled with xenon, and the results from the XENON project.

3.1 A dual phase TPC as a particle detector

The core of a dark matter direct search detector is the dual-phase TPC (liquid and gaseous phase), mostly filled by noble liquids, here xenon, and a smaller layer of noble gas in the top part. A schematic view of the dual phase TPC filled with xenon is reported in Figure 3.1.

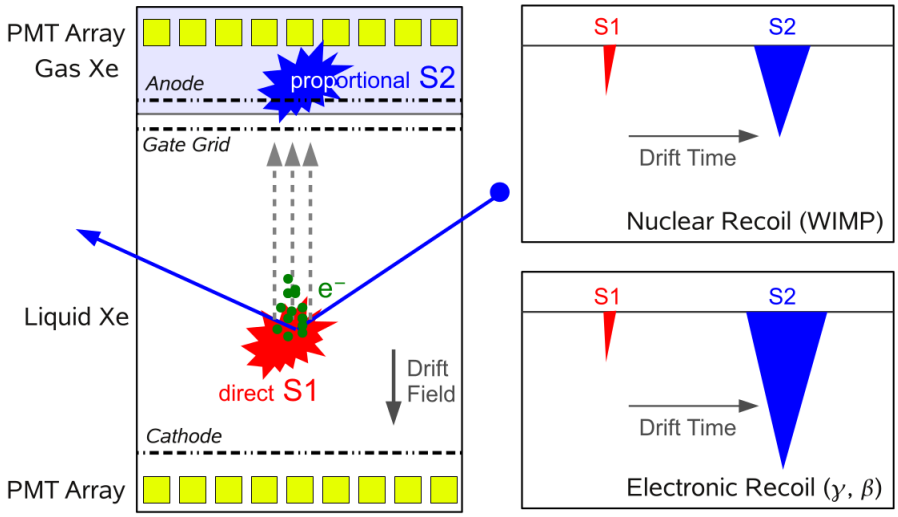

Figure 3.1: Left: working principle of a dual phase TPC. Right: waveform of a NR event (top) and ER event (bottom), whose S2/S1 ratio is the basis for background rejection.

A particle interacts in the TPC with liquid target through scattering off the xenon nuclei (neutrons or WIMP particles), also called *nuclear recoil* NR, or off the atomic electrons (γ rays or electrons), also called *electron recoil* ER. Then, the recoils produce excitation, ionization (with the subsequent recombination) and in case of NR some energy converted into heat is lost; the partition into different channels depends on the type of the recoil and is the base for the nuclear and electron recoil discrimination (Section 3.1.2). The resulting scintillation signal from excitation and recombination is called *direct*, or *primary signal* (S1). An electric field is applied across the LXe volume, drifting the ionization electrons surviving the recombination away from the interaction site. Electrons which reach the liquid-gas interface are extracted into the xenon gas, where a stronger electric field ($\gtrsim 10^3$ kV/cm generated between the gate at ground potential and the positively biased anode), induces an avalanche of the order of several hundred electrons. Then, at lower strength of the electric field, the multiplied electrons that collide with xenon nuclei excite the atoms, with the consequent emission of linear electroluminescence (gain factor of about 5 photons per electron). The scintillation produced is called *secondary*, or *proportional scintillation* (S2).

In both the S1 and S2 signals the scintillation light of 178 nm comes from the de-excitation of Xe_2^* dimers. The TPC is arranged by a top and a bottom array of PMTs, in direct contact respectively with GXe and LXe. Since LXe has a higher index of refraction than in the gas phase ($n = 1.69$ [37]), the direct scintillation will undergo total internal reflection at the liquid-gas interface, then it is mostly detected by the bottom PMT array.

The vertex of the interaction can be 3-dimensionally reconstructed. The $(x - y)$ position is reconstructed by the pattern distribution of the proportional scintillation in the PMT array. Since the S2 signal is generated at a well defined spot in the liquid-gas interface, very close to the top PMT array, the light is collected here by few PMTs while it is more homogeneously distributed over the bottom PMT array; then, in order to improve the position resolution to some millimeters, it is preferable to consider the signal from the bottom array only, namely $S2_b$. The z coordinate (along the drift field) is computed from the time difference between the signals $S1$ and $S2$, once known the electron drift velocity in the liquids, with about a millimeter of resolution.

Signal correction

The light collection efficiency depends on several factors, such as the solid angle coverage of the PMTs, the average number of reflections before a photon hits a photocathode, the PMT quantum efficiency, *etc*, and hence is a function of *(x-y-z)* coordinates. As a consequence, the TPC response looks not uniform along the *(x-y-z)* axes, mostly for S1. In order to correct for this effect, a monoenergetic light signal from a source homogeneously distributed inside the TPC volume is employed (usually 32.1 keV conversion electrons from the isotope ^{83m}Kr). The light yield distribution of xenon is calculated in several slices of *(x,y)* (or *(r,z)*) and its average value is used to construct a correction map. Also a dependence from the azimuthal-angle ϕ has been investigated, but its contribution is shown to be negligible. Then, when we use the *cS1* symbol, it means the S1 signal corrected by the light correction map. Figure 3.2 shows the light correction map obtained in XENON100 from the detector response to 40 keV line from inelastic neutron scattering on ^{129}Xe [59].

As already discussed in Section 2.3.2, during the electron drift toward the extraction field, electrons can be captured by electronegative impurities concentrated in LXe (such as H_2O, O_2, *etc.*). The electron lifetime τ_e is a measurement of the target purity and strongly influences the proportional scintillation signal:

$$S2(t) = S2_0\, e^{-t/\tau_e}\,, \tag{3.1}$$

where t is the time of the interaction, $S2(t)$ is the corresponding proportional signal and $S2_0$ is the absolute proportional signal, assuming zero impurities. Then, per each event, one has to correct S2 by the exponential factor ($cS2_b$). In order to improve τ_e the LXe is continuously

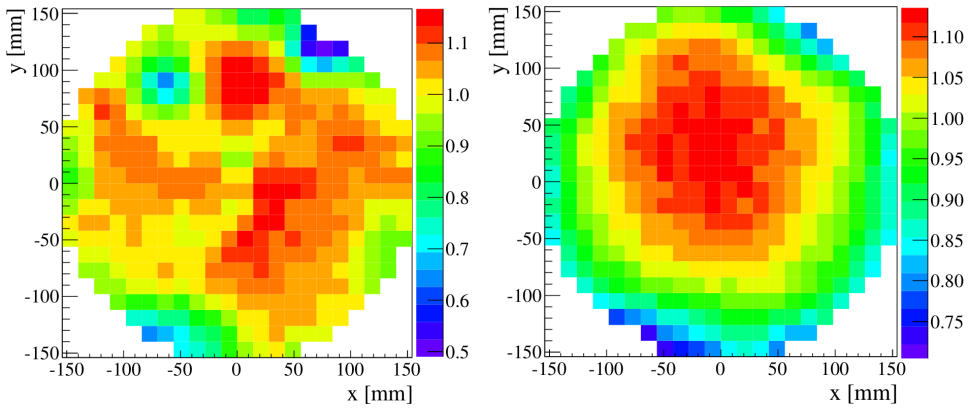

Figure 3.2: Light collection map measured with the 40 keV line from inelastic neutron scattering on ^{129}Xe for the top (left) and bottom (right) PMT arrays.

circulated and purified and unless there is an increasing of outgassing from materials, the electron lifetime grows with time. As example, the evolution of the electron lifetime in XENON1T over the first science run is shown in Figure 3.3. The two step-like decreases are due to the stop in the recirculation system, in order to allow for detector operations [60].

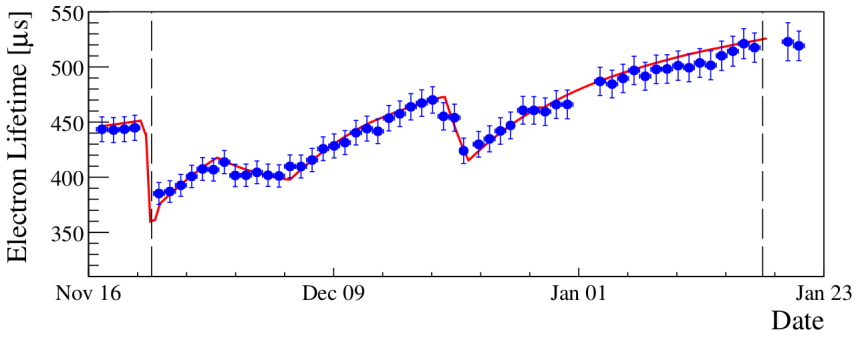

Figure 3.3: Evolution of the electron lifetime in XENON1T over the first science run (the red line is the fit function).

Detector design

In XENON, the almost uniform drift field inside the TPC is generated between a cathode, located in the bottom, and the gate at ground potential in the top, while the extraction field is obtained between the gate and the upper anode. The liquid-gas interface of xenon stands between the gate and the anode, where the extraction field acts. Moreover, screening electrodes are placed just in front of the two PMT arrays, in order to protect the PMTs from the electric field. The electrodes have been designed for high S1 light collection efficiency by maximizing the

optical transparency of the gate, the cathode and the bottom screening mash.

When the detector is operating, it is important to keep the liquid level of xenon very stable, using a diving bell made of stainless-steel, surrounding the top PMTs and the gate grid. The diving bell is directly pressurized by a controlled gas flow in order to handle the liquid-gas interface of xenon, while outside the bell the liquid can be arbitrarily high. This made it possible to fill the vessel up to about 4 cm above the bell, enabling a 4π coverage of the TPC with an instrumented veto of liquid xenon.

Electronegative impurities (*i.e.* H_2O or O_2) are kept below the ppb level (10^{-9}) by a constant recirculation of the xenon. LXe is taken from the bottom of the cryostat and evaporates in a heat exchanger system, which removes impurities by forming chemical bonds with getter material. Then, the purified xenon in gas phase is injected on the top of the TPC. Checks on the xenon purification are performed by weekly calibrations, from which one extract the electron lifetime in different moments.

A reliable and easy handling cooling system with very good stability is required for any dark matter experiment operating at cryogenic temperatures. In case of xenon, it is liquefied inside the TPC and kept at its operating temperature of -96°C through a Pulse Tube Refrigerator, based on a system of helium compression that uses a Stirling cycle. A copper cold finger is connected to the PTR and reaches the xenon volume, allowing to adjust fluctuations in temperature. LXe is extracted from the bottom of the detector, purified in gas phase, and introduced back as GXe into the diving bell. The boil-off xenon gas that reaches the cold-finger of the PTR becomes here liquefied; the liquid drops flow into the detector sliding in an insulated pipe inclined by 5°. In case of emergencies, a valve on the backup liquid nitrogen (LN_2) line connected with the TPC will be opened, freezing the xenon inside for few ours. A scheme of a typical cryogenic system operating with xenon (taken from XENON100 [59]) is shown in Figure 3.4.

Some detectors employ also an *active veto of LXe*, that lowers the event rate in the target and reduces the rate of accidental coincidences to a negligible level, thanks to the self-shielding capability of liquid xenon. The active LXe veto is constituted by a thickness of xenon all around the TPC and is equipped by PMTs, optically separated from the TPC by interlocking light-tight panels. Those panels surround the TPC and are made of PTFE, chosen for its properties both as insulator and good reflector of the VUV scintillation light [61].

In order to check the stability of detector parameters, such as light yield, charge yield, electron lifetime, position correction map, *etc*, calibrations with external sources are performed. For ER calibrations are usually employed γ rays from ^{228}Th, ^{127}Cs and ^{60}Co, while for NR calibrations neutrons from ^{241}AmBe.

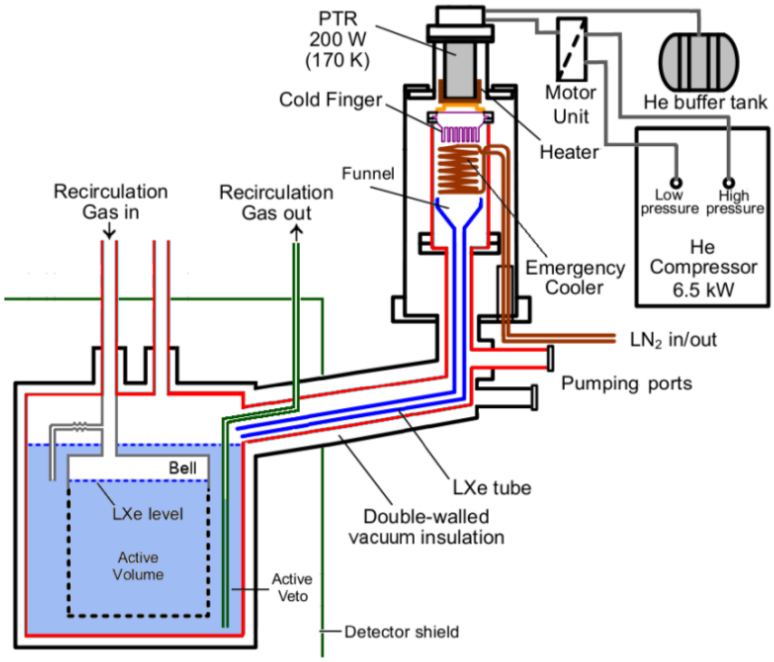

Figure 3.4: Scheme of the XENON100 cryogenic system.

Background contributions

In order to reach competing sensitivity with dark matter direct detectors, the background has to be minimized. We can mainly distinguish three types of background:

- *internal background*: is due to the radioactivity contained in the materials used to build the detector; it mostly induces ER.
  The internal background is primarily dominated by γ rays of the decay chains of ^{238}U, ^{232}Th, ^{40}K and ^{60}Co. It is reduced by a careful selection of all detector materials of the TPC with very low level of radioactive contaminations. Moreover, most of the materials which are in contact with xenon (all component of the TPC, the inner vessel of the cryostat and the connection pipes, the cryogenic and purification system) were additionally selected for a low ^{222}Rn emanation rate. Screening facilities are used to measure the intrinsic background and predict the overall rate.

- *intrinsic background*: is due to xenon contamination by the radioactive ^{85}Kr; it mostly induces ER.
  The ^{85}Kr has an isotropical abundance of ^{85}Kr/^{nat}Kr$\sim 10^{-11}$, decays via beta-decay with an endpoint of 687 keV and has a half-life of 10.76 y. Commercial xenon gas contains a concentration of ^{nat}Kr at the ppm level. As an example, for the ^{85}Kr-induced background to be subdominant one should reach a concentration in XENON100 of ^{nat}Kr/Xe$\sim$100 ppt (part per trillion) [62]. The Kr concentration

in xenon is reduced by using a distillation system based on the different boiling temperature of xenon (165 K at 1 atm) and krypton (120 K at 1 atm). The volatile Kr is collected at the top of the distillation column, while the Kr-depleted xenon at the bottom.

- *external background*: is due to the radioactivity coming from the rock and the muon-induced neutrons; they mostly induce NR.
  A shield of water can be used to suppress the neutron and gamma flux from rock radioactivity.
  The muon-induced neutrons, due to muon spallation of nuclei or electromagnetic and hadronic cascades generated by muons, have enough energy to reach the TPC and produce the same signal as expected by WIMPs. In order to tag those events, the water shield can be instrumented with photomultipliers, acting also as a Cherenkov active muon veto (see Chapter 6).

3.1.1 Combined Energy Scale

It is possible to summarize the interaction phenomenon in noble liquids as follows: when a ionizing particle crosses the medium, both the ionization and excitation processes occur. In order to perform a measurement we have to translate this processes in a measurable signal, that is, in this case, the charge and light yield respectively. When a γ or β particle hit a liquid xenon target, its energy is converted into a measurable signal, meaning there is no quenching effect (usual in NRs). Since fluctuations in ionization and scintillation are anti-correlated, one can construct a linear energy scale in which the recombination fluctuations are canceled by adding the two signals [57]. This ER energy scale is called *Combined Energy Scale* (CES). It shows the total energy and hence, must be field-independent, while the individual scintillation and ionization yield depend by electric field.

The photon detection efficiency, also called *primary scintillation gain* g_1, is the conversion between photons and S1 photoelectrons and takes into account the light collection efficiency (LCE) and the PMT quantum efficiency:

$$g_1 = \frac{cS1}{n_\gamma}\,. \tag{3.2}$$

The electron detection efficiency, also called *secondary scintillation gain* g_2, is the conversion between electrons and S2b photoelectrons and takes into account the extraction efficiency and the electron-multiplication due a strong electric field:

$$g_{2b} = \frac{cS2b}{n_e}\,. \tag{3.3}$$

Then, the Combined Energy Scale obtained from an ER can be written as:

$$CES = W\,(n_\gamma + n_e) = W\,(\frac{cS1}{g_1} + \frac{cS2_b}{g_{2b}})\,, \tag{3.4}$$

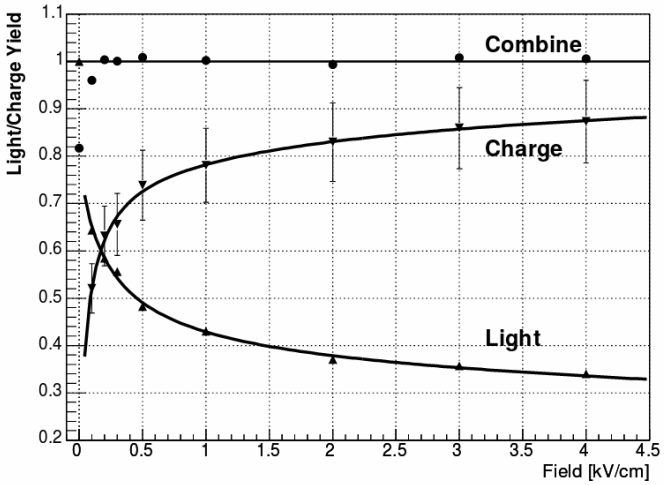

Figure 3.5: Light and charge yield, relative to the value at zero field, as a function of drift field for 662 keV γ rays from ^{137}Cs.

where W=13.7 eV is the energy required to produce a quantum (γ or electron). From this equation is even more clear that the two observables are anti-correlated. Figure 3.5 shows the relative light and charge yield referred to the value at zero field of 622 keV γ rays from ^{137}Cs, together with the sum of the two quantities, that should be by definition equal to 1 at each field [52].

Moreover, an example of the energy reconstruction of the 662 keV γ line from ^{137}Cs using the S1 (12.5% 1 σ resolution), the S2 (6.5% resolution) signal separated and the CES (2.3% resolution) from XENON100 experiment is shown in Figure 3.6 [59]. The great advantage of improving

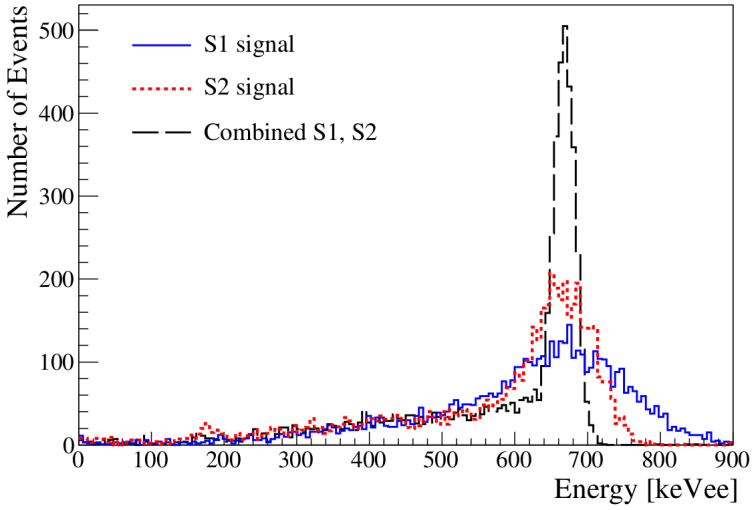

Figure 3.6: Energy reconstruction of the 662 keV γ line from ^{137}Cs using the S1, the S2 signal separated and the CES.

in the energy resolution when using the CES with respect to the S1 or S2

signal only (for instance, it allows to separate the lines from radioisotope decays) looks clear from the plot. Thus, the combined energy scale is typically used for comparison of background spectra with Monte Carlo predictions.

Nuclear-Recoil equivalent energy

For NRs the quenching effect of the charge yield is less visible than for ERs (as shown by the relative charge yield in Figure 2.9). In fact, since the quenching depends on the track density, in case of α particles and NRs the drift field can move only a fraction of ionization electrons from the track core.

Moreover, part of the energy released by the impinging particle is lost into heat (nuclear quenching), meaning it is not possible to define a Combined Energy Scale for NRs in the same way as for ERs. Then, the reconstruction of the NR energy, or *nuclear recoil equivalent energy* E_{nr}, is usually computed from the direct scintillation signal S1:

$$E_{nr} = \frac{S1}{L_{y,er}} \frac{1}{\mathcal{L}_{eff}} \frac{S_{er}}{S_{nr}}, \tag{3.5}$$

where S_{er} and S_{nr} are the scintillation light field quenching factors for ERs and NRs respectively, $L_{y,er}$ is the usual light yield referred to 122 keV γ ray and $\mathcal{L}_{eff}$ is the relative scintillation efficiency. The obtained energy is tagged with the unit keV_{nr}. In XENON100 for instance, we got: $L_{y,er}$=(2.20±0.09) PE/keV, S_{er}=0.58 and S_{nr}=0.95 [50].

Electron-Recoil equivalent energy

When we calibrate a detector with γ or β sources, the detector response in terms of charge collected or secondary scintillation signal is converted into energy. Since these particles are responsible for ER events, we call this energy *electron recoil equivalent energy* and tag it with the unit keV_{ee}.

3.1.2 Discrimination band

As already mentioned, the different track left by a nuclear or electron recoil allows us to determine the nature of the impinging particle. In fact, α particles, neutrons or WIMPs transfer a large fraction of their energy to the nuclei of the medium, whose recoil leaves a high ionization density track, where more electrons can still recombine even in presence of a strong electric field. On the other hand, in ERs, due to electrons and γ, the energy of the impinging particle is transfered to the atomic electrons, and the following ionization density track is smaller than in NR case, such that the recombination process is strongly quenched in presence of electric field.

The different recombination probability among the two processes results in an bigger direct signal S1 in case of nuclear recoils, and bigger proportional signal S2 for electron recoils. Thus, the different charge-to-light ratio is used to discriminate nuclear ($S2/S1_{WIMP}$) and electron ($S2/S1_{e^-}$) recoils. In particular, the ratio $S2/S1$ for nuclear recoils is lower than for electron recoils:

$$S2/S1_{WIMP} < S2/S1_{e^-} \,. \tag{3.6}$$

The distribution of electron and nuclear recoil from XENON100 calibration data is shown in Fig 3.7. The discrimination parameter used here is $\log_{10}(\mathrm{S2}_b/\mathrm{S1})$ shifted by the median of the ER band (also called *flattened band*). The efficiency to reject ER background is around 99.5% at 50% nuclear recoil acceptance.

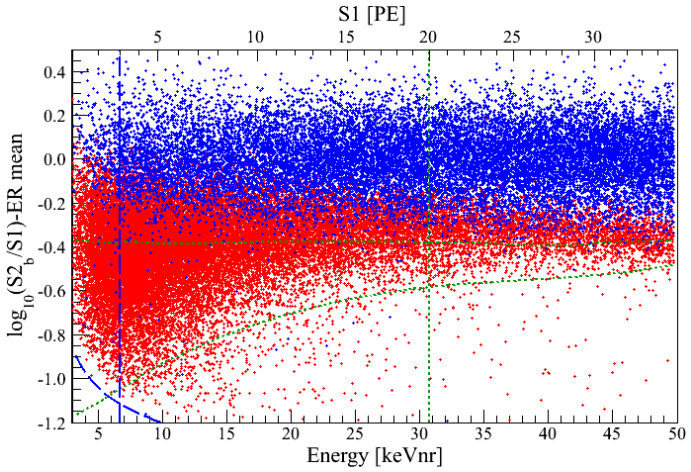

Figure 3.7: Distribution of electronic recoils (blue) and nuclear recoils (red) from XENON100 calibration data in the discrimination parameter space $\log_{10}(\mathrm{S2}_b/\mathrm{S1})$.

3.1.3 Pulse shape discrimination

The scintillation light curve of xenon has two different components, due to singlet and triplet states. In particular, the singlets and triplets decay times depend on the density track produced by impinging particles and the ratio of singlet to triplet states (I_s/I_t) is larger at higher deposited energy density [63]. One explanation of this mechanism is that the ionization electrons before the recombination can collide with a singlet state, inducing a transition to the triplet state (*i.e.* superelastic collisions with thermal electrons). The probability of this process is inversely proportional to the recombination time, that is function of the ionization density.

The difference in the scintillation pulse decay shape for different kind of particles can be used to effectively discriminate the nature of the ionizing radiation, with a so called *Pulse Shape Discrimination* (PSD). The

singlet states are favored in higher density tracks, left by NRs due to neutrons and WIMPs, while they are reduced in the case of lower density tracks, left by ERs due to electrons and γ:

$$(I_s/I_t)_{NR} > (I_s/I_t)_{ER}\,. \tag{3.7}$$

The pulse shape discrimination is quite difficult for liquid xenon, due to the small time separation between singlet and triplet decay components. In liquid argon the PSD is more effective, able to to distinguish ERs from NRs down to nuclear recoil energies of 50 keV with a rejection power of about 10^6 [64], that is anyway required to suppress the large background due to ^{39}Ar (β emitter) present in atmospheric Ar.

3.1.4 SI and SD interactions

The interaction of WIMPs with nuclei can be divided between scalar, or *spin independent* (SI), and axial-vector, or *spin dependent* (SD) interactions.

In case of scalar interactions, the WIMP scatters coherently with the whole nucleus and the SI cross section scales as A^2 (where A is the number of nucleons).

If the WIMP is a spin-1/2 or a spin-1 field, the contributions to the WIMP-nucleus scattering cross section arise from couplings of the WIMP with a quark axial current. The SD differential WIMP-nucleus cross section as a function of momentum transfer q is [67]:

$$\frac{d\sigma_{SD}(q)}{dq^2} = \frac{8G_F^2}{(2J+1)v^2} S_A(q)\,, \tag{3.8}$$

where G_F is the Fermi constant, v is the WIMP speed relative to the target, J is the total angular momentum of the nucleus and S_A is the axial-vector structure function. If the momentum transfer is zero, the structure function become:

$$S_A(0) = \frac{(2J+1)(J+1)}{\pi\, J} \left[a_p\langle S_p\rangle + a_n\langle S_n\rangle\right]^2\,, \tag{3.9}$$

where $\langle S_{p,n}\rangle = \langle J|\hat{S_{p,n}}|J\rangle$ are the expectation values of the total proton and neutron spin operators in the nucleus, and the the effective WIMP couplings to protons and neutrons are defined in terms of the isoscalar a_0=a_p+a_n and isovector a_1=a_p-a_n couplings. Since xenon has two isotopes with non-zero nuclear spins, it is possible to detect SD interactions also. In particular, natural xenon contains ^{129}Xe, spin 1/2 and ^{131}Xe, spin 3/2, with an abundance of 26.4% and 21.2% respectively. Figure 3.8 shows the sensitivity (from XENON100 [65]) for neutron couplings and proton couplings. XENON100 took data for 224.6 live days setting the most stringent limit on WIMP-neutron SD scattering, to 3.5×10^{-40}cm^2 cross section for a 45 GeV/c^2 WIMP mass at 90% C.L.

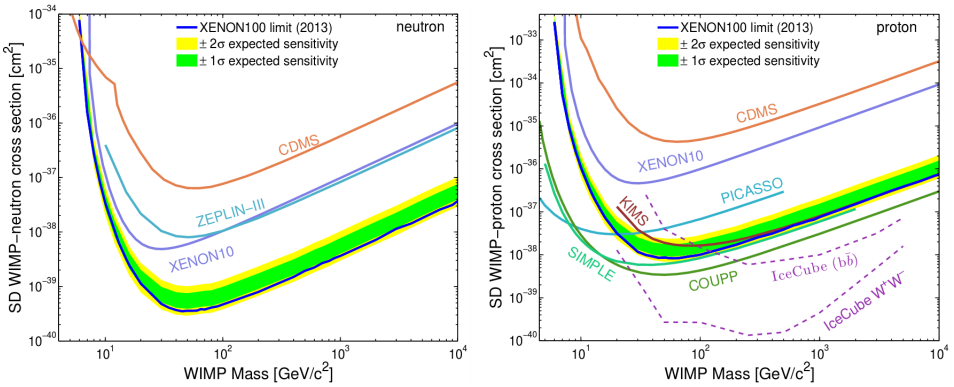

Figure 3.8: Upper limit on the WIMP SD cross section on neutrons (left) and protons (right) obtained with XENON100.

3.2 Nuclear form factor

The nuclear form factor $F(q)$ is a correction to the theoretical scattering cross section of particles from point-like target nuclei with infinite mass: $\sigma = \sigma_0 F^2(q)$, where σ_0 is the cross-section at zero momentum transfer. In fact, when the momentum transfer $q = \sqrt{2M_T E_r}$ (where M_T is the target mass) is such that the De Broglie wavelength $\lambda = h/q$ is comparable to the nuclear radius R, the diffraction occurs. It means that the effective cross-section falls down with increasing momentum transfer; this effect is significant for target media with large atomic mass, in particular for xenon atoms.

The nuclear form factor is defined as the Fourier transform of the nuclear mass density distribution $\rho(\mathbf{r})$:

$$F(\mathbf{q}) = \int_V \rho(\mathbf{r}) e^{i\mathbf{q}\cdot\mathbf{r}} d\mathbf{r} = \frac{4\pi}{q} \int_0^R r \sin(qr)\rho(r) dr \,, \tag{3.10}$$

where the last part assumes the integration in cylindrical coordinates in case of isotropic distribution, so that $F(\mathbf{q}) \equiv F(q)$ [66].

The nuclear form factor is different in case of SI and SD interactions. In fact, according to the *odd-group model*, the non zero nuclear spin is carried only by the nuclei with unpaired number of protons or neutrons [67]. The Helm parametrization on the mass density distribution, that approximates the nucleus to a solid sphere with a skin thickness $s \approx 1$ fm [68], is used to derive the SI interaction form factor:

$$F_{SI}(q) = 3\frac{j_1(qR)}{qR} e^{-\frac{(qs)^2}{2}} = 3\frac{\sin(qR) - qR\cos(qR)}{(qR)^3} e^{-\frac{(qs)^2}{2}} \,, \tag{3.11}$$

where $j_1(qR)$ is the spherical Bessel function and $R = \sqrt{c^2 + \frac{7}{3}\pi^2 a^2 - 5s^2}$ (with $c = 1.23A^{1/3}$ fm and $a \approx 0.52$ fm). In case of SD interactions, a simplified approach describes the form factor as obtained by the Fourier

transform of a thin shell, approximating a single outer shell nucleon:

$$F_{SD}(q) = j_0(qR) = \frac{\sin(qR)}{qR}\,, \tag{3.12}$$

where $j_0(qR)$ is the zero Bessel function and $R \approx 1.0A^{1/3}$ fm. A more exact computation has been provided by Engel *et al.* in the experimental useful range $0 < qR \leq 6$ [67].

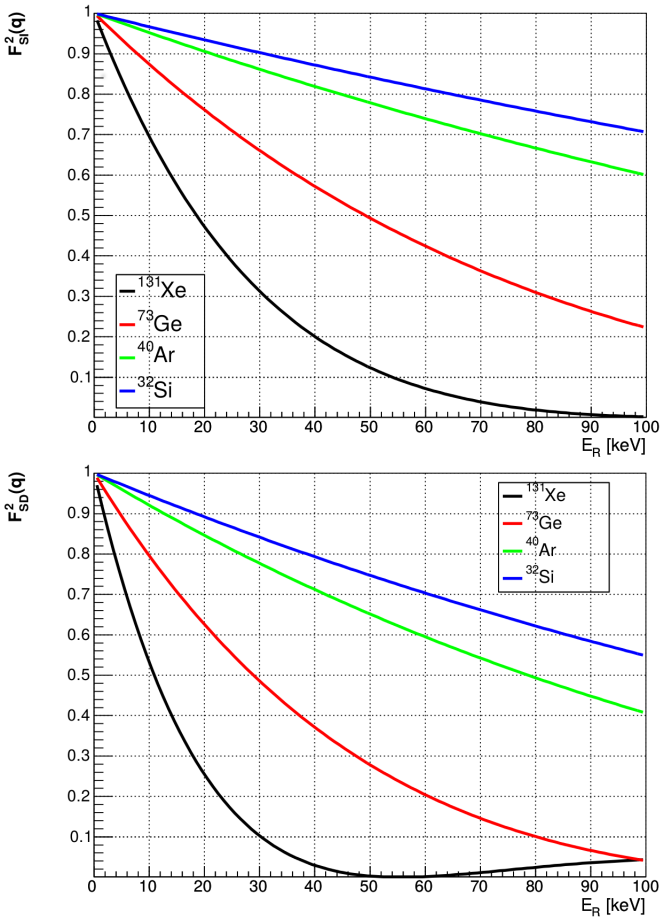

Figure 3.9: Spin-independent (top) and -dependent (bottom) nuclear form factor for several materials.

The SI and SD nuclear form factors from the above equations are plotted in Figure 3.9 for different target materials [69]. It is important to notice that in xenon $F^2(q)$ falls off quickly, thus a low energy threshold is essential to minimize the effect of the suppressed rate due to the form factor.

3.3 The XENON project

The XENON project is intended for direct dark matter detection. It is located at Gran Sasso National Laboratories, Italy, at an average

depth of 3600 m water equivalent, that reduces the cosmic muon flux by a factor 10^6.

In order to increase the sensitivity to WIMP-nucleon scattering cross section, the project has passed through three stages with increasing target mass: the prototype XENON10, the following XENON100 and the operating XENON1T. The last detector will be able to be upgraded soon into XENONnT. Figure 3.10 shows where the experiments are located at the underground laboratories.

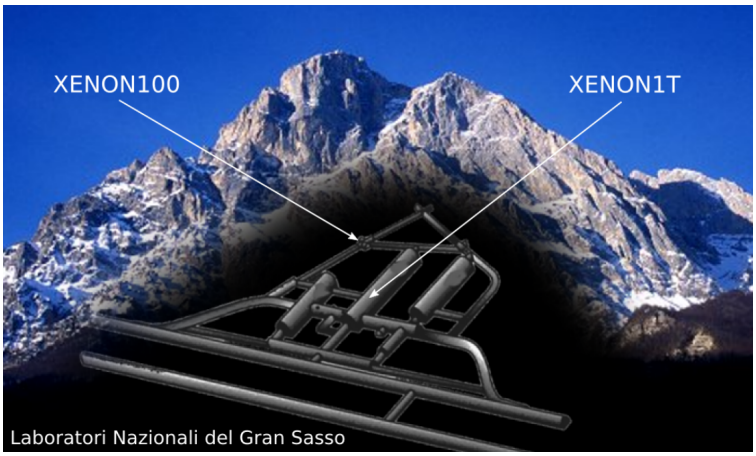

Figure 3.10: Location of the XENON100 (the same as XENON10) and XENON1T experiment at LNGS, where 3600 m water equivalent offers low-background conditions for the rare-event searches.

3.3.1 XENON10

XENON10 is the prototype of the project. Started in 2006, it has been designed to test the XENON concept and verify achievable threshold, background rejection power and sensitivity. The TPC dimensions were 20 cm in diameter and 15 cm in height. The detector contained 15 kg total mass of xenon, viewed by 89 1-inch PMTs [70].

After a blind analysis of 58.4 live days of data, using 5.4 kg fiducial mass, XENON10 set the best limit at that time on WIMP-nucleon SI cross section to 4.5×10^{-44} cm^2 [53] and on WIMP-neutron SD cross section to 5×10^{-39}cm^2 at a WIMP mass of 30 GeV/c^2 at 90% confidence level [54].

3.3.2 XENON100

XENON100 consisted of a new TPC able to keep a factor of 10 more mass with respect to XENON10. It have been designed in order to fit inside the same passive shield as for XENON10, allowing to realize a fast upgrade of the experiment. It took data up to 2016; this work will treat also some aspects reguarding calibrations in XENON100.

Detector design

The almost cylindrical XENON100 TPC of 30.5 cm height and of 15.3 cm radius contained the 62 kg LXe target. 242 1-inch Hamamatsu PMTs, specially selected for low radioactivity [71], detected the light in the TPC; 98 of them were located in the top PMT array, arranged in concentric circles in order to improve the resolution of radial event position reconstruction. The PMTs with highest quantum efficiency (QE) have been placed in the bottom array of the TPC, where most of the photons from S1 signal are arriving, in order to maximize the light collection efficiency in the detector. A layer of liquid xenon surrounded the TPC on all sides and was observed by 64 PMTs (the same type as used for the TPC). In total, XENON100 contained 161 kg of LXe [59].

The electric field used for the normal operations was equal to 0.53 kV/cm (with the cathode at 16 kV), while the extraction field across the liquid-gas interface was about 12 kV/cm (with the anode at 4.5 kV), with an extraction efficiency close to 100%.

In order to reduce the external background, XENON100 had been equipped with a passive shield, the same as XENON10. The detector was surrounded, from inside to outside, by 5 cm of OFHC copper, followed by 20 cm of polyethylene, and 20 cm of lead, where the innermost 5 cm consisted of lead with a low contamination of ^{210}Pb. The entire shield rested on a 25 cm thick slab of polyethylene. An additional outer layer of 20 cm of water or polyethylene had been added on top and on three sides of the shield to further reduce the neutron background. Figure 3.11 shows a diagram of the passive shield, together with a picture when the shield has been opened showing the XENON100 cryostat. During detec-

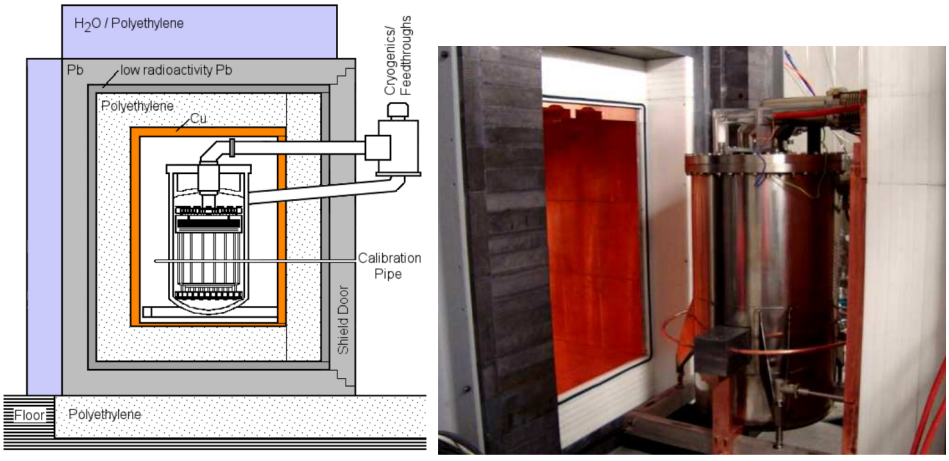

Figure 3.11: Diagram of the XENON100 passive shield (left) and picture of the opened door.

tor operation, the inner shield cavity was constantly purged with high purity boil-off nitrogen in order to avoid radioactive radon penetrating into the shield, that was maintained at a level below 1 Bq/m^3. Moreover,

the internal background had also been reduced by a careful selection of all detector materials regarding intrinsic radioactivity [71], a xenon target with lower ^{85}Kr contamination and a novel detector design leaving only low radioactive components close to the target. Finally, XENON100 featured an active veto of 99 kg of liquid xenon viewed by 68 PMTs. The cryostat had been filled with xenon up to 4 cm above the bell, enabling a 4π coverage of the TPC.

Results

During its long operation between 2008 and 2016, XENON100 achieved the world-best at the time experimental results in the detection of WIMPs, but has also been in axions search [72], investigation of leptophilic dark matter interacting with atomic electrons [73] and a long term electron recoil event rate modulation check [74]. Here we report some of the most important conclusions.

In 2012 XENON100 released the results of a blinded analysis on 224.6 live days $\times$ 34 kg exposure [56]: no evidence for dark matter interactions have been found. Actually, two candidate events have been observed in the nuclear recoil energy range of 6.6-30.5 keV$_{nr}$, but consistent with the background expectation of (1.0$\pm$0.2) events. Figure 3.12 shows the position of the two events inside the fiducial volume and in the flattened discrimination space. The detector has set the best limit at the time for the SI elastic WIMP-nucleon scattering with a minimum cross section of 2×10^{-45}cm^2 for a WIMP mass of 55 GeV/c^2 at 90% C.L. In the same dataset, a spin dependent analysis has been performed, releasing again the best limit at the time on the WIMP-neutron elastic cross section (Section 3.1.4). Moreover, a combined analysis over three runs summing up to 477 live days has improved the sensitivity by almost a factor 2 [75]. An ultralow electromagnetic background has been achieved, equal to about 5×10^{-3}events/keV$_{ee}$·kg·day before electronic recoil rejection.

3.3.3 XENON1T

XENON1T is the first of the new generation multi-ton scale dark matter detectors. The experiment is located in the Hall B of LNGS and a big water tank surrounding the cryostat allows to further reduce the external background (see Figure 3.13).

Detector design

The cylindrical TPC is 96 cm in length and 110 cm in diameter. A total amount of 3.2 t LXe fills the inner vessel of the cryostat, out of which 2.0 t of xenon target are contained in the TPC. The remaining xenon covers the diving bell and is mostly used as a passive shield from external radiations. Figure 3.14 shows the CAD drawing of the TPC. A total of 248 3-inches circular window Hamamatsu PMTs are used to

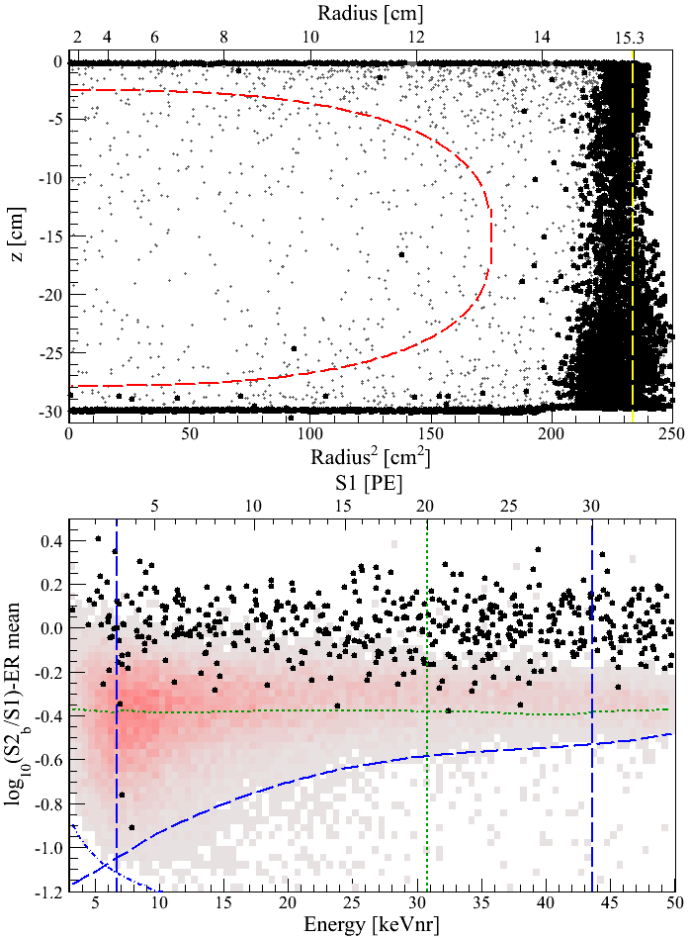

Figure 3.12: Top: spatial distribution of the events inside the TPC in the 6.6-43.3 keV$_{nr}$ energy region; the red dashed line delimits the 34 kg fiducial volume. Bottom: event distribution in the flattened discrimination parameter $\log_{10}(S2_b/S1)$. The blue dashed line indicates the 3-20 photoelectron threshold, while the gray dotted line is the mean of the NR band.

record the signals from the TPC. 127 of them are radially installed in the top array above the target, to facilitate radial position reconstruction, and 121 are packed as tightly as possible in the bottom array, to maximize scintillation light collection efficiency. The bottom PMTs in the central region of the array feature a higher quantum efficiency in order to maximize the position reconstruction capability of the detector. The PMTs have an average quantum efficiency of 34.5% at 178 nm and a single photoelectron acceptance of 92.5%. Once they have been installed in XENON1T, the average gain measured is 2.6×10^7 (including the factor related to the $\times10$ amplifier) and the dark rate resulted around 12 Hz for the top PMT array and 24 Hz for the bottom one. The PMTs give the highest contribution to the internal background; in order to reduce it, big efforts have been applied, together with Hamamatsu, to produce low-radioactivity PMTs [76].

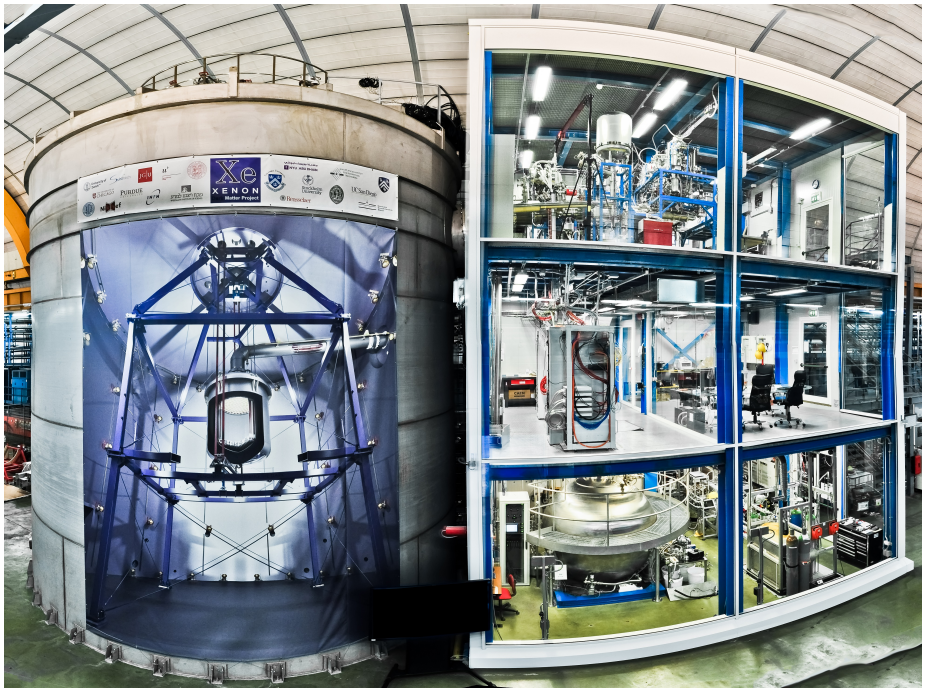

Figure 3.13: Picture of the XENON1T experiment, with the water tank (left) and the auxiliary systems (right) used for the maintaining of the detector.

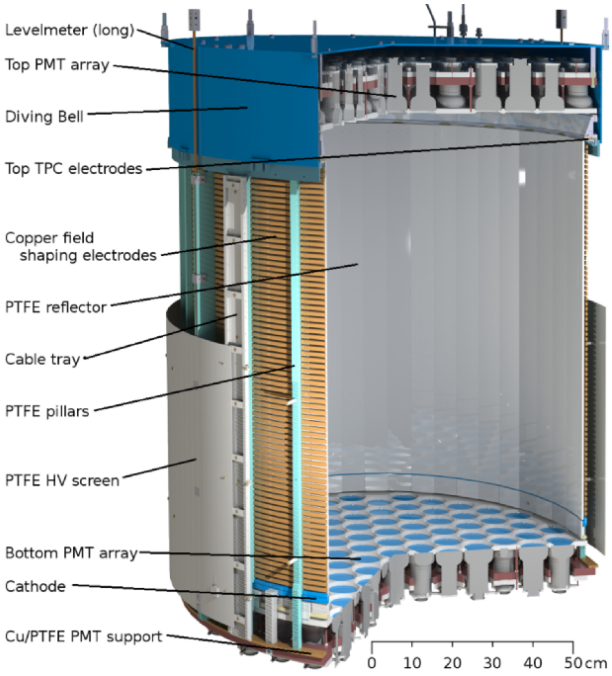

Figure 3.14: CAD drawing of the XENON1T TPC.

The electric field used for the first science run is 0.12 kV/cm (*i.e.* cathode at 12 kV) corresponding to an electron drift velocity of 1.44 mm/μs, while the extraction field across the liquid-gas interface is 10

kV/cm (*i.e.* anode at 4.0 kV).

Up to now, LXe detectors were filled by liquefying xenon from the gas phase, while the target was recuperated by evaporating it; this process requires too much time for multi-ton scale detectors and it is impossible to fastly recover in case of emergency. Then, a new cryogenic Recovery and Storage system for Xenon (ReStoX) has been developed. It consists of a vacuum insulated stainless steal sphere (2.1 m in diameter and 28 mm wall thickness) that allows to store up to 7.6 t of liquid or gas xenon, supporting a pressure up to 73 bars, see Figure 3.15. The recovery of xenon is done in liquid phase, via direct vacuum insulated lines and driven by the pressure difference in the system.

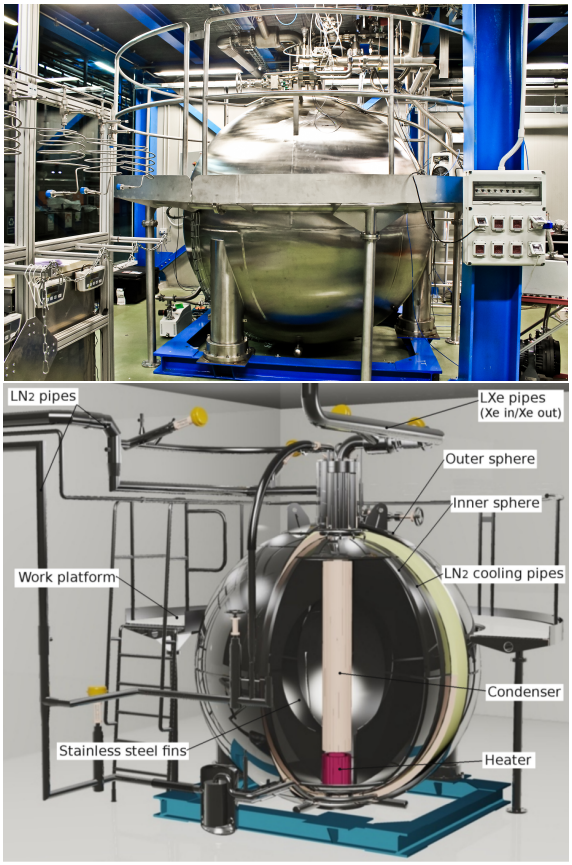

Figure 3.15: Picture (top) and CAD drawing (bottom) of the Recovery and Storage system for Xenon.

A big effort has applied to suppress the background, allowing to reach the best sensitivities. As already mentioned, the internal background is mainly due to the detector materials, that emanate ^{222}Rn; in order to suppress it, the materials used to build the TPC were selected for a low intrinsic radioactivity, tested with γ-spectroscopy and mass spectrometry. Before assembly, all components have been cleaned with several techniques, such as degreasing, passivation, bath in de-ionized water and ethanol, electropolishing. Moreover, the cleaning process and the assembly happened in a dedicated cleanroom. The highest contribution to

the internal background is given by PMTs, whose ^{222}Rn concentration is anyway at the level of 10 microBq/kg.

The muon-induced neutron background is reduced by a water Cherenkov detector surrounding the TPC, the *Muon Veto* (MV). It consists of a cylindric tank, 9.6 m in diameter and 10.2 m in height, filled with water and equipped with 84 8-inches photomultiplier tubes. The PMT quantum efficiency is around 30% in the wavelength range 300-600 nm and the average gain is 6.2×10^6 for typical voltages of 1500 V. In order to maximize the photon detection efficiency, the inner walls of the water tank have been covered by a reflective foil, that acts both as a more than 99% reflector between 400-1000 nm wavelength and a wavelength shifter to the PMTs higher QE value [77]. In case the MV has detected an impinging particle, the consequent event recorded by the TPC would be removed from analysis. Hardware setup, calibrations of the MV system and a muon analysis on the first XENON1T science run data have been part of the study carried out in this work (Chapter 6).

Due to the large self-shielding power of LXe, for multi-ton scale detectors the fiducial volume can not be reached by usual calibration sources located outside the TPC. In order to bypass this problem, for ER calibrations a ^{83m}Kr source (emitting γ rays of 32.1 keV and 9.4 keV) is injected in the purification system and reaches internally the TPC through recirculation. For NR calibrations, a neutron generator gun, based on the deuterium-deuterium fusion, is a source of neutrons with around 2.5 MeV and a flux tuned by setting the generator voltage [78].

Results

XENON1T has released the results from the first science run after 34.2 live days of exposure [58]. The run started on November 22, 2016, and ended on January 18, 2017, when an earthquake temporarily interrupted detector operations. The detector set the most stringent exclusion limit on the elastic SI WIMP-nucleon interactions, with a minimum cross section of 7.7×10^{-47}cm^2 for a WIMP mass of 35 GeV/c^2 at 90% confidence level. Figure 3.16 shows the sensitivity plot, together with the results from other experiments.

A total of 63 events have been found inside the WIMP energy region (3-70 PE in cS1 and 50-80000 PE in cS2): no one of them is within 10 ms from a muon veto trigger and only one is observed below the 50% NR discrimination band, that is anyway consistent with the background-only hypothesis. Moreover, the electronic recoil background is the lowest ever achieved in a dark matter detector, and is equal to $(1.93\pm0.25)\times10^{-4}$events/(kg·day·keV$_{ee}$) inside (1042±12) kg fiducial mass and in 5-40 keV$_{nr}$ energy range.

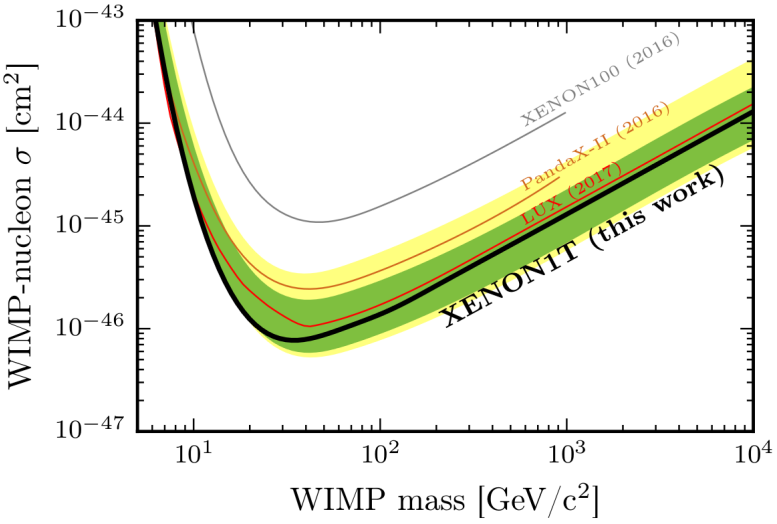

Figure 3.16: SI WIMP-nucleon cross section limits as function of WIMP mass at 90% C.L. obtained by XENON1T [58].

3.3.4 XENONnT

Most subsystems of XENON1T have been designed such that they can support also a significantly larger dark matter detector, with a target of around 7 tons, called XENONnT. In particular, all LXe handling systems, the detector support structure, as well as the outer cryostat are now already larger than required for XENON1T. In fact, the TPC is installed inside a double-walled, cylindrical stainless steel cryostat, leaving enough space between the inner and the outer vessel to accommodate the upgrade stage XENONnT as well. The cryogenic xenon recovery and storage system (ReStoX) manage to keep the required concentration of ^{nat}Kr/Xe (below 0.048 ppt) also for the XENONnT size of target material. Thus, the upgrade basically requires a higher number of PMTs (almost double the XENON1T ones) and electronics, about three times xenon mass with respect to XENON1T and a bigger inner vessel of the cryostat in order to contain it.

The idea of XENONnT is to allow for a quick move to a larger instrument after the science goal of XENON1T has been reached. If XENON1T find dark matter signals, XENONnT could better confirm them. In any case, XENONnT aims at improving the spin-independent WIMP sensitivity by another order of magnitude compared to XENON1T. At low WIMP masses, the sensitivity would approach the *neutrino floor*, caused by the coherent scattering of solar ^{8}B neutrinos off the xenon nuclei [79], which mimic the signal expected from WIMPs. The neutrino coherent scattering is an irreducible background and the only chance to further improve the sensitivity on the WIMP cross section will be to use new detection strategies such as, directional techniques.

Chapter 4

MC validation of Electron Recoils in XENON100

In this Chapter we focus on the electron recoils, due to electrons or gammas scattering off xenon electrons, inducing electromagnetic background. In fact, even though NRs, due to neutrons or WIMPs scattering off xenon nuclei, are of primary importance for dark matter search, a small fraction of ERs falling into the nuclear recoil discrimination band (see Section 3.1.2) can not be rejected and represents a dangerous background. Thus, a weekly campaign of ER calibrations is carried out during the detector operation and a detailed MC simulation that predicts the electromagnetic background is strictly required. The model used to predict the number of photons and electrons produced by a particle interacting with the detector is called Noble Element Simulation Technique (NEST). It consists in a phenomenological description of the xenon response to an ionizing radiation, through a collection of target-related parameters obtained by fitting up-to-date experimental results.

The MC has been validated through a comparison with calibration data in XENON100 from Xe activation lines by neutron inelastic scattering (from AmBe), ^{232}Th and CH_3T sources. The importance of a valid MC for ERs in a xenon-based TPC is of primary importance for XENON1T, where the large self-shielding power of the liquid xenon does not allow to reach the inner fiducial volume through usual calibration sources located outside the TPC.

4.1 MC description

The main software used for the Monte Carlo is Geant4 (*GEometry ANd Tracking*) [80], version 9.3.p02, a toolkit for the simulation of the passage of particles through matter, using object oriented programming, in C++. It is adopted by a large number of experiments in different fields of application, such as high energy physics, astrophysics and space science, nuclear and accelerator physics, as well as in studies regarding medical physics and radiation protection. Geant4 includes facilities for

handling geometry, tracking, detector response, run management, visualization and user interface. The physics processes cover a wide range (*i.e.* electromagnetic, hadronic and optical processes) and a large set of long-lived particles, materials and elements, over a large energy range, from few hundred of eV to the TeV scale[81].

Geant4 has been used in the first part of the MC simulation, when an incoming particle hits the target material, releasing a certain amount of energy per each step, fixed by the physics. The physics model used for scintillation is given by NEST, which predicts the number of photons and electrons produced by a particle hitting a xenon target. Once the full Geant4 MC simulation has been validated, a toy MC that reproduces the same output has been developed, in order to save time, disk-space and handle more easily the NEST parameters. For the second part of the MC simulation, related to the detector response, a external code (based on ROOT [82]) has been written. It was designed to convert photons and electrons into the measurable signals S1 and S2, considering the detector parameters such as the light collection efficiency, the quantum efficiency of the photomultipliers, the multiplication of electrons in the liquid-gas interface of xenon, *etc.* This code can also run directly on the toy MC without any modification, and provides as output, among other quantities, the light yield and the ER discrimination band (see next Sections).

4.1.1 The NEST model

As already mentioned, NEST [83, 84] is a dedicated code, based on the collection of models and experimental data, developed to describe both scintillation light and ionization yields in liquid xenon-based detectors as a function of particle type, its energy and the electric field. NEST provides a detector-independent description of the target response to incident radiation, in absence of information related to the interaction cross-section in liquid xenon. A fit to all available LXe response parameters on NR and ERs over 40 years to date have been performed in order to combine them in an unified model.

NEST is a C++ code [85] and can be included as library in Gean4, replacing the existing physics process for scintillation photons (*G4 Scintillation*) by excitation and recombination. The advantage of NEST with respect to earlier simulations is to directly predict the absolute number of photons and electrons produced by an energy deposition. Thus, it bypasses the problem of non-linear energy dependence of the scintillation yield per unit energy deposited in the medium and also, of the influenced of scintillation yield by the magnitude of the applied electric field. Moreover, it takes into account the statistical smearing of each physics process, allowing for a complete description of the phenomenon.

The concept of NEST can be summarized as follows: the energy E_d deposited by a particle hitting a detector is firstly converted into

a number of quanta n_q, *i.e.* photons n_γ plus electrons n_e, by assuming a quanta yield q_y of 73 quanta/keV (fixed by the work function)

$$E_d = W \cdot n_q = W(n_\gamma + n_e)\,, \tag{4.1}$$

where $W = 1/q_y$ is the average work function (required energy) for creating a photon or electron; from this equation we clearly recognize the anti-correlation between the two signals. This process is dominated by a Fano factor F=0.03 [86]. Then, the quanta are shared between excitons N_{ex} and ions N_i, by taking into account the exciton-to-ion ratio α=N_{ex}/N_i as a field- and energy-dependent parameter, such that:

$$N_{ex} = \alpha N_i\,, \tag{4.2}$$

$$N_i = n_q - N_{ex}\,. \tag{4.3}$$

Part of N_i recombines itself (N_r) according to a field dependent recombination probability r:

$$N_r = N_i \cdot r\,. \tag{4.4}$$

This is the most crucial part of the simulation, and acts not only on the separation between the light yield for ER and NRs, but also on their smearing, affecting the discrimination power. In NEST (version 0.98), r is evaluated following the Doke-Birks model [87] for long tracks, which depends on the stopping power dE/dX of each particle, while for short length tracks (energies smaller than 10-15 keV) the Thomas-Imel box model [88], which depends on the energy, is adopted. Figure 4.1 shows

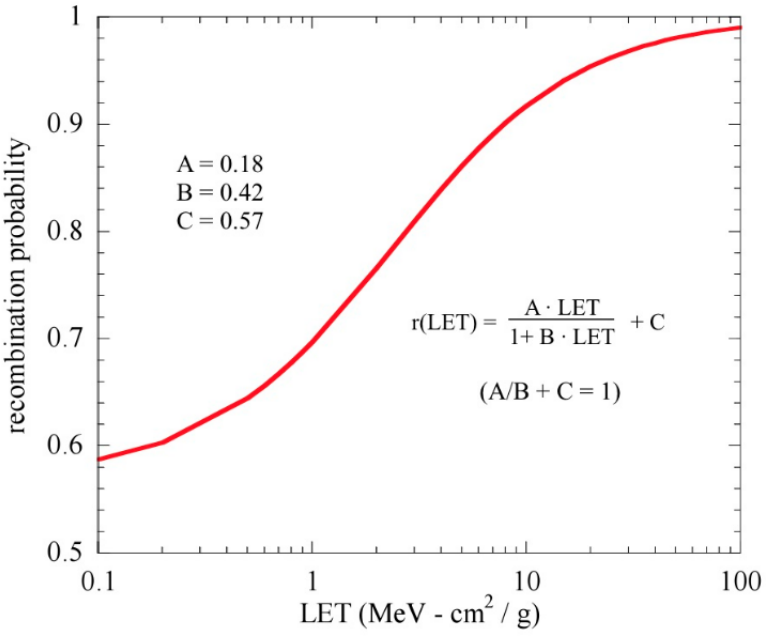

Figure 4.1: Doke-Birks recombination probability due to electrons in case of zero electric field.

the recombination probability, due to incoming electrons in case of zero

electric field, described by the Birks Law, which depends on the Linear Energy Transfer (LET), used instead of dE/dX. The free parameters A, B and C have been constrained by comparison with experimental data on light yield and the condition A/B+C=1 ensures that there is total recombination when dE/dX approaches infinity.

The average number of photons and electrons becomes:

$$n_\gamma = N_{ex} + N_r \,, \tag{4.5}$$

$$n_e = N_i - N_r \,. \tag{4.6}$$

In Figure 4.2 is shown a scheme of the physics process as described by NEST.

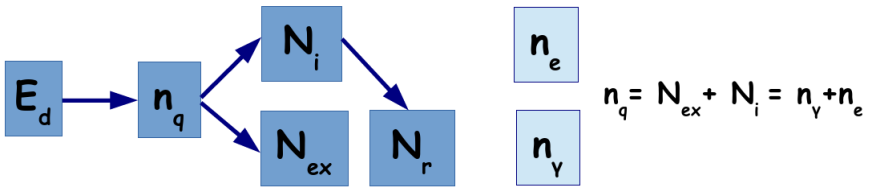

Figure 4.2: Scheme of the physics process related to the LXe response to an ionizing radiation as described by NEST.

The NEST (version 0.98) for ERs has been implemented in the XENON100 Geant4 code. In order to check if the photon and electron yield (n_γ/E_d and n_e/E_d respectively) before any detector effect is compatible with the average values released by the NEST collaboration [83, 89] to O(1%), we have run a full MC simulation. A flat spectrum of electrons with energies up to 200 keV have been generated in the center of the TPC, considering the electric field used in XENON100 during normal operations, 530 V/cm. The photon and electron yields obtained by the simulation (before being converted into S1 and S2 signals) are reported in Figure 4.3 left, while on the right are shown the relative benchmark plots from NEST. Comparing with the green curve in the NEST plot (500 V/cm drift field) the agreement on the mean value of the photon and electron yield is clear. The change of shape at around 10-15 keV is due to the different model used for the recombination probability, as explained above.

Once the full MC simulation has been validated, one can also build a toy MC following the NEST description and its statistical smearing. It can be summarized as (all the parameters have been explained above, in this Section):

1. Gaussian sampling of the number of quanta n_q

$$n_q \sim Gauss_{n_q}(q_y \cdot E_d, \sqrt{F} \cdot q_y \cdot E_d) \,; \tag{4.7}$$

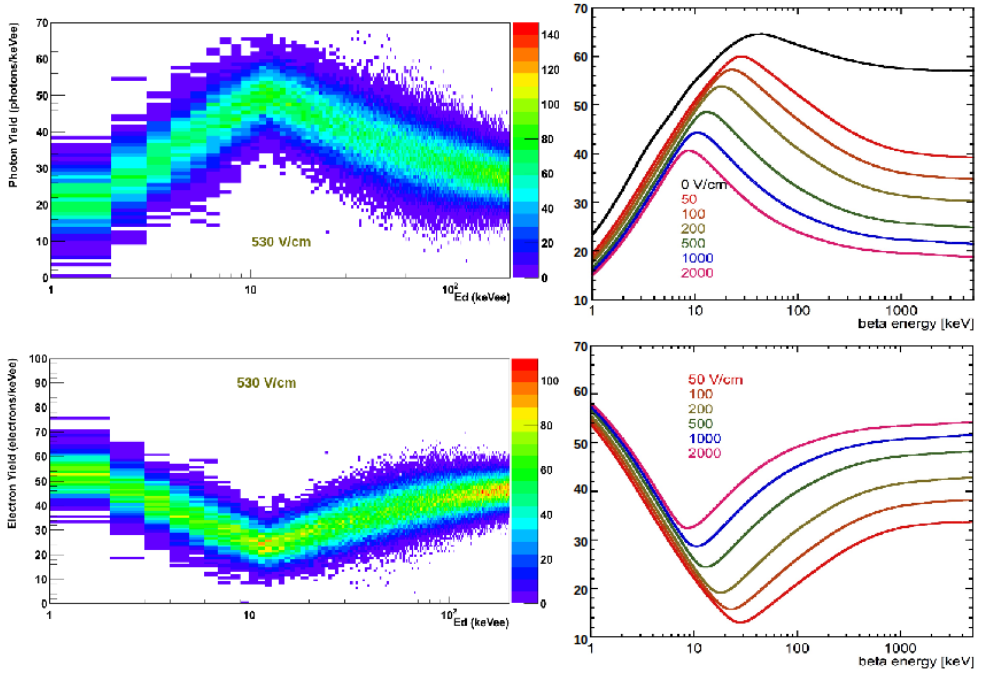

Figure 4.3: Photon and electron yield from a full MC simulation (left) compared with the benchmark plots from NEST (right).

2. Binomial sampling of number of excitons N_{ex} and anti-correlated number of ions N_i

$$N_{ex} \sim Binom_{N_{ex}}(n_q, \frac{\alpha}{\alpha+1}) \,, \tag{4.8}$$

$$N_i = n_q - N_{ex} \,; \tag{4.9}$$

3. Binomial sampling of number of recombined ions N_r

$$N_r \sim Binom_{N_r}(N_i, r) \,; \tag{4.10}$$

4. finally, the number of photons n_γ and electrons n_e obtained is the one in Equation 4.5 and 4.6 respectively.

The detector response parameters, such as exciton-to-ion ratio, Thomas-Imel parameter, recombination probability, *etc.*, have been reported on the NEST website [89], where also parameters related to the newer NEST version 0.99 for ERs have been calculated. NEST v0.99 mainly differs for the recombination treatment, that uses the Thomas-Imel box model in the entire energy range, and not only for short tracks, as in v0.98. For NEST v0.99 a Geant4 code has not been developed yet, then we can use it as toy MC only. Figure 4.4 shows the photon yield averaged in each keV bin of energy, obtained by a toy MC. Here a flat spectrum of ER events up to 100 keV has been simulated, using a drift field of 400 V/cm, in order to test both the NEST version 0.98 (blue line) and 0.99 (red line). The impact of the two different models for the recombination probability above 10-15 keV in energy is clear in the shape of photon yield.

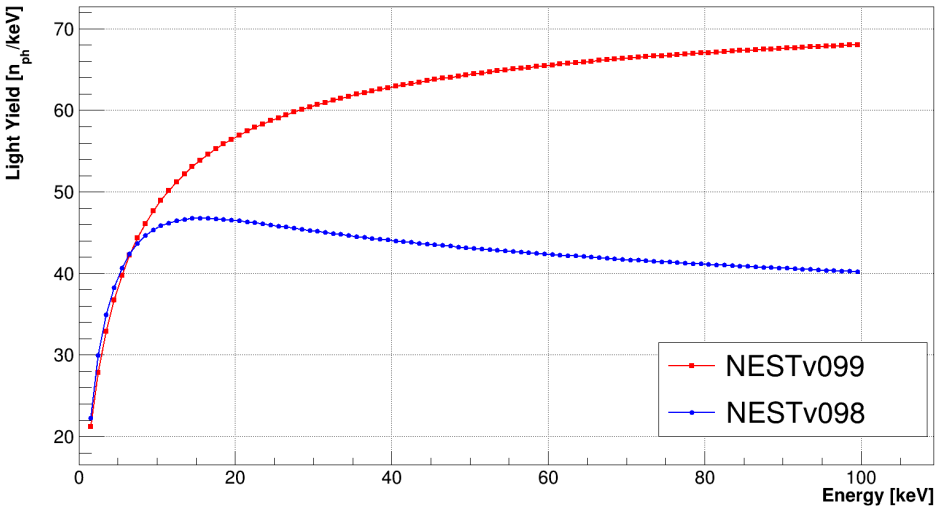

Figure 4.4: Photon yield averaged in each keV bin of energy obtained by a toy MC which follows the NEST model, version 0.98 (blue line) and 0.99 (red line).

4.1.2 Detector response

The second part of the simulation is made with an external code based on ROOT and is closely related to the detector parameters. In particular, it consists of converting the n_γ into the measurable signal S1 and n_e into S2, once they have been drifted toward the liquid-gas interface of xenon. In this procedure, the detector performances have been taken into account.

Going more into details, n_γ is firstly converted into number of photoelectrons N_{PE} created at the PMT surface, by applying the position-dependent Photon Detection Efficiency (PDE). The average PDE is given by the convolution of the Light Collection Efficiency (LCE), due to the detector geometry, and the PMTs Quantum Efficiency (QE):
PDE=LCE×QE.

Since the PDE is not homogeneous in the detector (see *Signal correction* in Section 3.1), it is usually corrected for a position-dependent correction factor $\alpha(r, z)$, shown in Figure 4.5. The correction map is calculated in XENON100 from the detector response to the gamma line at 39.6 keV coming from inelastic scattering of neutrons off ^{129}Xe nuclei. In particular, the light yield of each (r, z) cell has been normalized by the average light yield over the entire TPC volume, equal to 2.84 PE/keV. The average value of PDE is around 6% in XENON100, and is obtained experimentally from the ratio:

$$\langle PDE \rangle = \frac{L_y(E, 122\,keV)}{Ph_y(E, 122\,keV)}\,, \tag{4.11}$$

where $L_y(E, 122\,keV)$ is the S1-yield, defined as number of photoelec-

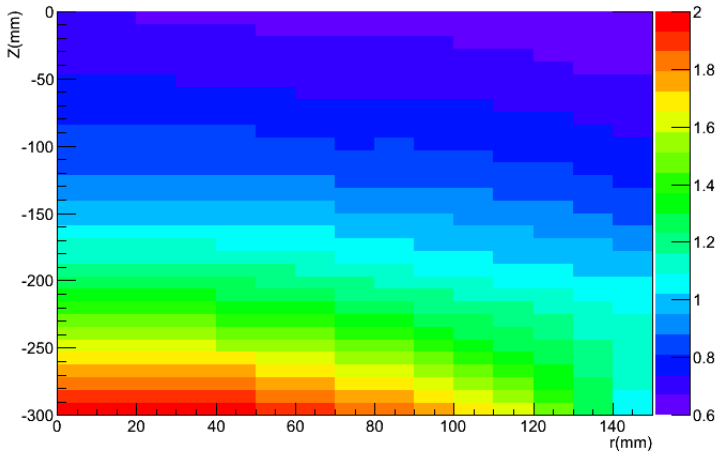

Figure 4.5: Position-dependent correction map $\alpha(r, z)$ to the Photon Detection Efficiency in XENON100.

trons per unit energy for 122 keV line, equal to 2.28 PE/keV and Ph_y $(E, 122\,keV)$ is the photon yield as reported in the NEST website, equal to 37.57 photons/keV. Both quantities are field-dependent and referred to a 500 V/cm drift field, while the PDE is field-independent. As we will see in the next Sections, in case one operates at a different electric field, the relative S1-yield can be obtained from the data as response to 122 keV gamma line. Then, in order to get the average PDE, the field-dependent photon yield can be retrieved from a fit over the photon yield of a 122 keV gamma line (reported in the NEST website), in case of different electric fields (*i.e.* 50, 100, 200 500, 1000, 2000 V/cm). In particular, the following fit function has been used:

$$Ph_y(E) = p0 + p1\,\log E + p2\,\sqrt{E} + p3\,E + p4\,E^2\,, \tag{4.12}$$

as shown in Figure 4.6.

The photon yield can also be parametrized by :

$$Ph_y(E) = Ph_{y,0} \cdot Quenching(E)\,, \tag{4.13}$$

where $Ph_{y,0}$ is the photon yield at zero field and $Quenching(E)$ is the light quenching due to the electric field.

In order to reproduce the PMT response properly, the fluctuations in single photoelectron pulses have been taken into account, such that the S1 signal is obtained by a Gaussian sampling with mean value equal to N_{PE} and width $\sigma_{PMT} \cdot \sqrt{N_{PE}}$, where σ_{PMT} is the single photoelectron peak/distribution. The average single photoelectron resolution of XENON100 PMTs is σ_{PMT}=0.5 PE, determined by PMT gain calibrations [59].

Finally, the resulting S1 signal is corrected for the average value of the LCE where the signal has been generated, in order to get the position

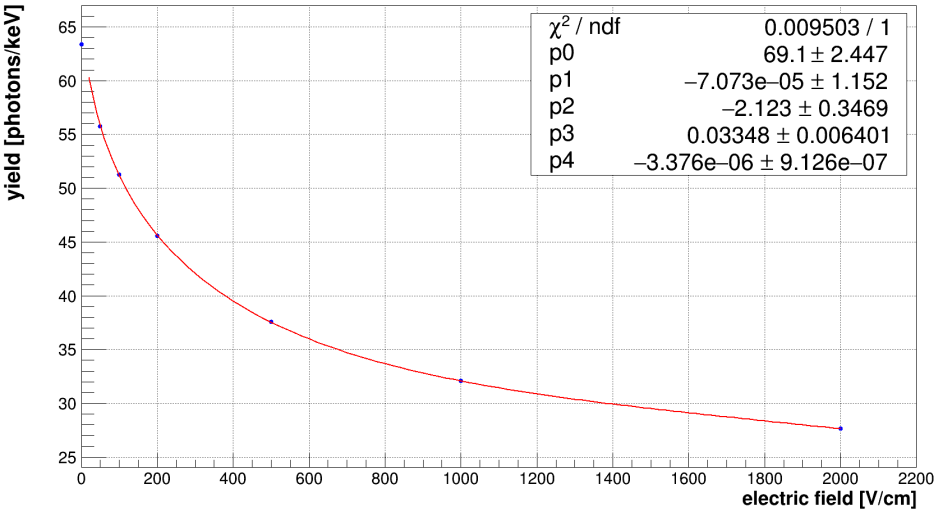

Figure 4.6: Fit to the photon yield obtained from a 122 keV gamma line, used as reference, at different values of the electric field (*i.e.* 50, 100, 200 500, 1000, 2000 V/cm), as reported in the NEST spreadsheet.

corrected S1 (cS1). The code that reproduces the light signal cS1 from the n_γ can be described with the following steps:

1. Binomial sampling of the number of photoelectrons N_{PE}

$$N_{PE} \sim Binom_{N_{PE}}(n_\gamma, \alpha(r,z) \cdot PDE)\,; \tag{4.14}$$

2. Gaussian sampling of S1 signal

$$S1 \sim Gauss_{S1}(N_{PE}, 0.5 \cdot \sqrt{N_{PE}})\,; \tag{4.15}$$

3. corrected S1 signal

$$cS1 = S1/\alpha(r,z)\,. \tag{4.16}$$

Now, in order to simulate the S2 signal, the electrons produced n_e have to be attenuated during their drift toward the liquid-gas interface, due to electronegative impurities in LXe (see Section 3.1). This effect depends on the position z of the interaction, calculated through the interaction time $t(z)$. The lifetime of the process, called *electron lifetime* τ_e, is around 500 μs in XENON100, obtained by calibration data and is weekly updated.

The extraction efficiency of electrons in the liquid-gas interface is considered 100%. The number of electrons extracted into the gas phase of xenon are called *gas events* N_g. In the gas surface, an amplification factor μ_1 called *secondary scintillation gain*, and its smearing σ_1 are applied in order to convert N_g to total photoelectrons N_{PE}. It takes into account the avalanche electrons produced by the strong electric field at

the xenon liquid-gas interface and their conversion into photoelectrons. The secondary scintillation gain, dependent on the anode voltage that generates the extraction field, are obtained from calibration data in XENON100 with a ^{60}Co source, by fitting the S2 low energy tail of the spectrum to see individually extracted electrons N_g. The fit function used is a sum of 5 Gaussians (multiplied by a function that accounts for the detection efficiency), assuming that the spectrum comprises a sum of one to five N_g. Figure 4.7 shows the fitted S2 low energy spectrum and the parameters of the first Gaussian, μ_1=19.67 PE/e$^-$ and σ_1=6.98 PE/e$^-$, are set as the mean and the with of the secondary scintillation gain [90].

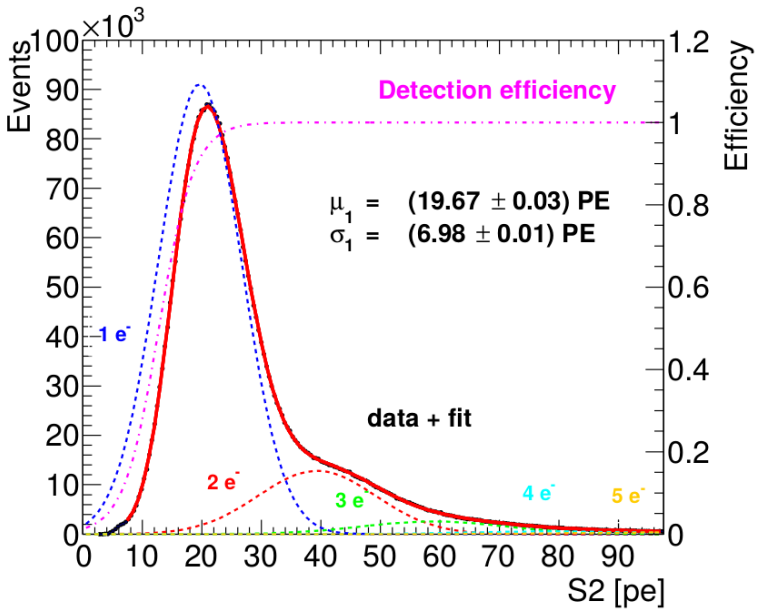

Figure 4.7: S2 low energy spectrum from a ^{60}Co source in XENON100, fitted with a sum of 5 Gaussians in order to get the secondary scintillation gain μ_1 and its width σ_1 [90].

While the signal S1 is very fast, since it is related to the light drift and reflection into the TPC, the signal S2 is slower, due to the time required by electrons for reaching the liquid-gas interface of xenon. As a consequence, in multiple hits the S1 resolution clusterize them into the same event, while the dilatation of the S2 signals allow to distinguish different peaks. The detector resolution on the S2 position along the z axis is 3 mm and has been taken into account into the simulation. In fact, all the hits happened in the LXe have been ordered by their z position: if inside 3 mm they are joined, the energy are summed, the S2s are summed and the positions are averaged, using the original S2 as weight; if outside, a new cluster has been computed.

Finally, the resulting S2 signals are corrected for the electron lifetime $e^{-t(z_{S2})/\tau_e}$ where they have been clustered, in order to get cS2. The code

that reproduces the charge signal cS2 from n_e can be basically described with the following steps:

1. Binomial sampling of the number of gas events N_g

$$N_g \sim Binom_{N_g}(n_e,\, e^{-t(z)/\tau_e})\,; \tag{4.17}$$

2. Gaussian sampling of S2 signal per each hit

$$S2 \sim Gauss_{S2}(\mu_1\, N_g,\, \sigma_1\sqrt{N_g})\,; \tag{4.18}$$

3. clusterization of S2 signals inside 3 mm along z axis: the energy of each hit is summed, the S2s are summed and the positions averaged, using the original S2 as weight;

4. corrected S2 signal

$$cS2 = S2/e^{-t(z_{S2})/\tau_e}\,. \tag{4.19}$$

4.2 AmBe calibration

^{241}AmBe calibrations have been performed before and after the long period of dark matter data taking, in order to check the detector stability and sensitivity to low energy NRs, also typical for WIMPs. In fact, the ^{241}AmBe is a (α,n) neutron source with a broad spectrum and an emission rate of (160±4) n/s [91]. We are interested in studying the ER background from inelastic scattering of neutrons off the xenon isotopes. In particular, a neutron scatters inelastically off a Xe nucleus, giving a scintillation photon (de-excitation); thus, we can observe a nuclear recoil together with an electronic recoil. In this study we analyze ERs of 39.6 keV gamma line from the isotope ^{129}Xe and the 80.3 keV gamma line from the isotope ^{131}Xe (a sketch of the process is shown in Figure 4.8).

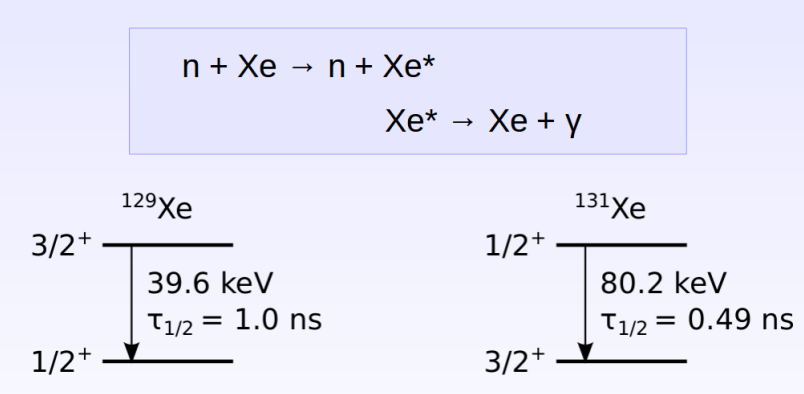

Figure 4.8: Sketch of the inelastic neutron scattering off ^{129}Xe and ^{131}Xe, with the consequent emission of a 39.6 keV and 80.3 keV gamma line.

The detector responds with S1 and S2 signals, anti-correlated and Gaussian distributed.

4.2.1 Elliptic fit

The detector response to a gamma line is a Gaussian distribution for both S1 and S2 signals. The resulting fit is a 2D Gaussian with different sigmas, *i.e.* an ellipsoid: when we cut the fit surface with a plane perpendicular to the z axis, we obtain an ellipse. Since the S1 and S2 signals are correlated, the ellipse is rotated; due to the anti-correlation of the signals, the rotation is counterclockwise. Figure 4.9 shows the initial ellipsoid function used to fit the signal due to a gamma line from AmBe calibration.

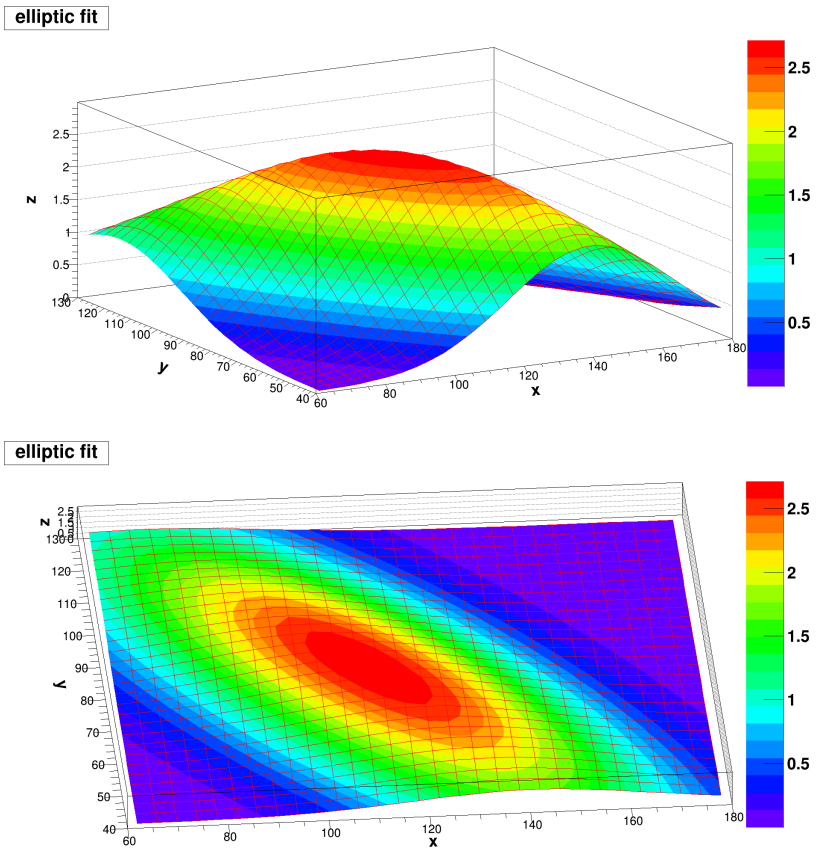

Figure 4.9: Ellipsoid used to fit the S1-S2 bubble due to a gamma line from AmBe calibration (top). In the bottom the elliptic planes for different values of z are more visible.

The equation used to draw this ellipsoid has 6 free parameters:

$$z = A \cdot \exp\{-(\frac{[(x-\mu_x)\cdot\cos\theta + (y-\mu_y)\cdot\sin\theta]^2}{a^2} + \frac{[-(x-\mu_x)\cdot\sin\theta + (y-\mu_y)\cdot\cos\theta]^2}{b^2} - 1)\}\,, \quad (4.20)$$

where:

- A= normalization constant,

- μ_x=S1 mean,
- μ_y=S2 mean,
- a=major axis,
- b=minor axis,
- θ=rotation angle (due to the S1-S2 anti-correlation).

We can quite well recognize the equation of a rotated ellipse inside the exponential term, while the physical meaning of this fit is the product of two Gaussians. If we consider two uncorrelated Gaussians corresponding to the S1 and S2 signals:

- S1 signal
$$G_{S1} = \frac{1}{\sigma_{S1} \cdot \sqrt{2\pi}} \exp\{-\frac{(x-\mu_{S1})^2}{2 \cdot \sigma_{S2}^2}\}, \tag{4.21}$$
- S2 signal
$$G_{S2} = \frac{1}{\sigma_{S2} \cdot \sqrt{2\pi}} \exp\{-\frac{(y-\mu_{S2})^2}{2 \cdot \sigma_{S2}^2}\}, \tag{4.22}$$

from the comparison with the Equation 4.20 we immediately get the mean and the sigma of the S1 and S2 signals, used in the following study:

- μ_{S1}=μ_x,
- μ_{S2}=μ_y,
- σ_{S1}=a/$\sqrt{2}$,
- σ_{S2}=b/$\sqrt{2}$.

2-sigma contour

Here we show how to select a 2-sigma contour from the ellipsoid. Firstly we have to remove the anti-correlation of S1 and S2, by rotating back the ellipsoid of a θ angle. The resulting ellipsoid will be:

$$z = A \cdot \exp\{-(\frac{(x'-\mu_x)^2}{a^2} - \frac{(y'-\mu_y)^2}{b^2} - 1)\} \tag{4.23}$$

Then we can center the ellipsoid to the origin of axes by moving it back of a value μ_x and μ_y:

$$z = A \cdot \exp\{-(\frac{x''^2}{a^2} + \frac{y''^2}{b^2} - 1)\} \tag{4.24}$$

Now we have to select the z-plane corresponding to 2-sigma ellipse (*i.e.* x''=$2\sigma_x$ and y''=$2\sigma_y$), recalling that a=$\sqrt{2}\sigma_x$ and b=$\sqrt{2}\sigma_y$:

$$z = A \cdot \exp\{-(\frac{(2\sigma_x)^2}{(\sqrt{2}\sigma_x)^2} + \frac{(2\sigma_y)^2}{(\sqrt{2}\sigma_y)^2} - 1)\} = A \cdot e^{-3} \tag{4.25}$$

Finally, the 2-sigma contour is obtained by imposing:

$$A \cdot \exp\{-(\frac{[(x-\mu_x)\cdot\cos\theta + (y-\mu_y)\cdot\sin\theta]^2}{a^2} + \frac{[-(x-\mu_x)\cdot\sin\theta + (y-\mu_y)\cdot\cos\theta]^2}{b^2} - 1)\} = A \cdot e^{-3}\,. \quad (4.26)$$

4.2.2 Results: MC-data comparison

In order to study properly the effect of the two gamma lines in the region of interests for WIMP search, we have selected in both MC and data the events with the following features (quality cuts):

- single scatters (based on the number of S2s),
- inside the inner fiducial volume of 40 kg,
- cS2>8000 PE, in order to remove the lower energy NR neutron scattering.

In case of the data, the basic cuts defined for the analysis have been firstly applied, in order to remove noisy events.

Figure 4.10 shows the elliptical fit to the 39.6 and 80.2 keV gamma lines in the S2 *vs.* S1 space in case of MC simulation and data; the black ellipses indicate the 1- and 2-sigma contours of the fit. A direct comparison between MC and data is reported in the Table 4.1, where the mean and sigma of the S1 and S2 signals are shown, together with the rotation angle and the rate of inelastic nuclear interactions. Moreover, for

39.6 keV	MC	Data	Discrepancy
μ_{S1} [PE]	113.91±0.11	117.66±0.09	-3%
σ_{S1} [PE]	24.05±0.10	19.81±0.07	21%
μ_{S2} [PE]	81.47±0.10	84.30±0.06	-3%
σ_{S2} [PE]	10.95±0.05	10.91±0.04	0.4%
θ [deg]	140.8±0.2	159.7±0.2	-12%
Rate [10^{-3}n/s]	116±5	116.2±1.6	0.3%
80.2 keV	MC	Data	Discrepancy
μ_{S1} [PE]	200.1±0.3	220.0±0.2	-9%
σ_{S1} [PE]	44.4±0.4	36.3±0.3	22%
μ_{S2} [PE]	196.7±0.3	189.6±0.2	4%
σ_{S2} [PE]	15.06±0.10	18.75±0.13	-20%
θ [deg]	134.9±0.2	142.4±0.4	-5%
Rate [10^{-3}n/s]	73±4	48.6±1.2	50%

Table 4.1: MC-data comparison of mean and sigma of S1 and S2 signals, rotation angle showing the anti-correlation and inelastic interaction rate from 39.6 keV and 80.2 keV gamma lines.

each parameter the discrepancy between MC and Data is calculated. The

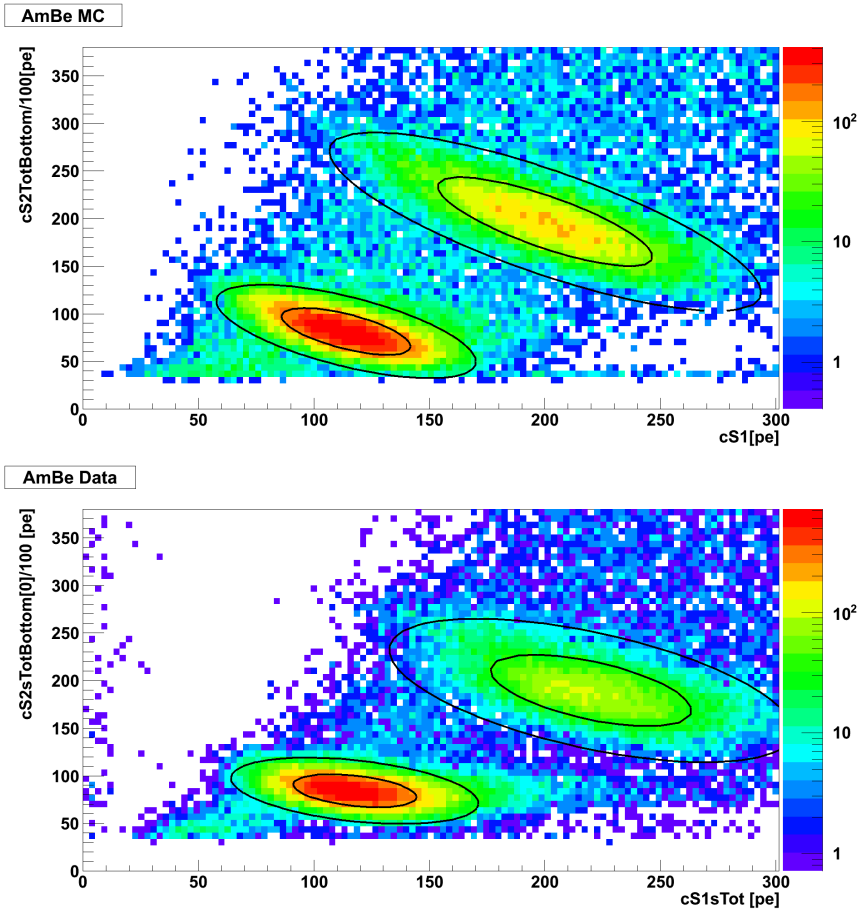

Figure 4.10: Elliptical fit on the gamma lines from Xe activation in case of MC simulation (top) and real data (bottom); the black ellipses indicate the 1- and 2-sigma contours of the fit.

interaction rate is defined as total number of events inside the 2-sigma contour, divided by the acquisition time T. In case of the data, T_{DATA} is given by the end and the beginning of a run, while in the MC case, T_{MC} is retrieved considering the activity A of the AmBe source and the total number of neutron generated, n_G: $T_{MC}=n_G/A$. The matching between MC-data is inside 10% for the S1, S2 mean values and for the rotation angle for the 80.2 keV gamma line. The rate of inelastic scattering events off ^{129}Xe matches the MC very well. On the other hand, the sigmas of S1 and S2 signals, the rotation angle for the 39.6 keV gamma line and the rate of inelastic scattering off ^{131}Xe show discrepancy greater than 20%. Regarding the rotation angle, in the MC case it remains almost constant in the two lines, and this agrees with the expectations in the absence of further interactions. Moreover, the higher values of the sigma of S1 and S2 signals in the MC could be an indication that the spread resulting from the simulation is too large; anyway, from a parallel analysis on ^{85m}Kr [92], the signal due to the de-excited 41.5 keV line has a rotation angle and sigmas of S1 and S2 signals very similar to those for the 39.4

keV gamma line from our MC.

Figure 4.11 shows the S1 and S2 distribution for both MC (blue line) and Data (red line); in order to make an effective comparison, the histograms have been normalized for the number of events and the same binning is used. In particular, the S1 and S2 distributions have been obtained as the projection on the x and y axes of Fig. 4.10 respectively. In Table 4.2 the S1 and S2 mean values and RMSs of each distribution,

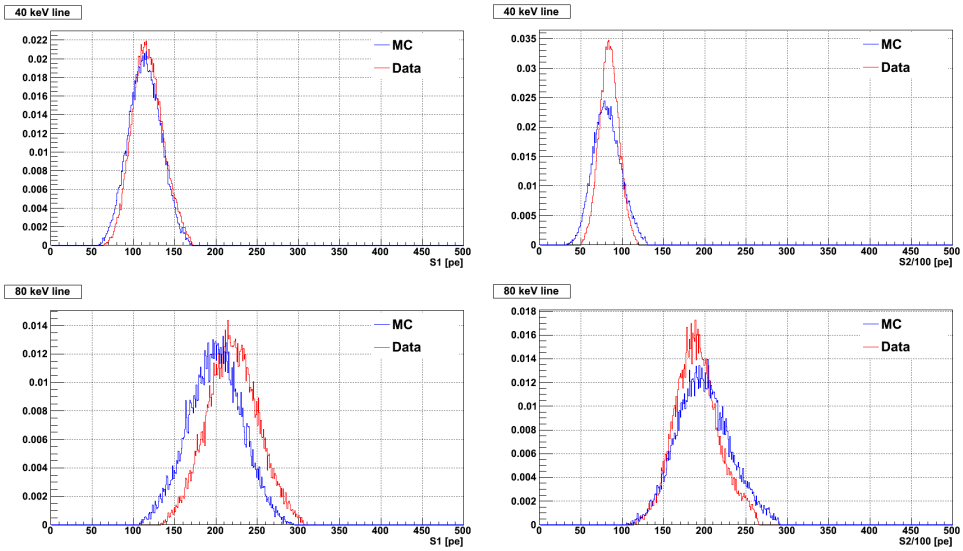

Figure 4.11: S1 and S2 distributions of the 39.6 keV and 80.2 keV gamma line for MC (blue line) and Data (red line).

together with the MC-Data discrepancy are reported. The matching between MC and data is within 10% for the S1 and S2 distributions of both lines, while the width of the S2 distribution in the MC case appears bigger than in the Data.

As a conclusion, we have ascertained that NEST, implemented in the XENON100 MC code, reproduces quite well the 39.6 keV and 80.2 keV

39.6 keV	MC	Data	Discrepancy
Mean S1 [PE]	113.77±0.10	117.56±0.08	-3%
RMS S1 [PE]	19.43±0.07	18.55±0.06	5%
Mean S2 [PE]	81.64±0.09	84.30±0.05	-3%
RMS S2 [PE]	16.75±0.06	11.69±0.04	43%
80.2 keV	MC	Data	Discrepancy
Mean S1 [PE]	199.0±0.2	220.0±0.2	-10%
RMS S1 [PE]	32.13±0.15	30.71±0.15	5%
Mean S2 [PE]	198.2±0.2	190.19±0.18	4%
RMS S2 [PE]	32.13±0.15	26.64±0.13	21%

Table 4.2: MC-data comparison of mean and RMS of S1 and S2 signals from 39.6 keV and 80.2 keV gamma lines.

Xe lines from AmBe. The main conclusions are as follows:

- we can trust our MC in predicting the average values of S1 and S2 signals;
- the MC sometimes differs from the data when considering the width of the S1 and S2 distributions;
- the S1-S2 rotation angle and sigma obtained with MC match a similar analysis on 41.5 keV line from ^{83m}Kr Data;
- the rate of inelastic interaction is in a very good agreement for the 39.6 keV line.

4.3 Th calibration

A ^{232}Th source was moved close to the cryostat of XENON100 and removed after few hours. This operation happened weekly in order to characterize the ER band (see Section 3.1.2). Low energy Compton electrons from Th source are uniformly distributed in energy, thus here we will consider the energy range of interest for WIMP search, between 0-50 keV.

4.3.1 Flattened ER band

In Section 3.1.2 we have already explained that the discrimination band is the main way to distinguish NRs, such those from WIMPs, by ERs, *i.e.* background, through the parameter $\log_{10}(S2_b/S1)$ as function of S1. Here we are interested in reproducing through MC simulation the band due to ERs, or ER band. Per each 1 PE bin of S1, a Gaussian fit over the discrimination parameter give us a set of mean values that can be fitted as a function of S1. The resulting fit function of the mean of the ER band, also called *ER mean*, will be used for this study. When we say *flattened ER band*, we refer to the discrimination parameter shifted by the ER mean, such that the discrimination band is centered along the ER mean (Figure 3.7).

4.3.2 Results: MC-data comparison

In order to study properly the effect of ERs in the low energy region, that represents a background for WIMP search, we have set the following quality cuts to both MC and data:

- single scatters,
- 34 kg fiducial volume,
- cS1<30 PE.

Moreover, in the MC we have used a selection that reflects the S2 hardware threshold for triggering an event, *i.e.* S2>150 PE. In the case of the data, some basic cuts remove noisy events.

The equation of the ER mean as a function of S1 is:

$$y = e^{p0+p1\cdot x} + p2 + p3\cdot x + p4\cdot x^2 + p5\cdot x^3 + p6\cdot x^4 + p7\cdot x^5 + p8\cdot x^6\ , \quad (4.27)$$

where x=cS1 and y=$\log_{10}$(S2$_b$/S1). Figure 4.12 shows the reconstruction of the ER band (red points) with both MC and data and the fit of the y mean values per each 1 PE bin in S1 is shown by the black line. In the bottom plot is reported the ER mean for MC (green line) and data (red line) for a more clear comparison. In the case of data, the population of events with high value of the discrimination parameter $\log_{10}$(S2$_b$/S1) represent a noise, when S1 and S2 do not belong together (not present in NRs) and can be removed with a dedicated cut. In Table 4.3 the fitting parameters of the ER mean and their MC-Data minimum difference have been listed. The matching between the fit on the ER

Param.	MC	Data	Diff. (%)
p0	-0.27±0.11	-0.06± 0.14	0
p1	(-29±2)·10^{-2}	(-4±3)·10^{-1}	0
p2	2.168±0.007	2.19±0.11	0
p3	(-5.2±0.3)·10^{-3}	(1.7±1.4)·10^{-2}	39
p4	(3.205±0.013)·10^{-3}	(-1.7±0.2)·10^{-3}	313
p5	(-5.950±0.005)·10^{-4}	(-2.2±0.6)·10^{-4}	112
p6	(3.7704±0.0017)·10^{-5}	(2.7±0.4)·10^{-5}	22
p7	(-1.0423±0.0006)·10^{-6}	(-9.7±1.1)·10^{-7}	0
p8	(1.0791±0.0017)·10^{-8}	(1.18±0.13)·10^{-8}	0

Table 4.3: Fitting parameters of the ER mean in MC and Data, obtained by ^{232}Th calibrations. The minimum difference has been calculated considering the closest MC and Data value inside errors.

mean band described by MC and Data is quite good. Actually, the fitting parameter p4 shows a 300% of difference, and also p3, p5 and p6 are slightly different. Anyway these discrepancies are highly affected by the errors on the fitting parameters.

Here we want to check if we can properly reproduce with MC the number of events below the ER/NR discrimination line, or *leakage events*, which would represent the most dangerous background. In particular, we proceeded as follows:

- use the flattened ER band, centered on the ER mean extracted from MC,
- use the official discrimination lines (defined in the flattened ER band) relative to 99.5%, 99.75% and 99.9% rejection,
- divide the x-axis of the MC flattened ER band in 1 PE slice of S1,

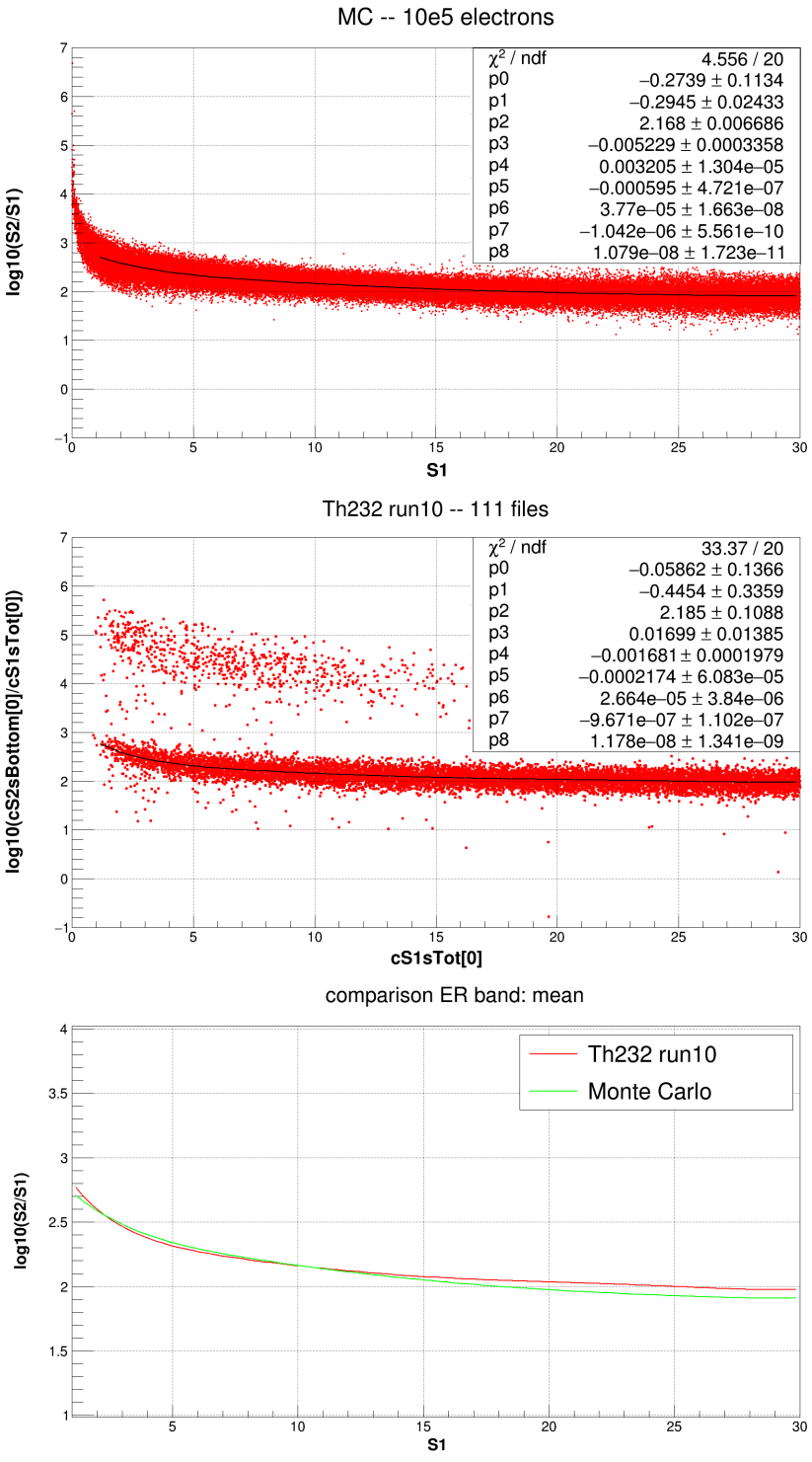

Figure 4.12: ER band reconstructed with both MC (top) and data (center) from ^{232}Th calibrations, represented by the red dots. The black line is the of the y mean values per each 1 PE bin in S1 On the bottom, the ER mean obtained with MC (green line) and data (red line).

- calculate the number events below the discrimination lines and normalize them for the total entries.

What we would expect with this procedure, in the best case, is that the leakage events predicted by MC would be 0.5%, 0.25% and 0.01%, referred to 99.5%, 99.75% and 99.9% discrimination lines respectively. In Figure 4.13 are shown the total MC counts below the three rejection lines per each 1 PE bin in S1. The mean value of the leakage events over the S1 range 0-30 PE is represented by the red line, while the expected number (0.5%, 0.25% and 0.01% respectively) is shown with a dashed line. The difference between leakage events predicted with MC and the

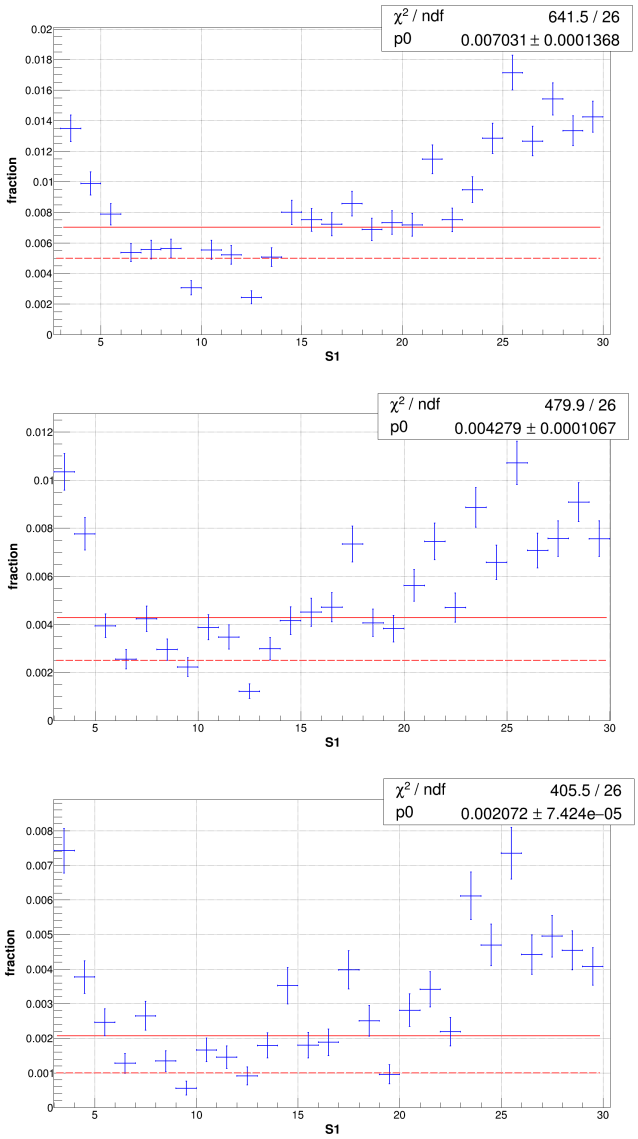

Figure 4.13: Fraction of leakage events predicted by MC, relative to 99.5% (top), 99.75% (center) and 99.9% (bottom) rejection lines per each 1 PE bin in S1. The red line is the average count, while the dashed line is the expected value, equal to 0.5%, 0.25% and 0.01% respectively.

expected one is quite big: around 27% for the 99.5% rejection line, 40% for the 99.75% rejection line and 50% for the 99.9% rejection line. The agreement between MC counts and expected values is better in the 5-15 PE range, while they disagree outide. Actually this behavior is coherent with the fact that there is not a perfect matching between MC and data regarding the fit of the ER mean (Figure 4.12 bottom).

As a conclusion, the NEST model manages to reproduce quite well the fit function to the mean value of the ER band per each S2 bin, but it still does not properly predict the fraction of leakage events. This effect agrees also with the analysis of the AmBe calibration, where the fluctuations of the detector response in the MC case are bigger than in the data, while the average values have been predicted quite well, inside 10%.

4.4 Tritium calibration

The tritiated methane (CH_3T), called tritium for simplicity, is an important source of internal calibration, thanks to the property of dissolving itself uniformly in the xenon volume. It is a beta emitter with an endpoint of 18.6 keV and a mean energy of 5.6 keV; the 64.2% of the decays happen in 1-8 keV energy range [93], of interests for WIMP search. The resulting interactions in the detector from electrons emitted by tritium are single scatter ER. The half-life of tritium is 12.33 years, but it can be removed with standard purification technology (only in case tritium is in a compound).

The tritium was injected in XENON100 during the last phase of its operation (in November 2015 and May 2016), in order to probe the performances of an internal source in view of XENON1T operations, for which external calibration sources are not sufficient to probe the inner part of the target. The cathode voltage used in this phase was 12 kV, generating a drift field of 400 V/cm, while the anode voltage was set to 4.4 kV. The field-dependent detector parameters have been adjusted accordingly in the MC, in particular:

- light *Quenching(E)*=0.6231, obtained from Figure 4.6,
- drift velocity v_d=1.74 mm/μs, proportional to the electric field (Equation 2.1)
- secondary scintillation gain of bottom PMT array μ_1=8.75 PE/e^-, σ_1=5.02 PE/e^-.

The quality cuts applied to both MC and data are:

- 48 kg fiducial volume,
- recoils happening just in the liquid-phase of the xenon volume.

Moreover, in the MC we have used a selection that reflects the S2 hardware threshold for triggering an event, *i.e.* S2>150 PE. We have not applied the single scatter cut in the MC, since the low endpoint of the energy spectrum already means that the events generated do not have enough energy to do multiple ERs. In the case of data, the usual basic cuts defined for the analysis in order to remove noisy events have been used. Moreover, also a single scatter cut that selects the events of interest has been applied.

4.4.1 ER band

As already mentioned, the width of the ER band is of great interest for a detector such as XENON, since it determines the discrimination efficiency of ER and NRs. It is affected by three components: the fluctuations on n_γ and n_e due to detector resolution and the event-to-event recombination fluctuations (σ(R), where R indicates the recombination). While the smearing due to n_γ and n_e can be measured somehow, the recombination fluctuations are more difficult to retrieve, and they are not taken into account in our MC model. This choice is motivated by the fact that the fluctuations in S1 and S2 obtained with a MC simulation are already bigger than in the Data case (Table 4.1 from AmBe calibrations), and a similar behavior is seen in the ER band, where the leakage events predicted with the MC results are higher than the expectations (Figure 4.13 from Th calibrations).

Figure 4.14 shows the ER band $\log_{10}(S2_b/S1)$ *vs* S1 obtained with both MC and Data. It has a characteristic decreasing shape as function of S1, reflecting the changing in light and charge yield at around 6 keV. Moreover, we have divided the ER band in 24 slices of 2 PE bin in S1, in the range 2-50 PE, performing a Gaussian fit for each distribution. The mean value extracted from the fit is superimposed to the ER band for both MC and Data and the relative sigma is reported in the bottom plot. The mean values for Data are higher than in MC case, above $\sim$18 PE of S1. More important, the fluctuations of the ER band decrease with S1 in the Data case, remaining anyway smaller than in MC (sigma is about 0.12 PE), as we can notice from the comparison of the values of sigma for the distributions. The bigger fluctuations in the ER band predicted with MC can explain the fact that leakage events with Th simulations are greater than the expectations.

Combined Energy Scale (CES)

As already mentioned in Section 3.1.1, the advantage of using both the S1 and S2 signals to reconstruct the energy of an event is the improvement in the resolution. This method is also called Combined Energy Scale (CES). Figure 4.15 top shows the CES obtained from MC (green line) and Data (red line), together with the true tritium energy spectrum [93] (blue line). On the bottom, we report the ratio of the Data to the MC,

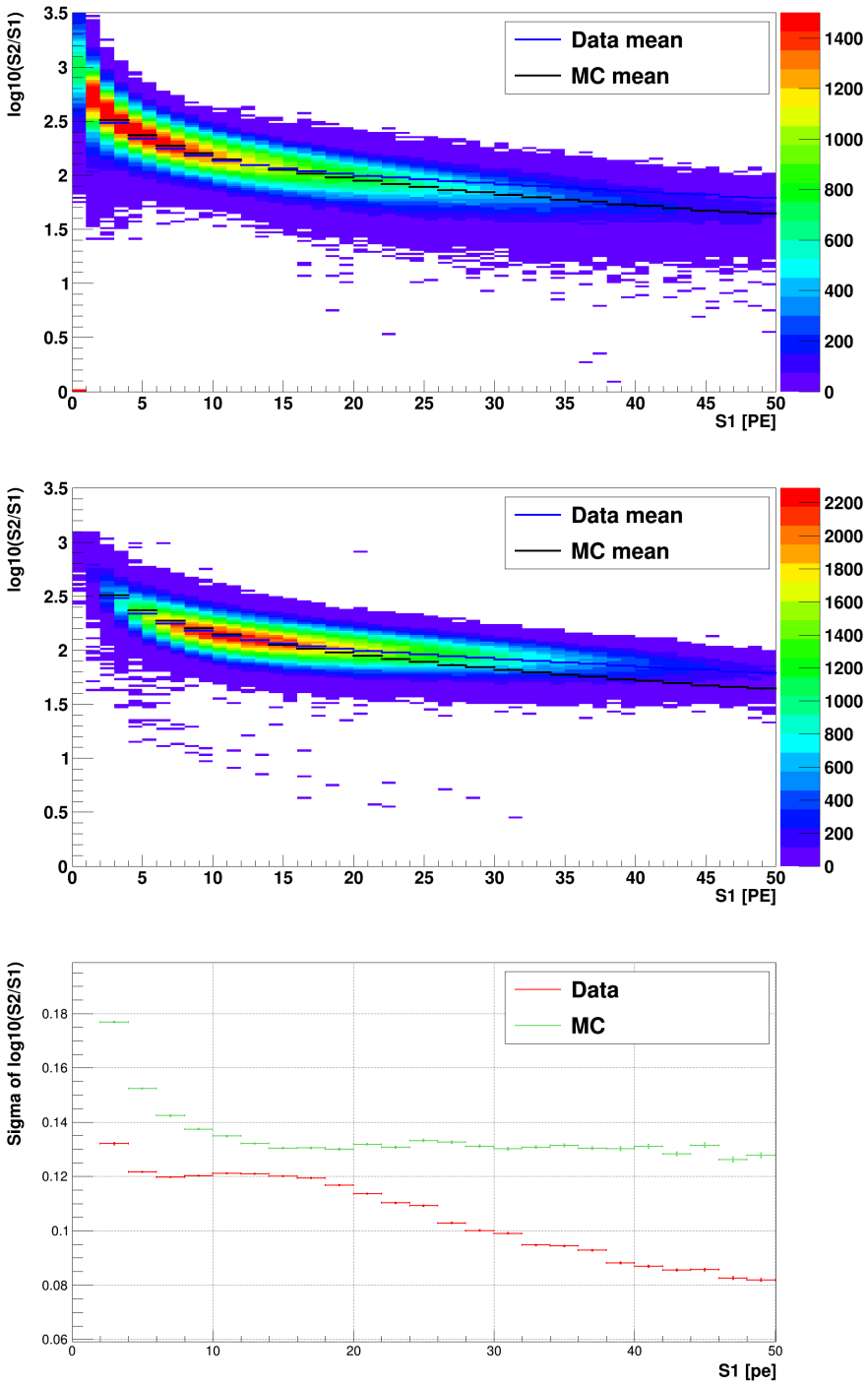

Figure 4.14: ER band reconstructed with both MC (top) and Data (center) from CH_3T calibrations. The mean of the Gaussian fit to the ER band per each 2 PE bin in S1, in MC (black line) and Data (blue line) case, is superimposed. MC (green line) and Data (red line) comparison of the sigma of the Gaussian fit to the ER band is shown in the bottom plot.

along with an empirical fit (red line) to an error function:

$$y = \frac{1}{2} Erf(\frac{x-\mu}{\sqrt{2}\sigma}) + \frac{1}{2}\,. \tag{4.28}$$

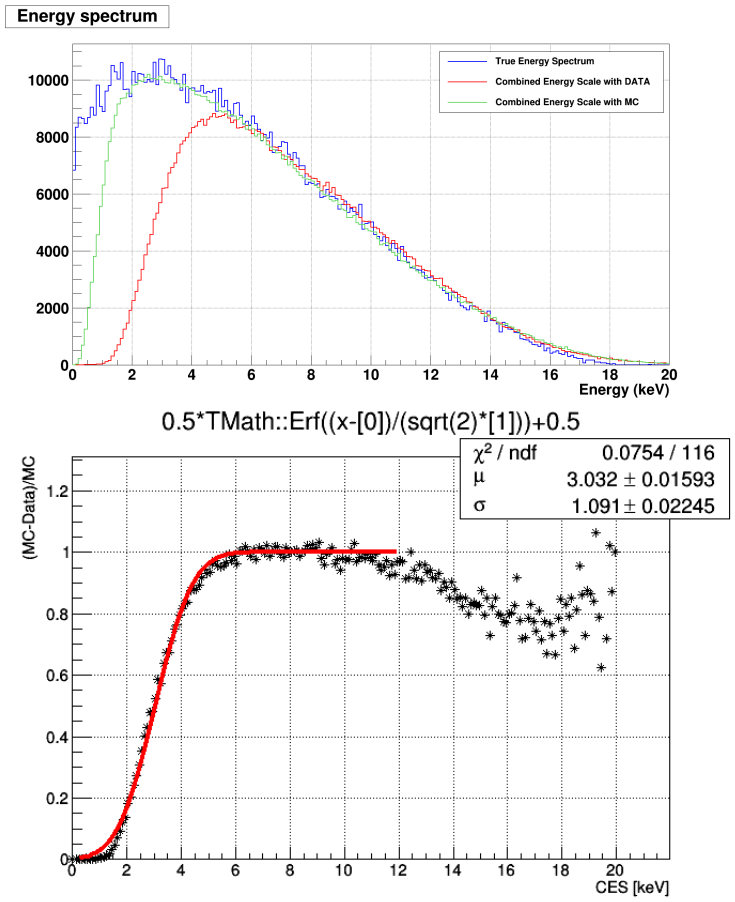

Figure 4.15: Top: tritium energy spectrum [93] and CES reconstructed with the MC (green line) and Data (red line). Bottom: ratio of the Data to the MC and fit with an error function (red line).

The agreement between MC and Data (and real energy spectrum) seems very good above 5 keV, supporting the validity of the S1 and S2 combined procedure to retrieve the energy. The lack of events below 5 keV in the Data is due to the basics and quality cuts applied, while below 2 keV we can notice the effect of the hardware threshold, very clear in the MC spectrum. However, starting from 2 keV in energy, the agreement between MC and true energy spectrum allows us to fully cover the very low energy region, never reached before with usual calibrations.

Moreover, one can directly obtain the total acceptance of the cuts applied from the ratio of the Data to the MC (where there are no cuts applied but the S2 trigger threshold); it is described by the error function used in the fit. The effective 50% energy threshold for ER events is

(3.032±0.016) keV. In the case of CES, the MC predictions describe very well the behavior of the detector.

4.4.2 Charge and Light yield

The light and charge yield are obtained dividing the S1 and S2 signals by the deposited energy, in form of CES. Figure 4.16 shows the light and charge yield map obtained with MC. Per each keV bin in energy the mean value has been computed in both MC and Data, and superimposed on the light and charge yield map. The mean values of the light and charge yield obtained by a toy MC (according to the NEST parameters reported in the website [89]) and Data is shown in a separate plot, where in the MC also the newer version of NEST, v0.99, has been tested. We have not used here a full Geant4 simulation, since a Geant4 code has not been developed for NEST v0.99. We want to remind that it mainly differs for the recombination treatment, that uses the Thomas-Imel box model in the entire energy range, while in the previous v0.98, for long tracks the Doke-Birk model has been used. In this plot, a small correction to account for threshold and spectral shape effects has been applied to the Data. In particular, spectral shape effects are caused by the fact that the CES, reconstructed with the detector parameters S1 and S2, reproduces the energy with a non-uniform fluctuation in each bin, due to the shape of the input spectrum. A correction function has been calculated as the ratio of yields given by MC input (directly from NEST) to those of MC output (obtained by the S1 and S2 signals.), for both charge and light. Above around 6 keV the agreement between MC with NEST v0.98 and Data results very good; on the contrary, the newer v0.99 does not match the Data.

Finally, a MC-Data comparison among the S1 and S2 signals is shown in Figure 4.17. As already concluded from a similar study with the AmBe calibrations, the MC shape of the S1 and S2 signals is not consistent with the data.

As a general conclusion, the results from MC predictions on the signal fluctuations in term of S1, S2 and ER band, suggest us to tune the MC model for electromagnetic background to calibration data in XENON100, as we will see in the next Chapter.

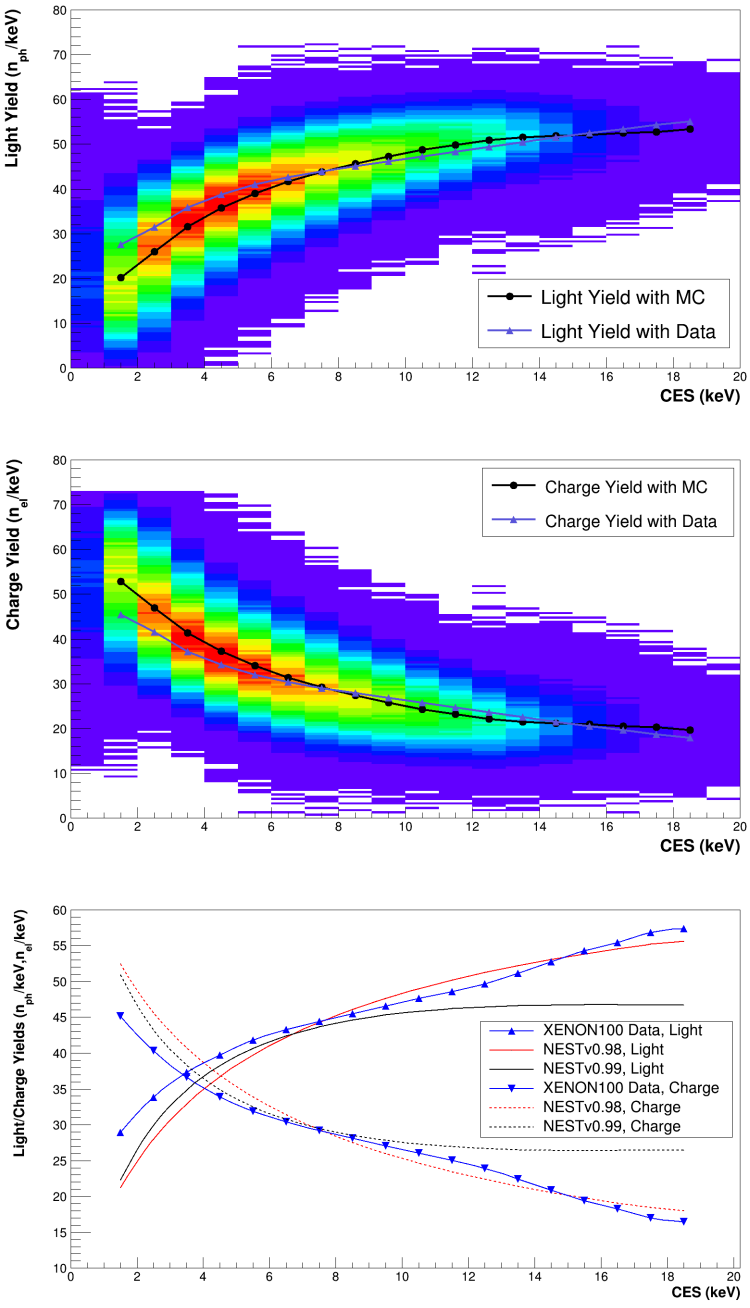

Figure 4.16: Light (top) and charge (middle) yield map obtained with MC, where the mean values extracted by MC (black line) and Data (purple line) are calculated per each 1 keV energy bin. Bottom: mean values of light and charge yield obtained with MC and Data (blue lines); a toy MC following NEST v0.98 (red lines) and v0.99 (red lines) have been developed.

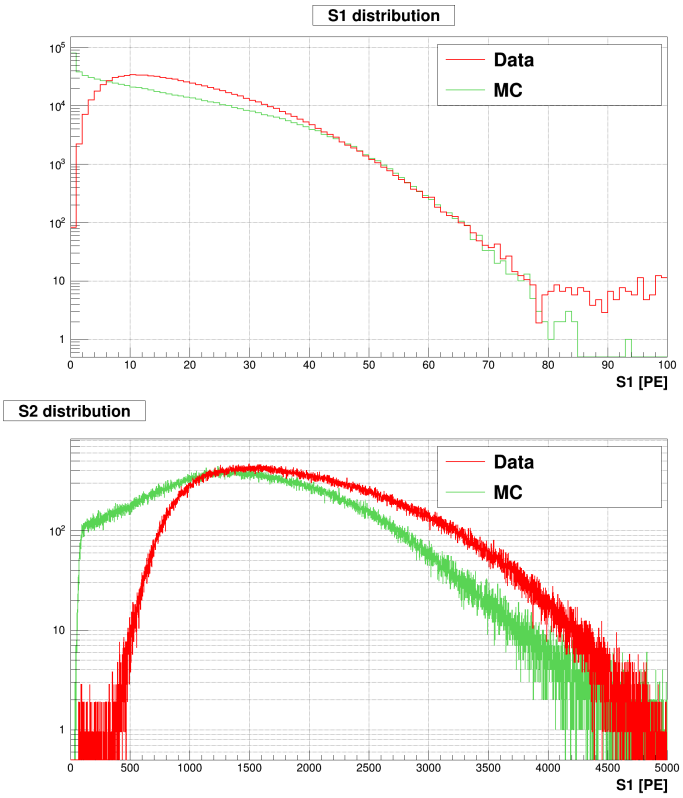

Figure 4.17: Comparison of the S1 (top) and S2 (bottom) spectrum from CH_3T calibrations between MC (green line) and Data (red line).

Chapter 5

Modelling the detector response to ERs with a Bayesian approach

In this Chapter we want to tune our MC model for ERs to calibration data in XENON100, in order to reconstruct the best photon yield map that matches the data.

An attempt of developing a refined matching between MC and measured data has been carried on within a Bayesian statistical approach. The idea is to build a phenomenological parameterization of the photon yield and its fluctuation, as function of the energy released in the detector by using the data from tritium calibration, a low energy beta emitter with endpoint 18.6 keV. The model used as input to predict the photon yield and its fluctuations is NEST. Then, the conversion between photons and electrons into measurable signal is closely related to the physics of the detector and is part of the likelihood.

5.1 Description

5.1.1 General mechanism

The NEST model (described in Section 4.1.1) gives values of photon yield $Ph_y(E)$, dependent by the energy E released by a particle hitting the target of the detector. The photon yield is defined as the number of photons n_γ per unit of energy. In the first step, we shall use a predefined photon yield map, as function of the energy, to generate a sample of ER events with a proper S1 and S2, to compare with the data from calibration runs in XENON100. Later we will try to reconstruct such map from the ER calibration data.

The model is developed in the 2D space defined by E and Ph_y (the photon yield for an energy E). In particular we define a 2D probability

density function (pdf), $p(E, Ph_y)$, which is normalized by definition as:

$$\int dE dPh_y p(E, Ph_y) = 1. \tag{5.1}$$

We can write it as:

$$p(E, Ph_y) = p(Ph_y|E)p(E)\,, \tag{5.2}$$

where the energy spectrum for ER is expected to be fairly flat, so $p(E) \approx$ const. At each fixed value of the energy E the conditional distribution $p(Ph_y|E)$ denotes the probability density for the possible values of Ph_y; large values of Ph_y decrease the ratio $S2/S1$.

We begin by describing the setup needed to reconstruct the NEST model output in the Ph_y *vs* E plane, which we call *ER photon yield map*. We divide the energy range in $i = 1, \ldots, N_E$ intervals, and for each we parameterize the conditional distribution of Ph_y, $p(Ph_y|E_i)$ with a Gaussian:

$$p(Ph_y|E_i) = \mathcal{N}_{Ph_y}(m_i, s_i)\,. \tag{5.3}$$

The parameters here are the mean m_i and the sigma s_i of the photon yield (although to simplify we could take at the beginning $s_i = s$ per each energy interval i). The vector of parameters for the 2D pdf is augmented by an amplitude parameter N_B, which controls the number of background events that are generated. Given that the observed number of calibration events is very large, the Poisson uncertainty on N_B can be neglected and we can also fix N_B to the number of background events observed in the calibration sample.

Thus, the parameters for this simple background model are

$$\Xi = \{m_1, \ldots, m_{N_E}, s_1, \ldots, s_{N_E}\}\,, \tag{5.4}$$

with a uniform prior in the range 0 to 1 for each m_i and s_i. The mean and sigma of the photon yield is set to be equal to the value predicted by NEST.

The determination of the background model proceeds as follows:

1. Draw Ξ from the prior. This generates the 2D pdf in the E, Ph_y space, or in the n_γ=Ph_y·E space, which we call $p(n_\gamma|\Xi)$.

2. Draw N_B ER model background events from $p(n_\gamma|\Xi)$, *i.e.* for $j = 1, \ldots, N_E$ do the following:

   (a) Compute the likelihood from:

   $$\mathcal{L}(\Xi_j) = p(S1, S2|\Xi_j) = p(S1|\Xi_j)p(S2|\Xi_j)\,, \tag{5.5}$$

   where

   $$p(S1|\Xi_j) = \sum_{n_\gamma} p(S1|n_\gamma)p(n_\gamma|\Xi_j)\,; \tag{5.6}$$

   $$p(S2|\Xi_j) = \sum_{n_e} p(S2|n_e)p(n_e|\Xi_j)\,. \tag{5.7}$$

(b) generate $S1, S2$ pseudo-data from $p(S1|\Xi_j)$ and $p(S2|\Xi_j)$, by using a simple rejection sampler.

3. Use a suitable Markov Chain Monte Carlo (MCMC) scheme, fed with the $S1, S2$ pseudo-data to converge to a posterior distribution for Ξ. In this work we use an affine invariant MCMC ensemble sampler, called *emcee* [94], which is open source and written in python.

Notice that in this framework, the posterior mean of Ξ gives the "best guess" of the background model, but we also have access to the variance through the samples themselves.

The posterior distribution for Ξ is equal to

$$p(\Xi|S1, S2) \propto \mathcal{L}(\Xi)p(\Xi)\,, \tag{5.8}$$

where $\mathcal{L}(\Xi) = p(S1|\Xi)p(S2|\Xi)$ is the likelihood and $p(\Xi)$ is the prior. The likelihood for the S1 and S2 signals will be explained in Sections 5.1.3 and 5.1.4 respectively, while the uniform prior is:

$$p(\Xi) = \begin{cases} 1/\Xi_{max} & \text{if } 0 \leq \Xi \leq \Xi_{max}; \\ 0 & \text{otherwise,} \end{cases} \tag{5.9}$$

where $\Xi_{max} = 73$ photons/keV, which corresponds to the quantum yield q_y (*i.e.* number of photons and electrons produced in unit of deposited energy) predicted by NEST.

5.1.2 Input parameters

As a starting point, we have to derive from NEST the average value of the photon yield m_j and its spread s_j for each 1 keV energy interval j, as described in the section above. We generated electrons with flat energies up to 50 keV, starting from the center of the TPC. The resulting photon yield map is shown in Figure 5.1 top: black markers represent the average m_j value of the photon yield, performed bin by bin with a Gaussian fit, and the corresponding sigma s_j, which stands around 6 photons/keVee, is reported in the bottom. As already described in Section 4.1.1, the change in the shape of the light yeld (parameters m_j and s_j) at around 12 keVee is justified by the different recombination model used in NEST (version 0.98), *i.e.* Thomas-Imel for short tracks and Doke-Birks for long ones. As input parameters for the likelihood we use the m_j and s_j extracted from the photon yield map.

Figure 5.2 shows the Gaussian fit of the photon yield performed in 4 bins, from 4 to 8 keV energy range, as example. From the plots, the distribution over each energy bin looks clearly Gaussian, as also evident from the fit parameters.

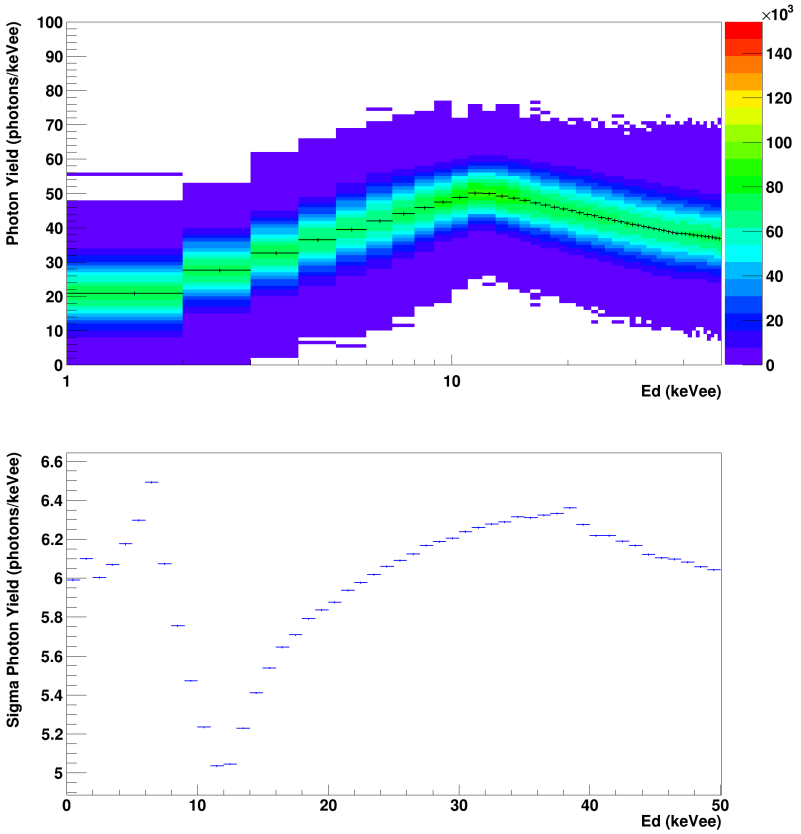

Figure 5.1: Photon yield map (top) extracted from NEST. The colour scheme shows the number of events, the mean values m_j per each 1 keV bin in energy are shown by black markers and the corresponding sigmas s_j obtained by a Gaussian fit are reported in the bottom plot.

5.1.3 Likelihood for S1 signal

The likelihood for the S1 signal

$$p(S1|\Xi) = \sum_{n_\gamma} p(S1|n_\gamma)p(n_\gamma|\Xi) \tag{5.10}$$

is composed of the product of a pdf $p(n_\gamma|\Xi)$ that is taken from the NEST model, and a pdf $p(S1|n_\gamma)$ related to the detector response.

The pdf for the number of gammas is obtained by the conditional distribution for Ph_y (Equation 5.3), remembering that n_γ=Ph$_y$×E:

$$p(n_\gamma|\Xi) = \mathcal{N}_{n_\gamma}(m \cdot E,\ s \cdot E)\,. \tag{5.11}$$

The pdf for the S1 signal follows the detector response, as described in Section 4.1.2: n_γ is firstly converted into number of photoelectrons N_{PE} created at the PMT surface, considering the spatially-averaged Photon Detection Efficiency, then we apply to each single PE a convolution with a Gaussian distribution to reproduce the response of the PMT

$$p(S1|n_\gamma) = \sum_{N_{PE}} p(S1|N_{PE})p(N_{PE}|n_\gamma)\,, \tag{5.12}$$

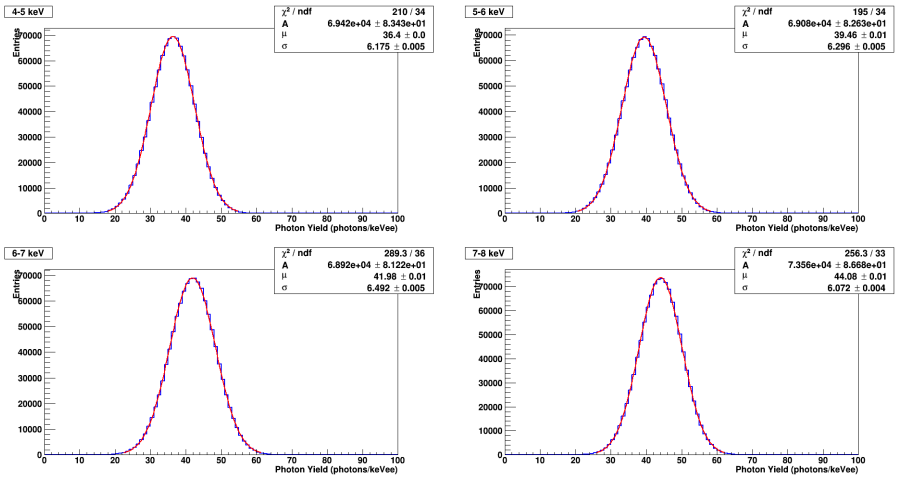

Figure 5.2: Gaussian fit to the photon yield in 4 bins of energy.

where

$$p(N_{PE}|n_\gamma) = Binom_{N_{PE}}(n_\gamma, PDE)\,, \tag{5.13}$$

$$p(S1|N_{PE}) = \mathcal{N}_{S1}(N_{PE}, 0.5\sqrt{N_{PE}})\,. \tag{5.14}$$

The value of PDE is 0.0607 PE/gammas, while the 0.5 width of the Gaussian distribution is the average single PE resolution of the PMTs, as in the XENON100 detector [59].

Thus, the final likelihood for the S1 signal is expressed as:

$$p(S1|\Xi) = \sum_{N_{PE}} \mathcal{N}_{S1}(N_{PE}, 0.5\sqrt{N_{PE}})\cdot \\ \cdot \sum_{n_\gamma > N_{PE}} Binom_{N_{PE}}(n_\gamma, PDE)\mathcal{N}_{n_\gamma}(m\cdot E,\ s\cdot E)\,. \tag{5.15}$$

5.1.4 Likelihood for S2 signal

The likelihood for the S2 signal

$$p(S2|\Xi) = \sum_{n_e} p(S2|n_e)p(n_e|\Xi) \tag{5.16}$$

is composed, as the S1 likelihood, of the product of a pdf $p(n_e|\Xi)$ for the number of electrons anti-correlated to n_γ as described by the NEST model, and a pdf $p(S2|n_e)$ related to the detector response.

The pdf for the number of electrons is a Gaussian anti-correlated to the conditional distribution for Ph_y, with a mean value depending on the quanta yield q_y= 73 quanta/keV:

$$p(n_e|\Xi) = \mathcal{N}_{n_e}((q_y - m)\cdot E,\ \sqrt{(F\cdot q_y)^2 + s^2}\cdot E)\,, \tag{5.17}$$

where the variance includes also the Fano factor F=0.03 [86] for generating n_q.

The pdf for the S2 signal considers firstly the gas events N_g, due to electrons drifting towards the anode for a time t_d and reaching the liquid-gas interface, taking into account the attenuation due to electronegative impurities, characterized by an electron lifetime τ_e. Then, the S2 signal is generated assuming a full extraction efficiency, a mean amplification factor μ_1 (secondary scintillation gain) and a Gaussian smearing σ_1:

$$p(S2|n_e) = \sum_{N_g} p(S2|N_g)p(N_g|n_e)\,, \tag{5.18}$$

where

$$p(N_g|n_e) = Binom_{N_g}(n_e, e^{-t_d/\tau_e})\,, \tag{5.19}$$

$$p(S2|N_g) = \mathcal{N}_{S2}(\mu_1 N_g, \sigma_1\sqrt{N_g})\,. \tag{5.20}$$

The value used for the electron lifetime is τ_e=500 μs and for secondary scintillation gain is μ_1=19.7 PE/e$^-$ and σ_1=7 PE/e$^-$, as in the ordinary operations of the XENON100 detector [90].

Thus, the final likelihood for the S2 signal is expressed as:

$$p(S2|\Xi) = \sum_{N_g} \mathcal{N}_{S2}(\mu_1 N_g, \sigma_1\sqrt{N_g}) \sum_{n_e>N_g} Binom_{N_g}(n_e, e^{-t_d/\tau_e})\cdot \\ \cdot \mathcal{N}_{n_e}((q_y - m)\cdot E,\ \sqrt{(F\cdot q_y)^2 + s^2}\cdot E). \tag{5.21}$$

5.2 Validation

Now we want to test the likelihood of a mono-chromatic gamma source with recoil energy E=39.6 keV (such as the one due to de-excitation of the isotope ^{129}Xe); the corresponding mean of the array of parameters Ξ, given by NEST, is m_{40}=38.31 photons/keVee. For simplicity, we start by fixing the value of the parameter sigma to s_{40}=6 photons/keVee, such that our ER model depends by the mean photon yield only. Figure 5.3 shows $p(S1|\Xi)$ as a sampling distribution in the top left panel, and as a likelihood function in the top right panel. In particular, the $S1$ signals have been randomly sampled from the first distribution: for this reason, by repeating 5 times the process with the same energy, *i.e.* same photon yield, the sampling distributions look the same. On the other hand, the likelihood functions looks different, since they are calculated as the probability to have a light yield such that it gives us the different sampled S1s. In the bottom panels are reported the similar plots for $p(S2|\Xi)$.

5.2.1 Data generation

Here we check the auto-consistency of the likelihoods that describes the ER background model in the Bayesian framework, by comparing with NEST.

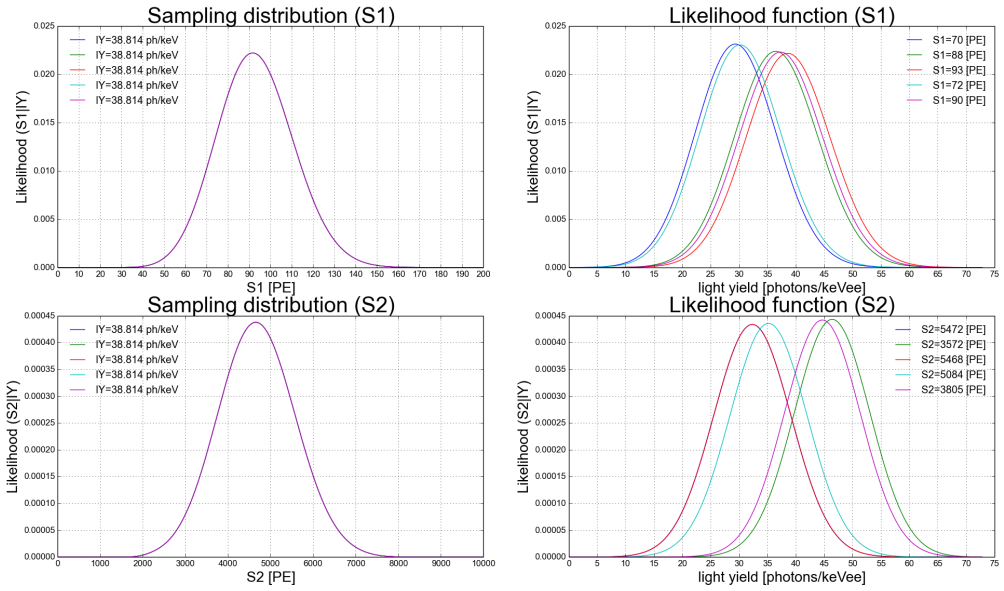

Figure 5.3: Top: sampling distribution (left) and likelihood function (right) of $p(S1|\Xi)$. Bottom: similar plots for $p(S2|E)$.

We consider 1000 events of a 39.6 keV gamma line, generated in the bottom part of the TPC. The S2 *vs.* S1 detector response obtained by a toy MC, following NEST v0.98 (according to the parameters reported

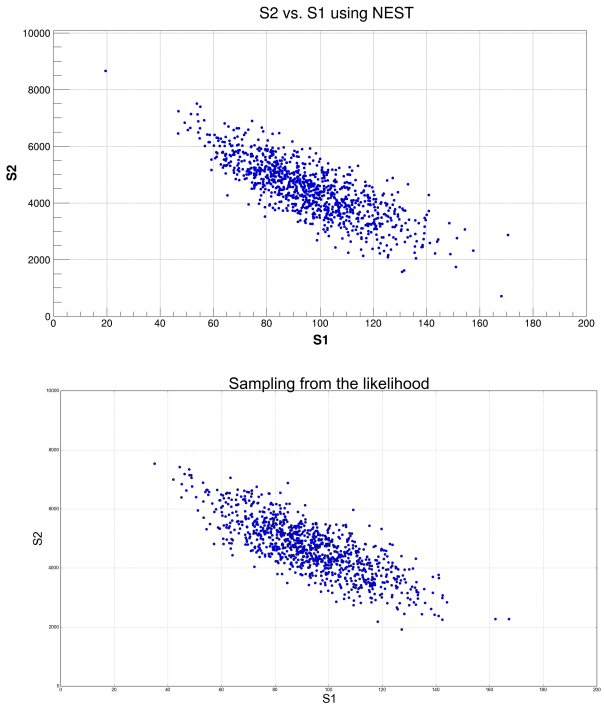

Figure 5.4: S2 *vs.* S1 distribution of 1000 events from a 39.6 keV gamma line obtained by NEST (top) and sampled by $p(S1, S2|\Xi)$ (bottom).

in the website [89]), and by sampling from the left panels of Fig. 5.3, is shown in Figure 5.4. The S1-S2 anticorrelation is clearly visible. Moreover, the center of the 39.6 keV region and its spread are very similar for NEST and the likelihood.

The comparison of the ER band, $\log_{10}(\mathrm{S2}_b/\mathrm{S1})$ *vs.* S1, obtained by 5000 events with uniform energy in the range 2-20 keV, as generated by NEST and sampled from the likelihood, is shown in Figure 5.5. Again, the detector response using the likelihood to reproduce the S1 and S2 signals for the ER band is consistent with the NEST model and we can go on with the event reconstruction.

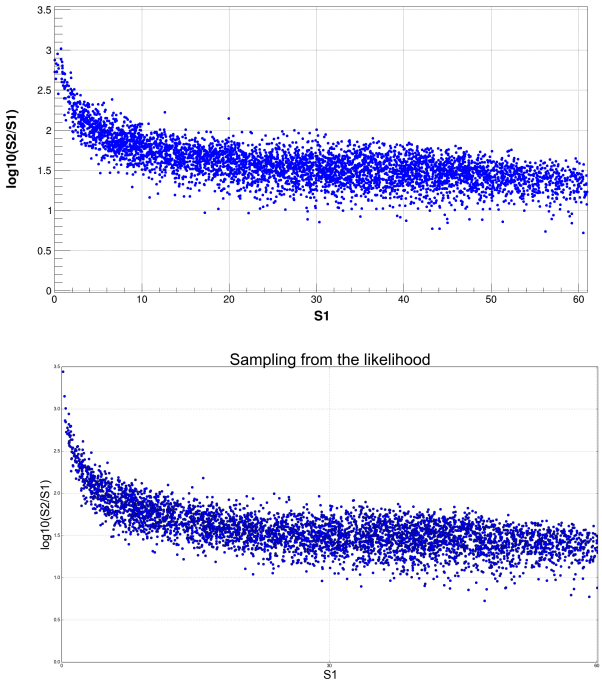

Figure 5.5: ER band from 5000 events with uniform energy in the range [2,20] keV, obtained by NEST (top) and sampled by $p(S1, S2|\Xi)$ (bottom).

5.2.2 1D single event reconstruction

Here we show how we converged to a posterior distribution of the parameters Ξ using an MCMC method.

We start by reconstructing a single point of the photon yield map referred to one energy bin. For simplicity, we still keep the value of the parameter sigma fixed, such that we use only one parameter, m_j; for this reason we are performing a 1D single event reconstruction. The procedure to obtain the posterior $p(m_j|S1, S1)$ is the following:

1. consider for instance 10 interactions due to a mono-energetic gamma source of 39.6 keV: the corresponding photon yield mean obtained

by NEST is m_{40}=38.31 photons/keVee (free parameter) and the sigma is fixed to s=6 photons/keVee,

2. generate 10 $\{S1, S2\}$ pseudo-data from $p(S1|\Xi)$ and $p(S2|\Xi)$, by using the rejection method,

3. reconstruct the photon yield $p(\Xi_{40}|S1, S2)$ from the 10 $\{S1, S2\}$ pseudo-data by using *emcee* and a uniform prior $p(\Xi)$.

Figure 5.6 shows the posterior distribution of the mean photon yield (*emcee* required 20 steps and 100 walkers). The pdfs obtained from the

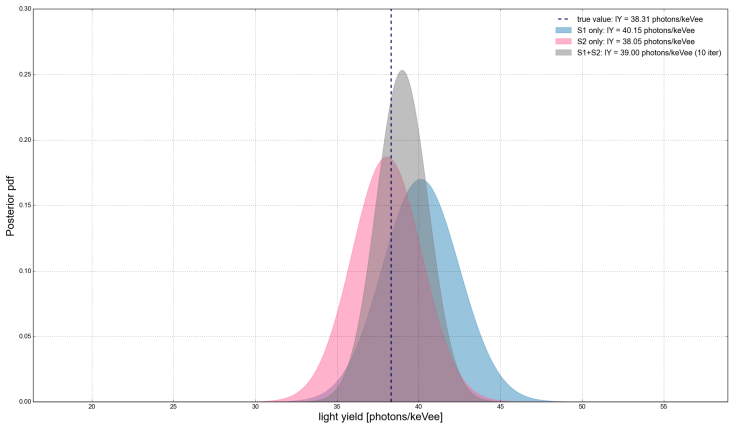

Figure 5.6: Resulting 1D posterior distribution of the mean photon yield, feeding the MCMC with 10 couples of pseudo-data $\{S1, S2\}$ sampled by the likelihood, for a 39.6 keV gamma line. The blue pdf $p(\Xi|S1)$ is obtained using the S1 signal only, the pink pdf $p(\Xi|S2)$ using S2 only, while the gray pdf $p(\Xi|S1, S2)$ uses both the signals S1 and S2. The vertical dashed line represents the true value.

S1 and S2 signals separately have a larger smearing than the one obtained using both S1 and S2, as expected. Anyway, all the three distributions stand around the true value (dashed line), which means the procedure to obtained the posterior is working well.

5.2.3 2D single event reconstruction

Now we consider also the sigma of the photon yield as a free parameter s_j, such that we can perform a 2D event reconstruction. The procedure to obtain the posterior $p(m_j, s_j|S1, S2)$ is the same as in the 1D case, but here we are using

- number of events: 20,

- 20 steps and 100 walkers,

- energy of events: 40 keV,

- true photon yield m=38.27 photons/keV and s=6.21 photons/keV (from NEST).

Figure 5.7 shows the posterior distribution of the mean and sigma of the photon yield, obtained using the S1 signal only $p(\Xi|S1)$, the S2 only $p(\Xi|S2)$ and both S1 and S2 $p(\Xi|S1, S2)$. Figure 5.8 reports the corner

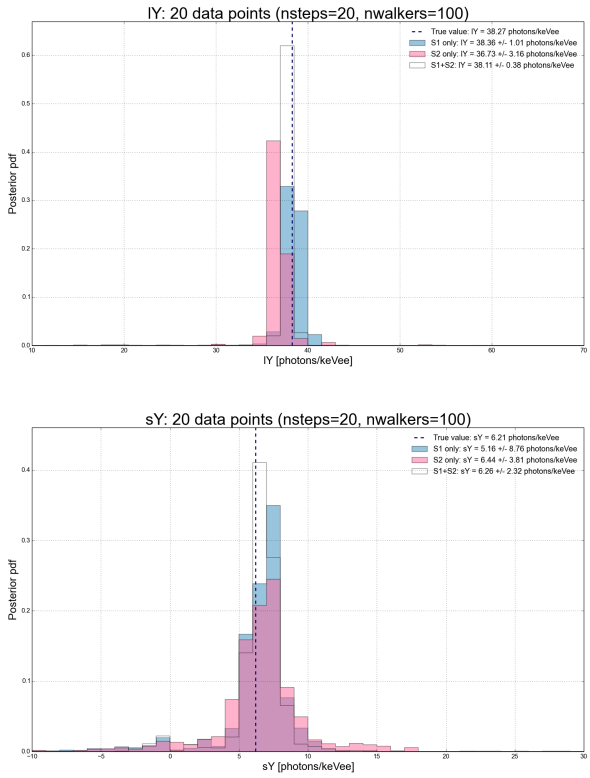

Figure 5.7: Resulting 2D posterior distribution of the mean (top) and sigma (bottom) of the photon yield, feeding the MCMC with 20 pairs of pseudo-data $\{S1, S2\}$ sampled by the likelihood, relative to a 40 keV mono-energetic line. The blue pdf $p(\Xi|S1)$ is obtained using the S1 signal only, the pink pdf $p(\Xi|S2)$ using S2 only, while the white pdf $p(\Xi|S1, S2)$ uses both the signals S1 and S2. The vertical dashed line represents the true value.

plots (*i.e.* posterior distributions of free parameters and their correlation) of the 2D event reconstruction, directly generated by the implemented MCMC method.

In the 2D event reconstruction, the pdfs obtained using the S1 $p(\Xi|S1)$ and S2 $p(\Xi|S2)$ separately have a larger smearing then the one obtained using both S1 and S2 $p(\Xi|S1, S2)$, as expected.

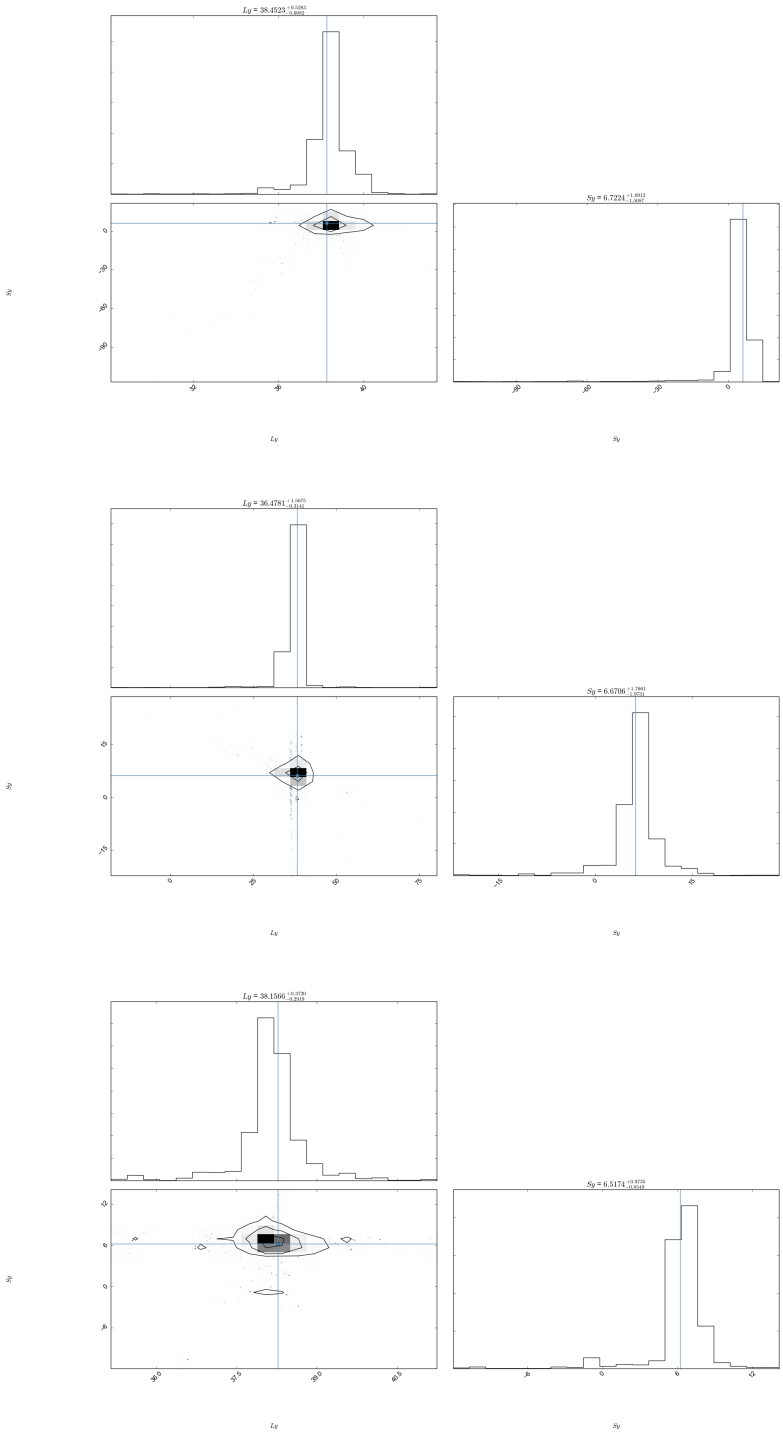

Figure 5.8: Corner plot of the 2D event reconstruction, using S1 (top), S2 (center) and both S1 and S2 (bottom), in order to show any eventual correlation between parameters.

5.2.4 Photon yield map

Here we reconstruct the 2D map of the photon yield, between 0-50 keV energy and with 1 keV bin width. The maximum of the posterior of the photon yield and the sigma have been used to draw a Gaussian distribution. We have used 5 events per each energy bin and the MCMC has been set with 20 walkers and 50 steps. In Figure 5.9 the reconstruction of the photon yield map is done by using the S1 signal only, S2 only and both S1 and S2. Black horizontal lines correspond to the mean of the photon yield and the blue line is the true photon yield (from NEST), as reference. The mean values of the photon yield obtained with S1 only, S2 only, both S1 and S2 and the true photon yield are shown all together in Figure 5.10, and the same has been done for the width of the photon yield.

The reconstructed mean values of the photon yield appear in good agreement with the ones given by NEST, especially in the case of using both the S1 and S2 signals. On the other hand, the number of events per energy bin, walkers and steps looks not enough to reproduce precisely the posterior distribution of the sigma of the photon yield; by rising those parameters the computational time will rise accordingly. Anyway, the ER background model developed has been tested with satisfying results.

Finally, we want to test the goodness of the Combined Energy Scale (Section 3.1.1) obtained with a pair of $\{S1, S2\}$ sampled from the likelihood. Since we are deciding *a priori* which energy E_d is released in the detector, we can directly compare it with the CES. In order to verify if the CES is a really good estimate for the energy, we have extracted from the likelihood 5 pair of $\{S1, S2\}$ per each energy bin of 1 keV in the range 0-50 keV. A fit over the CES *vs.* E_d distribution gives us the following equation:

$$CES = m \cdot E_d + q\,, \tag{5.22}$$

where $m \approx 1$ and $q \approx 0$ within the errors of the fit (Figure 5.11), that perfectly agrees with the expectations.

5.3 Photon yield map from tritium data

A more refined data-simulation fitting model, also based on MCMC, has been developed in parallel to extract the photon yield from the beta decays of tritium, below 15 keV [95]. The method used to evaluate the posterior probability is exactly the same as described in this Chapter, and the likelihoods for the S1 and S2 signals are basically the ones reported above. In fact, the likelihoods consider the xenon response to ERs as modelled by NEST to obtain n_γ and n_e, and the detector response to retrieve S1 and S2.

The power of this work is to describe more in detail the detector physics and response. In particular, with respect to the current ER model, it adds:

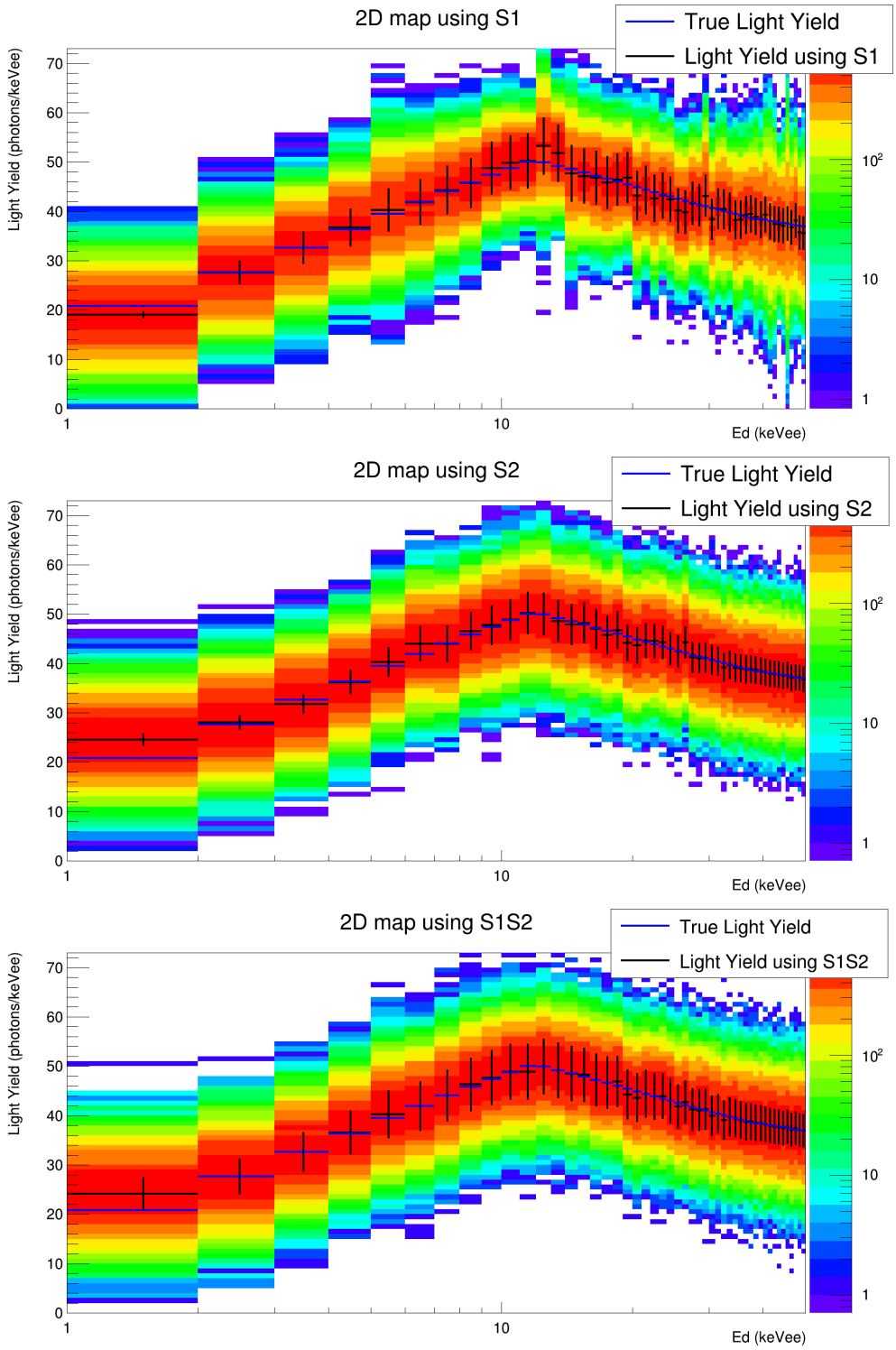

Figure 5.9: Photon yield map reconstructed with MCMC (the colour scheme indicates the posterior distribution using 5 events per bin, 20 walkers and 50 steps), using the S1 signal only (top), S2 only (middle) and both S1 and S2 (bottom). Black horizontal lines correspond to the mean of the photon yield and the blue line is the true photon yield.

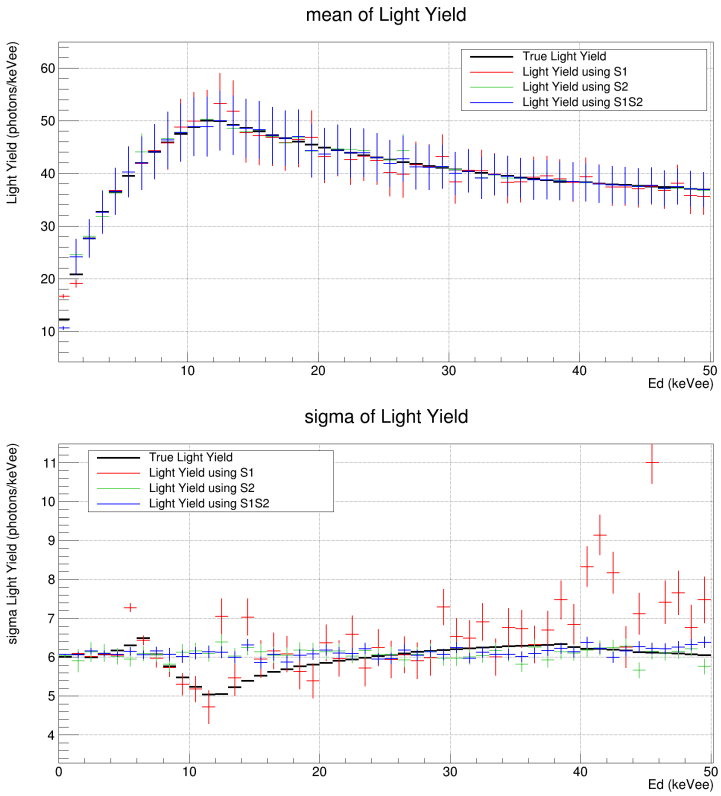

Figure 5.10: Top: mean of the photon yield obtained with S1 only (red line), S2 only (green line), both S1 and S2 (blue line) and true photon yield (black line). Bottom: the same but for the width of the photon yield distribution.

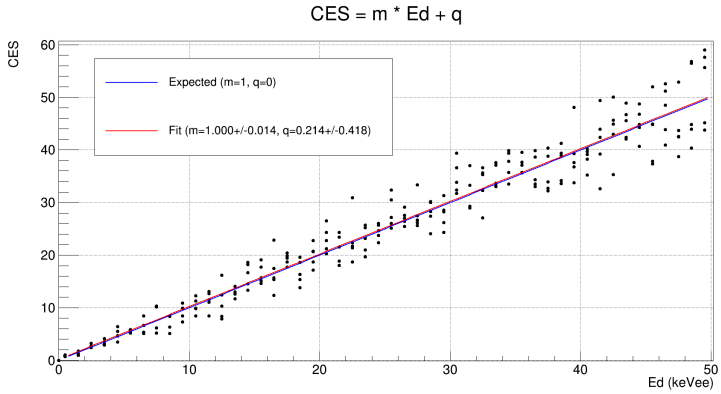

Figure 5.11: Fit to CES *vs.* true E_d. The red line is the fit function and the blue line is the expectation.

- electron-ion recombination fluctuations Δr in liquid xenon, considered as free parameter, as function of the energy, to be fine tuned with the data; in fact, intrinsic fluctuation on the recombination are not negligible, as reported by LUX measurements [96]. The electron-ion recombination fluctuations are considered to be

Gaussian-like:

$$r \sim \mathcal{N}(\langle r \rangle, \Delta r)\,. \tag{5.23}$$

In particular, the reference curves for $\langle r \rangle$ and Δr are initially chosen from NEST version 0.98 and LUX, respectively.

- due to the big non-uniformity of the PDE across the LXe volume, the Fiducial Volume (FV) chosen in this study is defined as 50% of the volume in the radius, removing the top and bottom part, such to minimize the position-dependent S1 and S2 signal variation. Moreover, in order to avoid systematic effects due to a non-uniform drift field, the central FV is further divided into 7 small FVs.

- each FV has different PDE and secondary scintillation gain.

- the primary g_1 and secondary g_2 scintillation gain have been obtained by applying the linear anti-correlation fit on several gamma lines, derived by the NEST equivalence (Equation 4.1):

$$\frac{E}{W} = n_\gamma + n_e = \frac{S1}{g_1} + \frac{S2}{g_2} \tag{5.24}$$

- the total number of photoelectrons from the prompt and proportional scintillation signals have been digitized, in order to reconstruct S1 and S2, accounting for the zero length encoding of the digitizers and the interference of noise in the baseline calculation; they have been modeled with a Gaussian.

In the previous Chapter, we have tested the NEST model, concluding that it predicts quite well the average values of detector response, but it does not match the data when considering the width of the distributions; for this reason an improvement to the MC model was required and developed in the current Chapter. The smearing of the signal distributions is governed by the recombination fluctuation Δr, the instrumental and statistical fluctuations. While the instrumental fluctuation can be minimized by improving the detector condition and the analysis corrections, the recombination fluctuation Δr remains the least known uncertainty of the detector response model to ERs. Figure 5.12 shows the results of the photon yield simulated with MCMC, together with the average recombination $\langle r \rangle$ and its fluctuations Δr, when an electric field equal to 400 V/cm is applied. In the photon yield plot, the dashed line is the initial guess based on NEST v0.98 (also Figure 4.16 top), while the yellow shaded region represent the results from LUX, shown as reference. The photon yield obtained from our data looks consistent with results reported by LUX. In the plots of the average recombination $\langle r \rangle$ and its fluctuations Δr, above 14 keV the dominant uncertainties are from the fit due to the small statistics near the endpoint energy of tritium beta decay; below 2 keV, the uncertainties increased because of the S1 detection efficiency drop below 5 PE.

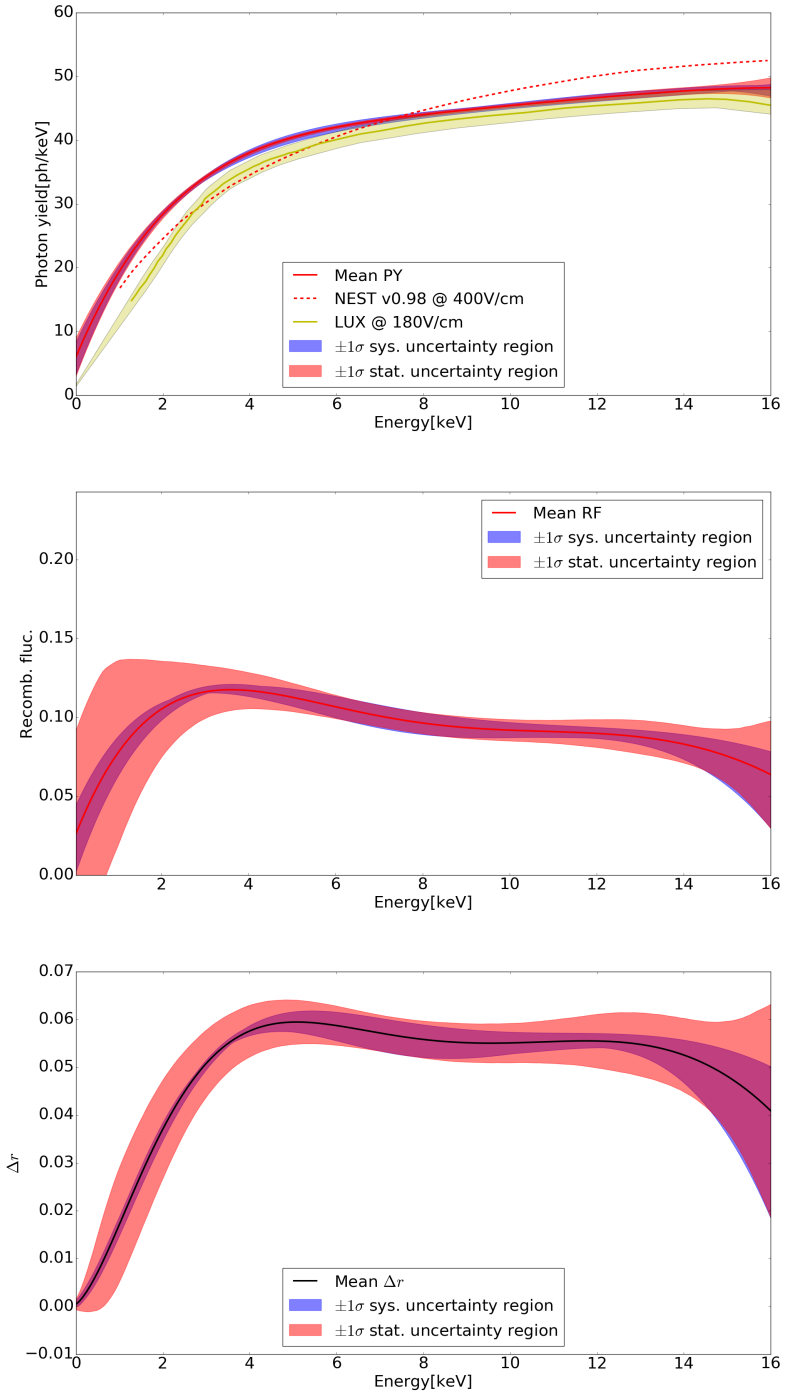

Figure 5.12: Best estimate of the photon yield (top), average recombination $\langle r \rangle$ (center) and recombination fluctuations Δr (bottom) as a function of deposited energy, obtained from the fit on tritium calibration data, at 400 V/cm drift field. The solid line represent the mean value and the shaded regions indicate the 1σ systematic and statistical uncertainties. In the top panel, the dashed line is the initial guess based on NEST v0.98 and the yellow distribution is the one obtained by LUX [96], shown for comparison.

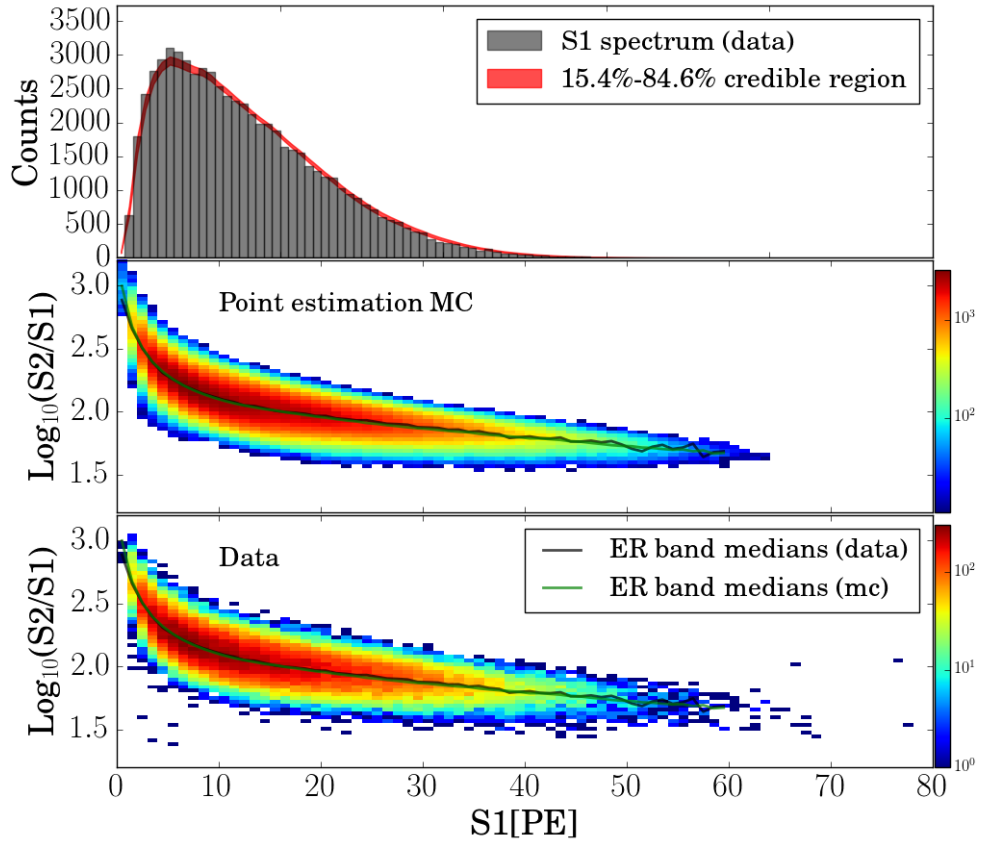

Figure 5.13: Comparison between the MC fit result (middle) and the data from tritium (bottom). The ER band $\log_{10}$(S2/S1) *vs* is plotted as function of S1 for a drift field of 400 V/cm. The S1 spectrum is shown on the top panel, together with the 15.4%-84.6% credible region from the fit in red [95].

Finally, the comparison of the fit result to tritium data, relative to the ER band $\log_{10}$(S2/S1) *vs* S1, is shown in Figure 5.13. We define here as "point estimation" the posterior distribution of the ER band, which has been obtained using the affine invarian MCMC method for maximizing the likelihood and sampling the parameter space. The black and green curves, indicating the ER band medians extracted from data and point estimation respectively, are well overlapping, meaning that the fit procedure worked correctly. As a reminder, the comparison of ER band between MC and data has been shown already in the previous Chapter, Figure 4.14 top, where the matching did not look fine, especially in the higher energy range. The S1 distribution of the data is shown in the top plot, together with the fit in red (15.4%-84.6% credible region). The improvement in the MC, as a result of the Bayesian posterior, appears clearly comparing to the NEST model, Figure 4.17 top, and fit perfectly the data.

As a general conclusion, the posterior distribution of the photon yield has been retrieved, allowing to improve the NEST model, specially in the

higher energy region. In particular, the initial guess of the photon yield has been taken by NEST v0.98 (Figure 4.16 top), and the results obtained using a Bayesian fit looks consistent compared to those measured by LUX. Moreover, the results from fit have been validated through comparison to the S1 distribution and ER band: the matching is now perfect.

The results provide new informations that are relevant to the design, operation and calibration of future liquid xenon based dark matter detectors. Finally, the photon yield extracted from this work is currently used to predict the electromagnetic background in XENON1T.

Chapter 6

Muon-induced neutron background in XENON1T

The XENON1T detector is located underground in the Hall B of LNGS. The muon flux reaching the experimental hall is $(3.31\pm0.03)\times10^8$ $\mu/\mathrm{cm}^2\mathrm{s}$ [97], with an average energy of 270 GeV [98]. In order to reduce neutrons and gammas from rock radioactivity and muon-induced neutrons, produced by muon spallation of nuclei or electromagnetic and hadronic cascades generated by muons, the XENON1T TPC has been installed in the center of a large cylindrical tank filled with water, or *water tank*, that acts as a passive shield. In fact, few meters of water constitute an effective shield against neutrons and gammas produced by rock radioactivity; the residual background is given by muon-induced neutrons with a flux of $7.3\cdot10^{-10}$ n/s [99] (for neutrons with energy greater than 10 MeV) and energy spectrum up to tens of GeV, reduced by about 2 order of magnitude by 4 meters of water. In order to tag muons or electromagnetic and hadronic cascades generated by muons, the water tank has been equipped with photomultipliers, acting as a Cherenkov detector, the *Muon Veto* (MV). The muon flux inside the water tank is about 0.04 Hz; moreover, from MC simulation we expect in the TPC 1.2 μ/hour.

In this Chapter I report a detailed description of the MV system for which I was involved from the tests of PMTs to the installation and the operation of the detector. Moreover, a muon analysis to tag muon-induced neutron events is described and is part of the results released by the XENON1T Collaboration for the first science run of data [58].

6.1 Muon Veto system

The XENON1T water tank consists of a cylindric tank, 9.6 m in diameter and 10.2 m in height, filled with deionized water. It is used as a passive shield, attenuating the flux of neutrons and gammas from rock radioactivity and of muon-induced neutrons. The flux suppression in different layers of water, is shown in Figure 6.1 [77].

The residual muon-induced neutrons background is tagged by the

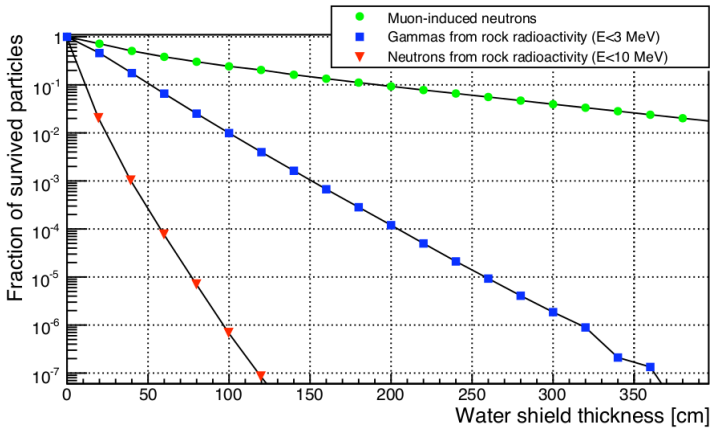

Figure 6.1: Fraction of neutrons and gammas from rock radioactivity (red and blue dots respectively) and of muon-induced neutrons (green dots) as a function of the thickness of the water shield surrounding the detector.

MV system [59] (Figure 6.2), an active shield made of 84 8-inches photomultiplier tubes Hamamatsu R5912ASSY, with a water-proof enclosure, mounted in the water tank. The PMTs have a bialkali photocathode

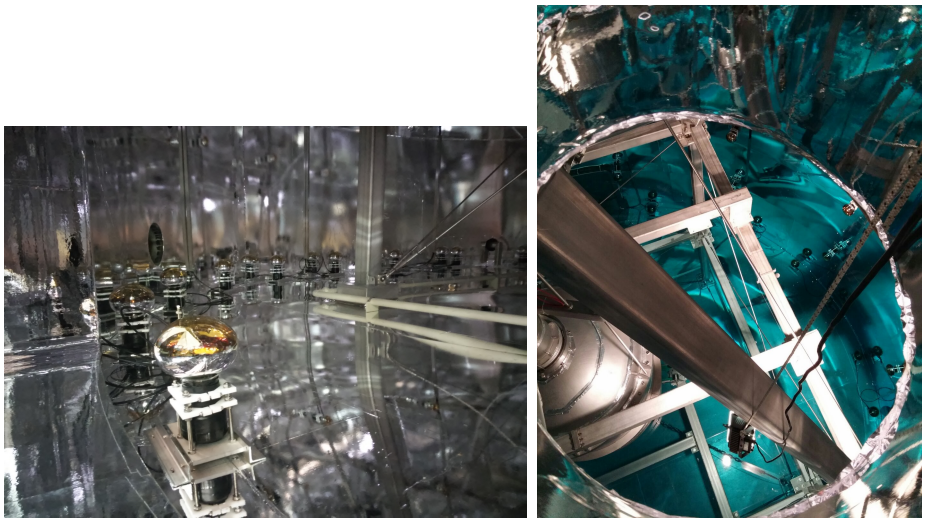

Figure 6.2: Picture of the MV system, as seen from the bottom part, without water in the tank (left) and from the top flange, with water in the tank (right).

and borosilicate glass window. Their quantum efficiency is around 30% in the Cherenkov wavelength range [300,600] nm and the average gain is 6.2×10^6 for typical voltages of 1500 V. The PMTs have been arranged in 5 rings at different heights. In the bottom (z=0 m) and top (z=10 m) are located 24 PMTs equally spaced in angle and the remaining 3 rings are constituted by 12 PMTs each (at z=2.5 m, z=5 m and z=7.5 m respectively). In order to maximize the photon detection efficiency,

the inner walls of the water tank have been covered by a reflective foil, that acts both as a ∼99% reflector between [400,1000] nm wavelength and a wavelength shifter to the PMTs sensitivity range. In case the MV has detected a charged particle, the consequent event recorded by the TPC would be removed from analysis.

6.1.1 DAQ

The XENON1T TPC and MV share the same Data AcQuisition system (DAQ). They can operate either simultaneously, for instance during dark matter runs, or separately, for calibrations. The PMT signals from the MV are digitized by 11 flash ADCs (100 MHz CAEN, model V1724) with 14 bit of resolution and 0.5 V of dynamic range. All ADCs share the same external clock, to ensure that they are properly synchronized and have identical time stamps. One computer (*MV reader*) is used for the read-out of the ADCs; in case of the TPC, 6 computers (*readers*) have been employed in parallel for the data acquisition.

The DAQ is controlled through web interface (no VPN required) [100], such that also non-experts can monitor the quality of the incoming data. In particular, one can select a run (MV run, background, calibration with source, LED calibration, *etc.*), start/stop a new run, check the data acquisition rate, receive alarms in case of problems with DAQ, close the alarms once the DAQ experts have fixed the problem, *etc.* Once a run is finished, the data is stored in a MongoDB noSQL database made of 3 parallel computers (together forming the so called *xe1t-datamanager*). A screenshot of the DAQ control panel is shown in Figure 6.3, together with the list of runs in the run database and the details of one MV run as example.

Another computer parallel to the TPC acquisition machines, the *acquisition monitor*, continuously stores informations related to the run, such as the analog sum-waveform, veto on/off, busy signal, *etc.* The last one is used to precisely predict the deadtime of a run. Of particular interests for the MV is the time stamp of each MV trigger. The MV employs a classical coincidence trigger (based on a CAEN V1495 VME unit) and a copy of this signal is sent to the TPC system. Thus, we can use the time of a MV trigger from MV data and from the acquisition monitor in order to synchronize MV and TPC (see Section 6.2).

Given the big amount of data produced by the TPC, the raw data from both MV and TPC systems remains temporary on the xe1t- datamanager and then automatically transferred to dedicated grid storage points, where they are processed. The overall DAQ scheme is shown in Figure 6.4 [60].

The data processor derives high-level quantities from the digitized waveforms which are stored in files accessible through a JupyterHub infrastructure.

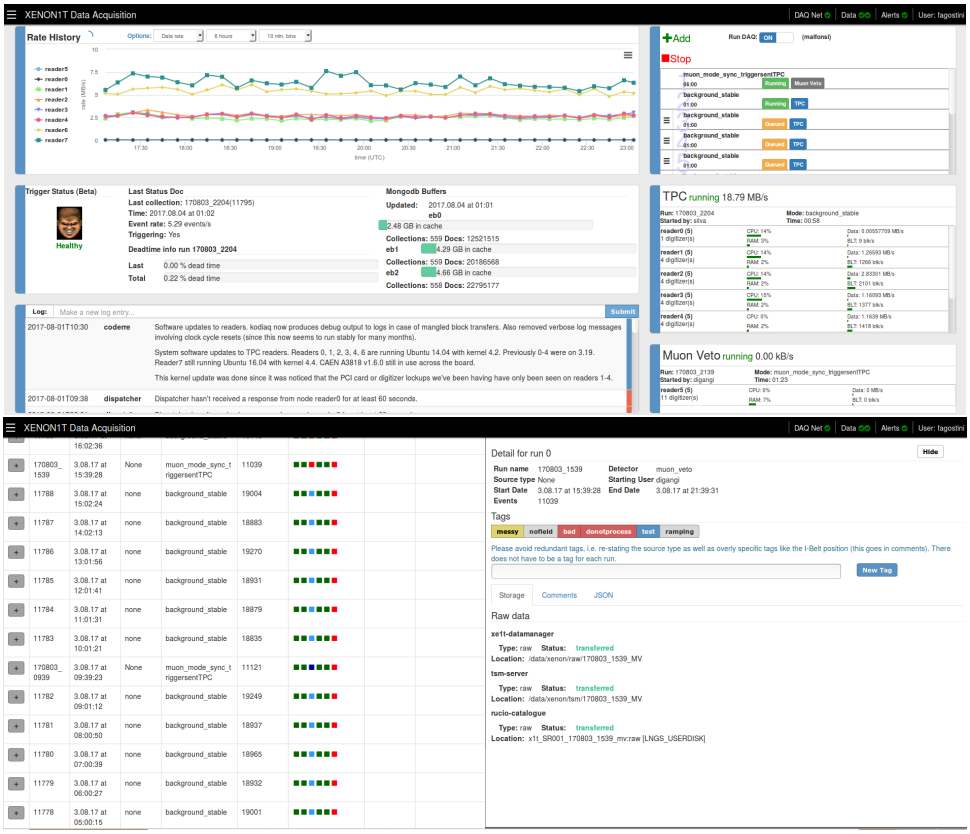

Figure 6.3: Screenshot of the DAQ web control (top) and run database with a MV run selected (bottom).

6.1.2 PMT calibration

For the calibration of PMTs of the MV system, two blue LED pulsers, with 8 independent channels each, have been emploied. In particular, we are using two parallel calibration systems (Figure 6.5):

- 84 PMMA optical fibers, individually illuminating one PMT;
- 4 diffuser balls, mounted on the cryostat support structure, for homogeneously calibrating the full system.

The optical fibers are grouped in 12 boundles, each one connected to one channel of the LED pulser; one boundle contains 7 fibers. The remaining 4 channels of the LED pulser are connected to one diffuser ball. From calibration purposes, an external clock generates the trigger to the 2 pulsers and is simultaneously sent and shared among the 11 flash ADCs. A sketch of the MV calibration system is shown in Figure 6.6.

The MV PMTs and the related calibration systems, are operated, controlled, monitored and recorded by a slow control through web interface (requires VPN), as for the other XENON1T subsystems. In particular, one can turn on/off the PMT voltages, as well as change their value. The web interface is used also for setting different calibration modes, as the

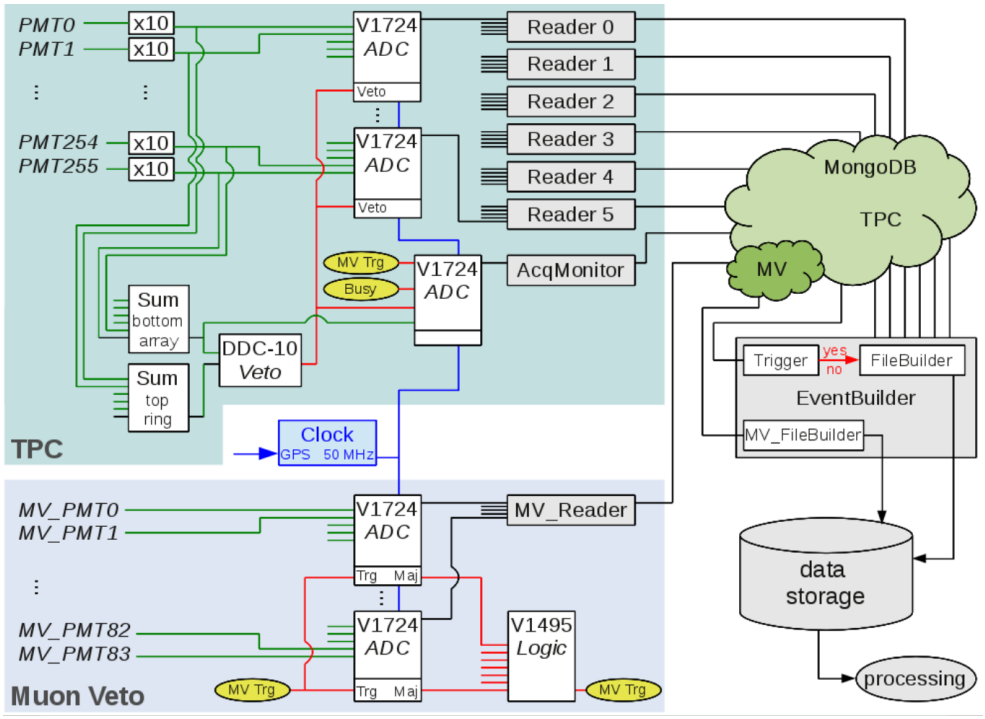

Figure 6.4: Scheme of the XENON1T DAQ system for the MV and TPC.

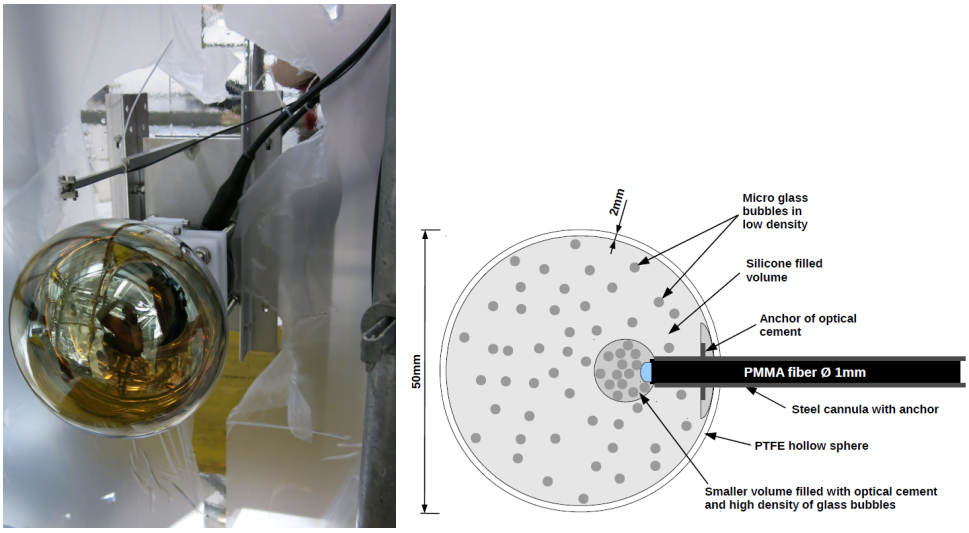

Figure 6.5: Optical fiber mounted on one PMT (left) and sketch of the diffuser ball (right).

voltage of the pulser, its width, frequency, *etc.* An example of the slow control web interface for the PMT voltages is shown in Figure 6.7, as well as the PMT calibrations modes.

Single photoelectron calibration

For simplifying the MV analysis, we have set the voltage required to have the same gain on each PMT. Experimental measurements on the

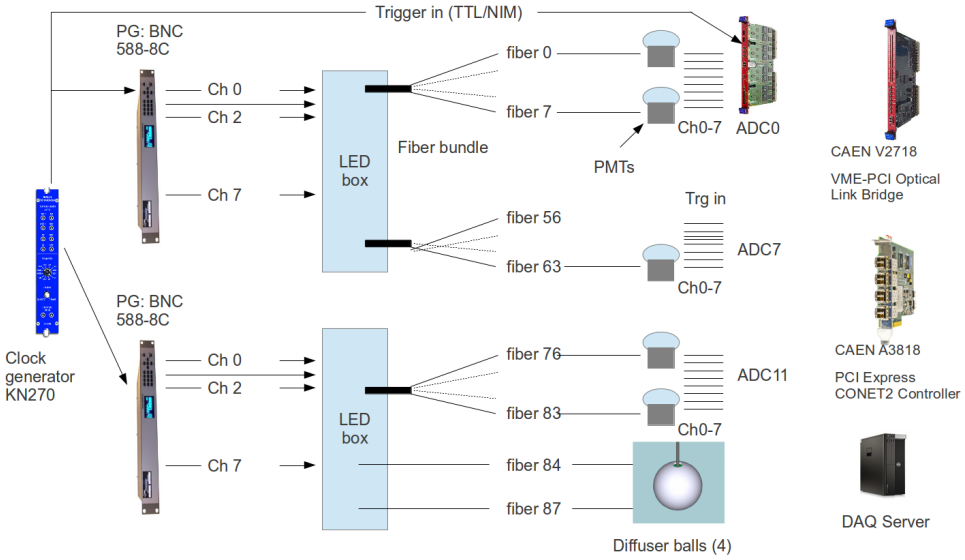

Figure 6.6: Sketch of the MV calibration system.

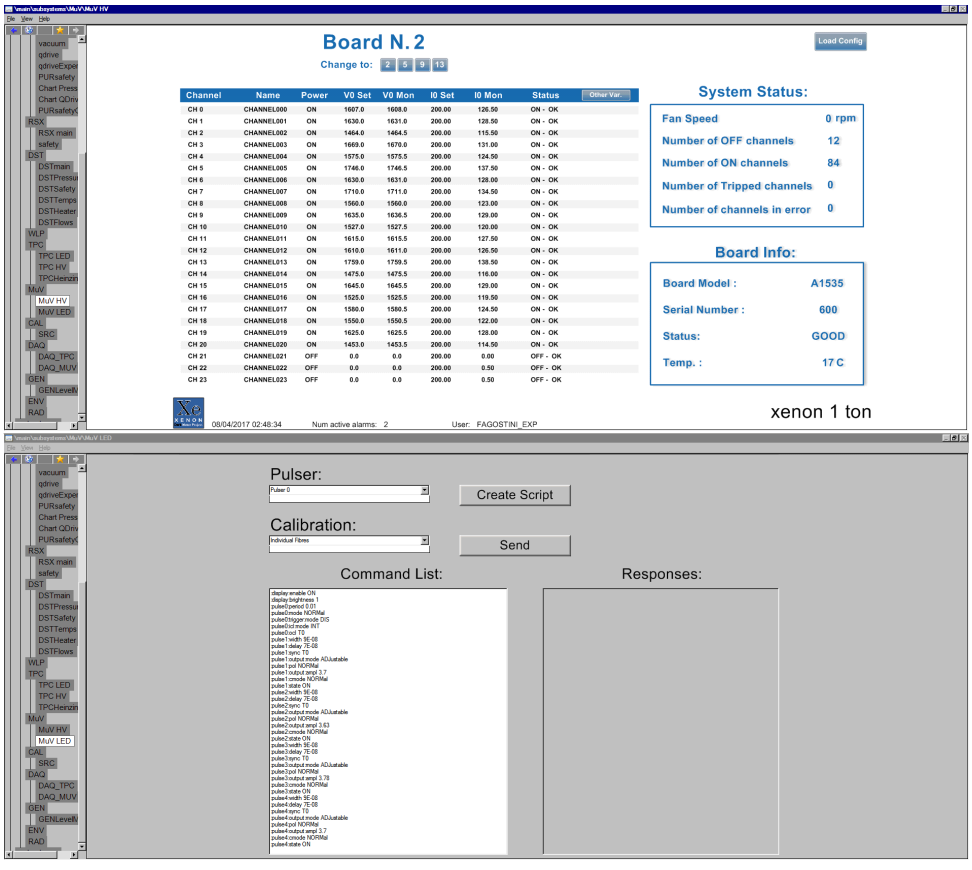

Figure 6.7: Screenshot of the MV slow control through web interface: PMT voltages (top) and Pulser settings (bottom).

gain dependence on the applied voltage have been performed in [101], where the MV PMTs have been previously tested in a separated apparatus. In particular, the value of the voltage which would give 1 pC as charge of the Single PhotoElectron (SPE), *i.e.* 6.02×10^6 gain, has been set per each PMT.

From a SPE calibration with diffuser balls (Figure 6.8) we can conclude that all the PMTs see light and are properly working; moreover the diffuser balls illuminate homogeneously the PMTs without creating black points in the tank. The position of the single photoelectron peak in the

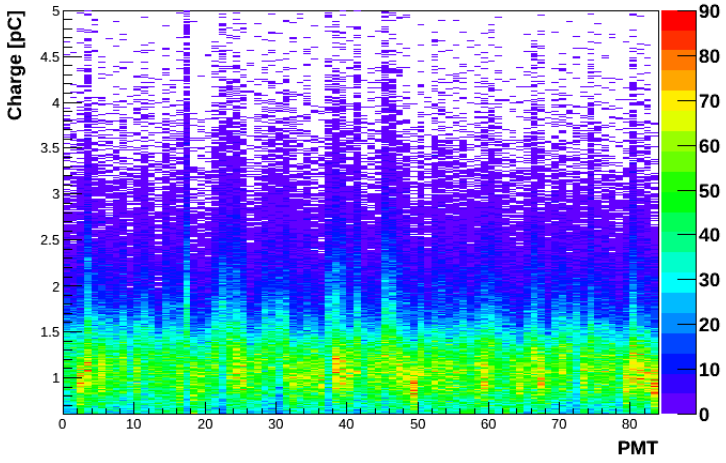

Figure 6.8: Single photoelectron calibration using diffuser balls: plot of the charge *vs* PMT position.

charge distribution looks always the same in all the PMTs, meaning that they are properly equalized in gain. Anyway, in order to make a more precise statement we have to fit the SPE spectrum with a proper fit function. The fit function used here, accounts for the Gaussian noise around 0 pC (*pedestal*); the Gaussian single photoelectron response around 1 pC; the exponential sub-amplified photoelectrons. Thus, it is written as:

$$f(x) = A_N e^{-\frac{1}{2}\left(\frac{x-\mu_N}{\sigma_N}\right)^2} + A_{s.p.e.} e^{-\frac{1}{2}\left(\frac{x-\mu_{s.p.e.}}{\sigma_{s.p.e.}}\right)^2} + p0 \cdot e^{p1(x-p2)} \,. \qquad (6.1)$$

Sub-amplified photoelectrons are due to inelastic scattering of electrons off the first dynode, which do not acquire enough energy to extract secondary electrons, electrons deviating the electric field, that skip the first dynode, photons generating photoelectric effect in the first dynode, rather than in the cathode, *etc.* An example of the single photoelectron fit is shown in Figure 6.9; the value $\mu_{s.p.e.} - \mu_N$ gives us the charge of single photoelectron.

The charge of SPE per each PMT extracted by the fit function has been calculated for all the PMTs, together with the PMT resolution:

$$res = \frac{\sqrt{\sigma_N^2 + \sigma_{s.p.e.}^2}}{\mu_{s.p.e.} - \mu_n} \,. \qquad (6.2)$$

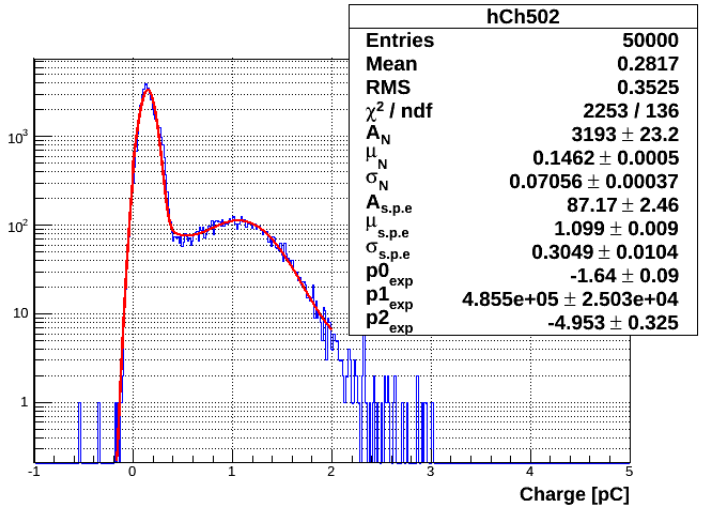

Figure 6.9: Fit to single photoelectron distribution of a MV PMT. The charge of single photoelectron is given by $\mu_{s.p.e.} - \mu_N$, around 1 pC.

In Figure 6.10 is shown the charge distribution of single photoelectron pulses for each PMT and the relative resolution, both fitted with a Gaussian. The resolution of the MV PMTs is found to be around 37%, while

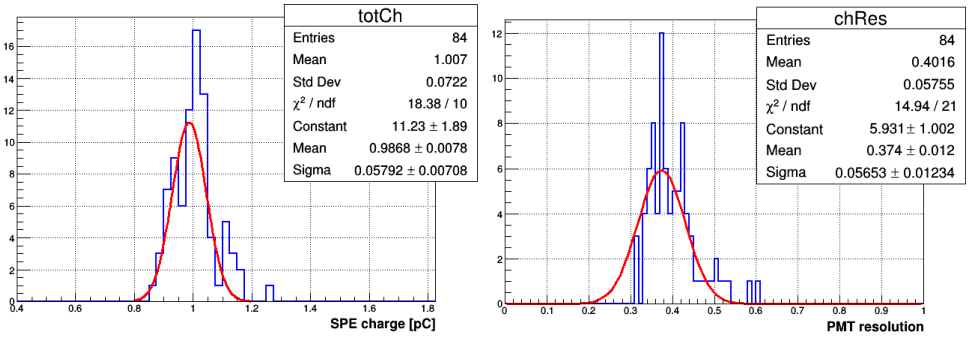

Figure 6.10: Single photoelectron charge of 84 PMTs (left) and resolution (right), fitted by a Gaussian (red line).

the average charge of single photoelectron is (0.987±0.008) pC. All PMTs have approximately the same gain. only 14 PMTs differs more than 10% from the SPE mean charge, but remains inside 20%, thus we can consider the PMT gain homogeneity sussesfully achieved.

6.1.3 MV tagging efficiency

The Muon Veto system is provided with a trigger unit, CAEN mod. V1495, which is designed (by means of custom firmware) to generate an internal trigger to the MV following a predefined condition. The conditions used during the MV operations are:

- Thr=1 PE: the amplitude of the signal has to be greater than 1

photoelectron and is set per each PMT, from the results on the PMT SPE calibrations;

- TOT=1: the consecutive Time samples Over the Threshold have to be more than 1 (*i.e.* 10 ns);

- N≥8, or *multiplicity*: the minimum number of PMTs ON in coincidence inside a certain time window Δt has to be greater than 8;

- Δt=300 ns: is the coincidence window, optimized by a MC simulation (Figure 10 of [77]).

When the above conditions are fulfilled the trigger unit generates a global trigger and all 84 PMTs digitized signals in a time window of 5.12 μs are stored. Moreover, a copy of the trigger signal is sent to the TPC acquisition monitor, where it gets stored. The hardware rate was measured to be 0.35 Hz. In case the MV has detected an interesting event, the consequent event recorded by the TPC would be discarded at the analysis stage, meaning we can in any case check what happens in the TPC even when the MV is triggering.

A detailed MC simulation of muons in the Hall B of LNGS has been tuned to the MV data during the commissioning phase [102]. In particular, we consider dangerous events for dark matter search as those with at least one neutron at the surface of the water tank, with a neutron energy of at least 10 MeV; in fact, it could reach the TPC and scatter with NR in the low energy, the same as for WIMPs. Thus, the residual background due to neutrons crossing the whole water shield, producing a single scatter nuclear recoil in 1 ton fiducial volume and in the [5,50] keV energy range, has been estimated. The selected events are divided in two different sub-samples:

- *muon events*: muons passing into the water tank,

- *shower events*: muons passing outside the water tank (which interact and induce electromagnetic or hadronic shower inside).

In both the cases, the charge particles passing inside the water tank emit Cherenkov radiation which is tagged by the MV.

The MC tagging efficiency for muon events and shower events fulfilling the trigger conditions Thr= 1 PE, TOT=1 and Δt=300 ns, as function of the PMT multiplicity N is shown in Figure 6.11. When the multiplicity is N≥8, the simulated tagging efficiency results 99.5% for muon events and 43% for shower events. The residual background of muon-induced neutrons in 1 ton fiducial volume of the TPC is summarised in Table 6.1. From this estimation, we can conclude that with the MV, the nuclear recoil background from muon-induced neutrons is suppressed by a factor of 2.5.

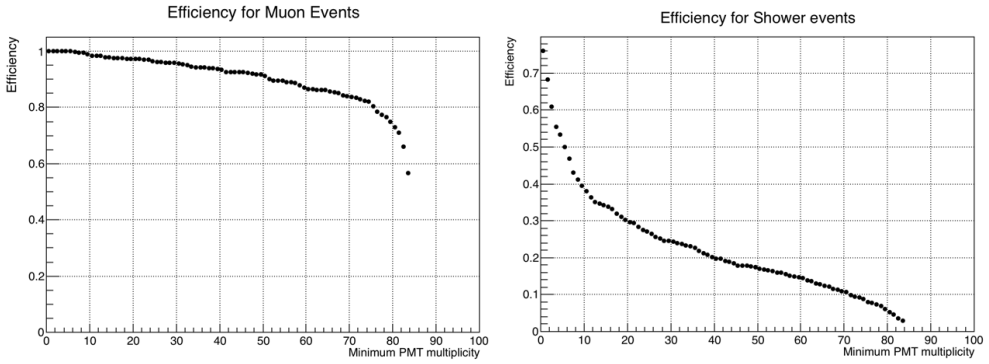

Figure 6.11: MV efficiency in tagging muon events (left) and shower events (right) as function of the multiplicity (Thr= 1 PE, TOT=1 and Δt=300 ns).

rate [evt/y] in 1 ton	muon events	shower events	total
before MV cut	$9{\cdot}10^{-3}$	$2.1{\cdot}10^{-2}$	$3.0{\cdot}10^{-2}$
tagging efficiency	99.5%	43%	
residual background rate	$5{\cdot}10^{-5}$	$1.2{\cdot}10^{-2}$	$1.2{\cdot}10^{-2}$

Table 6.1: Residual background rate of muon-induced neutrons inside 1 ton fiducial volume, after applying the MV tagging efficiency.

6.2 Synchronization of MV and TPC using muons

The Muon Veto setup in XENON1T has been meant to provide a time synchronization with the TPC system. They are two independent systems, which are able to run alone, even if the other system is down. The two systems are based on the same device, the CAEN digitizer V1724; anyway, during the commissioning phase and the first science run, they were not sharing the same clock. Later, a GPS timing unit, relevant also for supernova detection, has been install (and tested) in the MV frame; the time signal would be optionally used for giving a common reference time in the TPC and MV.

Moreover, the event time is given by the time when the run starts, plus the time to the next event. Since the flash ADCs have an internal counter which assigns a time to the trigger, *Trigger Time Tag* (TTT), with 31 bit resolution, it restarts every $\sim$21 s. In the case of MV, with low aquisition rate (0.35 Hz), this results in a wrong time tag when two consecutive events are separated by more than 21 s. Thus, in order to bypass the problem of rollover, on January 23rd 2017, an additional trigger with a fixed frequency of 0.1 Hz has been added to the MV: the *synchronization signal*. The resulting MV trigger rate is 0.45 Hz. The synchronization signal has been sent to the TPC, such that the time difference among TPC and MV is only due to hardware.

Anyway, in this work I always refer to the MV time coming from the

acquisition monitor (installed in the TPC frame), such that we do not face hardware synchronization problems; the only shrewdness one has to keep in mind is that the synchronization signal has to be removed from the data, in the analysis phase.

6.2.1 Hardware synchronization

The acquisition monitor is a file that has been stored any time we start a run with the XENON1T TPC. It is located in the raw data folder and collects basic informations related to the run; of our interests is the time stamp of each MV trigger ("real" trigger plus synchronization signal), and the time stamp of the 0.1 Hz pulse alone. By rejecting the MV triggers closest in time to a 0.1 Hz pulse, one gets the "real" MV trigger only. In fact, since both the signals are read from the same system (the acquisition monitor), the delay time is very narrow, only due to hardware, *i.e.* cables. Figure 6.12 shows the time delay of the synchronization signal and the closest MV trigger, before and after installing the GPS unit, which constitute a different hardware configurations. It looks very

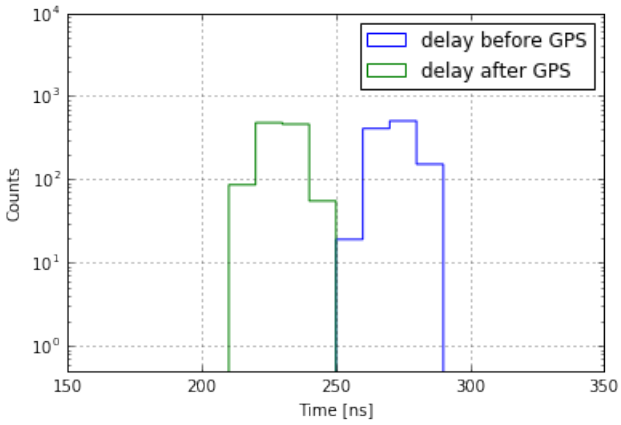

Figure 6.12: Closest time difference between a MV trigger and the syncronization signal, before (blue line) and after (green line) installing the GPS unit.

narrow, around 270 ns before installing the GPS unit and 230 ns after its installation. Based on these results, the way that will be used from now on to select "real" MV triggers only, is to reject MV triggers closer than 300 ns from a syncronization pulse.

The time distribution of two consecutive MV triggers is expected to follow a Poissonian probability; due to the presence of the synchronization signal, we can not have consecutive events more distant than 10 s in time, and this results in a cut-off (Figure 6.13). We have now some comment. First, in blue is shown the time difference dt between any two consecutive pulses, without any kind of further selection. Anyway, a peak around zero, increasing while decreasing the bin width, point us to an afterpulse effect, happening around 10 μs from the main pulse. In

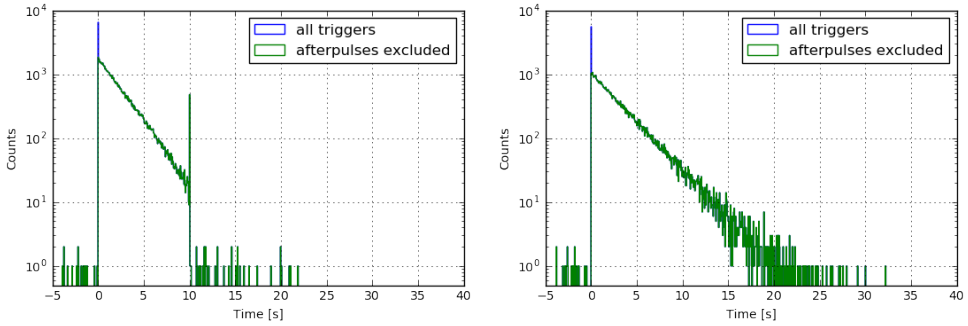

Figure 6.13: Time difference of two consecutive MV triggers, considering all the triggers (left) and "real" MV triggers only (right).

fact, if a muon crosses the water tank, it emits a large amount of photons and the probability to have an afterpulse increases with the light produced. In some case, the afterpulses are synchronized among PMTs and if the PMT signal satisfies the MV trigger conditions, a new trigger is sent to TPC, while the MV is in Busy mode. Thus, in order to exclude afterpulses (green line), we require that dt >10 μs. Second, we notice few events with a negative dt; several checks have been performed in order to find out their origin (if they belong to the same run, if the time distance from the beginning/end of a run is constant, if the previous/next event looks strange, *etc.*), but no correlation has been found. In order to go on with the analysis, the trigger events have been re-ordered by time. Third, 48 events have dt greater than 10 s, even though the syncronization signal is not rejected. In these cases, they belong to the beginning of the run; thus, we have also learned that the automatic starting of a new run takes 10-20 s of delay.

In conclusion, we have demostrated that an efficient technique based on the time difference between each syncronization signal and the closest MV trigger, allows to obtain only "real" MV trigger events, of interest for this study.

6.2.2 Synchronization using muons

Now we want to study the synchronization of the MV with TPC, by using muons. In fact, since muons cross MV and TPC almost instantaneously, the delay time should be only due to electronics. From the MC, we expect that the muon rate in the TPC is around 1.2 evt/hour. Moreover, given the timing informations of the PMTs it is possible to reconstruct single muon tracks inside the water tank (Figure 6.14)

The analysis has been performed by looking at the TPC response to a muon event triggered by the MV, meaning we consider TPC data only; here 2 days of data have been analyzed. The parameters of interests in this analysis is the time difference between a TPC event and the closest MV trigger, as obtained by the acquisition monitor. A zoom on

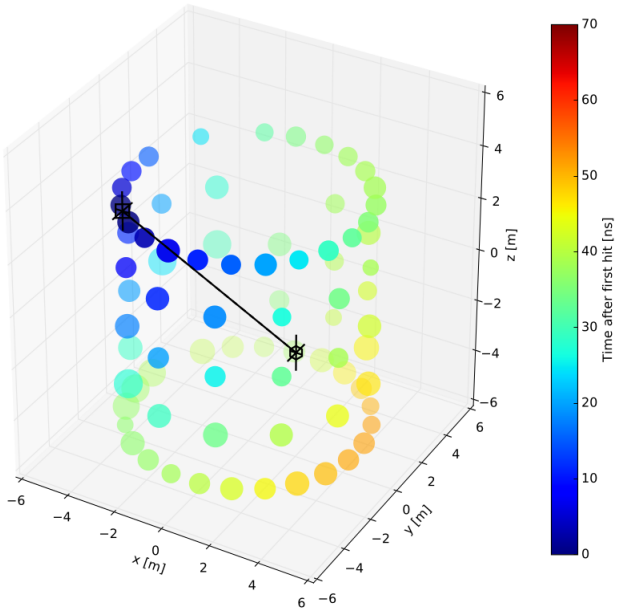

Figure 6.14: The timing information of light reaching the PMTs of the MV (coloured points) allows to reconstruct the muon track (black line) inside the water tank (black line).

the μs region should show us an eventual coincidence among the two systems (Figure 6.15). The results are very symmetric in the range of

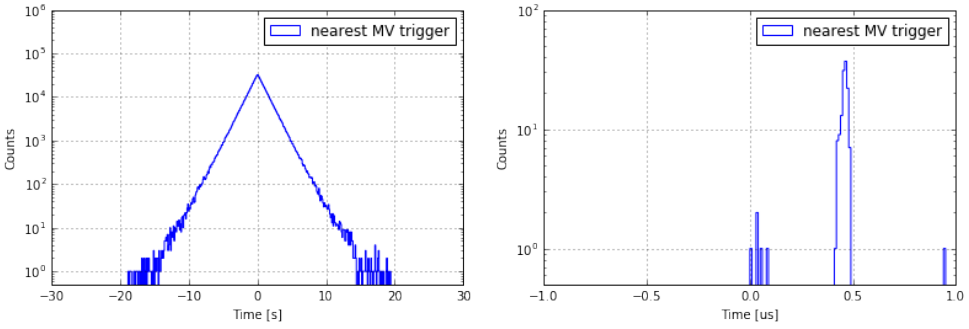

Figure 6.15: Time difference between a TPC event and the closest MV trigger in the second region (left) and in the μs region (right).

seconds and agrees with the expectations. From the zoomed distribution one can clearly see the narrow population of 128 events at around 450 ns, due to muon candidates. The time delay between TPC and MV results in agreement with the time for creating the MV trigger and it is systematically positive, with the MV trigger happening after a TPC event, as expected.

In order to understand if there are real populations or just random coincidences of MV and TPC events, we can calculate how many accidental coincidences we expect and compare the numbers with the one extracted from the data. We are also interested in checking if we can

catch some neutron capture from the data, that would mean a muon that passes through the water tank triggers the MV, and induces a neutron that with some delay is captured and triggers the TPC. In Table 6.2 we report the number of accidental coincidences between MV trigger and TPC events in a certain time window, obtained as follows:

- *Expected* coincidences: we consider a MV rate equal to 0.35 Hz and almost 10^7 TPC events,
- *Data (negative)*: we calculate the number of coincidences in the negative part of Figure 6.15, in order to check if any neutron capture occured,
- *Data (positive)*: we calculate the number of random coincidences in the positive part of the plot, starting from 1 μs (in order to avoid the population of muon candidates).

	Expected	Data (negative)	Data (positive)
1 μs	0.3±0.6	0	0
10 μs	3.4±1.9	4	4
100μs	34±6	30	35
1 ms	342±19	322	334

Table 6.2: Number of accidental coincidences in a certain time window.

The expected accidental coincidences agree with the measured ones (inside errors), thus the population around 450 ns can be truly considered as muons. Moreover, since in the negative side of the time delay there is not an excess of events, we can not recognize any neutron capture in the TPC, that would have opened the door to a still not investigated physics.

Since a muon crossing the TPC releases a huge amount of energy (*i.e.* photoelectrons), there should be some correlation between the total charge of a TPC event and the closest MV trigger. The charge spectrum of the events selected as muon candidates, below 500 ns time delay from the closest MV trigger, is inspected, doubling the statistics (Figure 6.16). The population of alligned events with high total area corresponds to the events already tagged as muon candidates, or at least related to the muon physics. In particular, their total charge spectrum looks composed by an exponential contribution in the lower part and a flat shape; the discrimination happens at around $2{\cdot}10^7$ PE. Thus, we separate the two type of events by their charge and interpret them as:

- charge$<2{\cdot}10^7$ PE and 500 ns coincidence time: 53%, rate=1.3 evt/hour. Muons interacts with the cryostat, leaving a smaller amoung of energy in the TPC;
- charge$>2{\cdot}10^7$ PE and 500 ns coincidence time: 47%, rate=1.2 evt/hour. Muons crossing both MV and TPC.

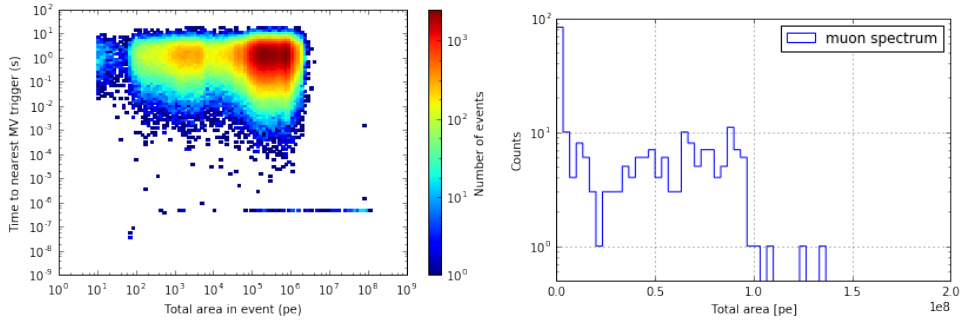

Figure 6.16: Closest MV trigger *vs.* total area of a TPC event (left) and charge distribution of selected muon events (right). The selection criteria is based on the coincidence between a TPC and MV trigger, inside 500 ns.

The extracted rate of muons crossing both MV and TPC agrees with the MC predictions. An example of a waveform of such event, characterized by a first big S1-like signal, and a long S2 signal (hundreds μs), is shown in Figure 6.17.

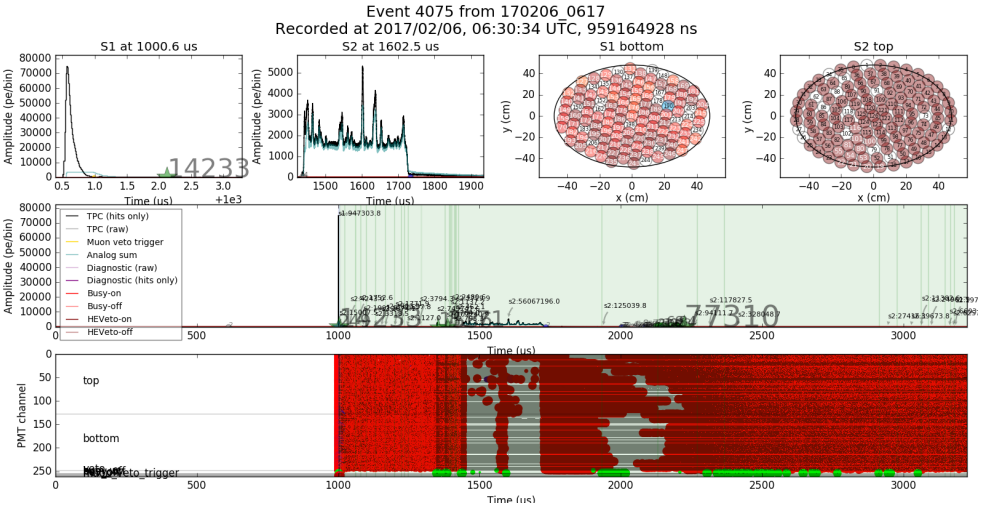

Figure 6.17: Waveform of an event where a muon crosses the TPC: it is characterized by a first big S1-like signal, and a long S2 signal (hundreds μs).

6.2.3 Muon Veto cut

As a conclusion from the previous Section, the rate of muons crossing both MV and TPC is around 1.2 muons/hour when selecting the events in coincidence inside 500 ns and with area greater than $2{\cdot}10^7$ photoelectrons and agrees with the expectations. Other TPC events in coincidence with the MV but with smaller area should be anyway related to the physics of muons crossing the water tank.

The presence of these events in tight time coincidence allows us to define a time region around the TPC time t_{TPC} in which to look for muon-related background. In particular, we can veto a time of 1 ms after a MV trigger occurs (t_{MV}), defined as

$$-1\,ms < t_{MV} - t_{TPC} < 1\,\mu s\,, \tag{6.3}$$

where in the positive side we reject muons crossing MV and TPC according to the previous study, and in the negative side we conservatively reject eventual neutrons induced by muons. Given the MV trigger frequency (0.35 Hz), the probability of a chance coincidence will be

$$P = 1.001 \cdot 10^{-3} \cdot 3.5 \cdot 10^{-1} = 3.5035 \cdot 10^{-4}\,. \tag{6.4}$$

Thus, the acceptance of the cut to dark matter event is 99.96%.

6.3 Muon-induced neutron background for Science Run 0

The first science run of XENON1T (or Science Run 0, *SR0*) is made of 34.2 live days of data acquired between November 2016 and January 2017 [58]. The MV performances (already explained in detail above) during the SR0 is summarised as:

- the MV was active for 95% of the time (coverage),
- the tagging efficiency for muon events is 99.5% and for shower events is 43%,
- the residual nuclear recoil background from muon-induced neutrons in SR0 after applying the MV cut is $1.2{\cdot}10^{-3}$ events in 1t FV, with a reduction factor of 2.5,
- MV cut: in case the MV has triggered an event, TPC events inside 1 ms coincidence window would be discarded from the analysis,
- the acceptance for the MV cut is 99.96%,
- given the low MV trigger (around 0.35 Hz), the rate of accidental coincidences between MV and TPC (about 5 Hz during ordinary dark matter runs) makes the loss of the live time negligible.

Here we are checking for coincidences between a dangerous TPC event, *i.e.* a leakage event, and a MV trigger in the SR0.

6.3.1 Data analysis in SR0

The data selection is based on the requirements used in the dark matter search (similar to those in Chapter 4), mainly:

- single scatters,
- inside 1 ton FV,
- cS1<200 PE, in order to select low energy events only,
- basic cuts that remove noisy events.

The distribution of the events passing the cuts, in the discrimination space $\log_{10}$(cS2/cS1) is shown as a function of cS1 in Figure 6.18, top. Red circles represent the events inside 1T fiducial volume (*FiducialCylin-*

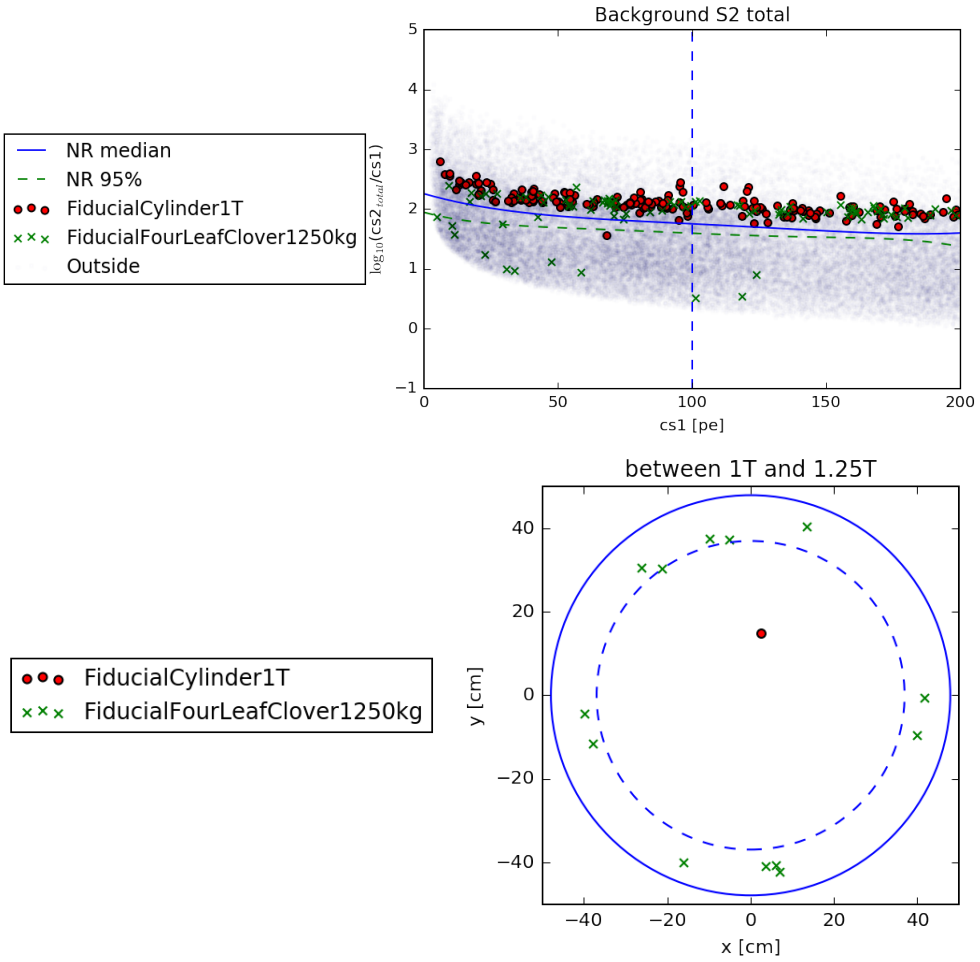

Figure 6.18: Top: distribution of events surviving the cuts for the WIMP search, defined in the first science run of XENON1T, in the discrimination space $\log_{10}$(cS2/cS1). Bottom: x-y position of leakage events (*i.e.* below the 50% NR discrimination line) inside the FiducialFourLeafClover1250kg.

der1T cut), green crosses are due to events between 1T and 1.25T (*FiducialFourLeafClover1250kg* cut) and the blue shadow stands for all the other more peripheral events. The NR median (blue line) and the 95% NR discrimination (green dashed line) is also reported in the plot. It looks very clear that the number of leakage events, *i.e.* those below the 50% NR discrimination line in the WIMP search space, increases quickly with increasing the FV.

The x-y position in the TPC of leakage events inside the 1.25 t is shown in Figure 6.18, bottom. They are 14 in total: 1 leakage event (red circle) stands inside the 1T fiducial volume, delimited by the blue dashed line, and 13 leakage events (green crosses) are located between 1T and 1.25T fiducial volume.

For each of the 14 leakage events inside the 1.25 t fiducial volume, the closest MV trigger has been calculated (Figure 6.19). We do not see

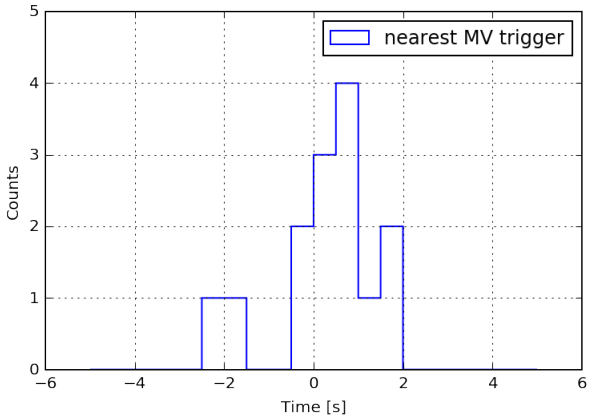

Figure 6.19: Time difference between each one of the 14 leakage events inside the 1.25T fiducial volume and the closest MV trigger.

any correlation between any of the 14 leakage events and a MV trigger, in particular:

- 9 events have a coincidence within the MV of ±1 s,
- 0 events inside ±1 ms coincidence (corresponding to the MV cut),
- of course, 0 events inside ±1 us coincidence (which would have been a muon),
- positive and negative time coincidences, as expected in absence of correlations.

In conclusion, a MV analysis on the data presented in the first science run of XENON1T, with 34.2 live days, has been developed: no time correlations between any of the 14 leakage events (inside 1.25T fiducial volume) and a MV trigger have been found, thus none of those events has been rejected. Moreover, a total of 63 events pass the selection criteria

for the WIMP search in 1T fiducial volume, but none was found within 10 ms of a MV trigger.

Conclusions

In the last decades, the dark matter has been one of the main subject in the field of astrophysics and cosmology, from both theoretical and experimental point of views. The potential discovery of dark matter would confirm the astrophysical and cosmological evidence and would strongly support the research on theories beyond the Standard Model. Big efforts have been done so far in order to design experiments which are able to find dark matter exploiting a direct detection technique, based on WIMP scattering off target nuclei, or indirect detection technique, which consists of tagging the particles produced by the decay of self-annihilation of WIMPs. The interaction of dark matter is characterized by extremely small cross sections, therefore the event rate is also very low. In order to observe dark matter through direct detection techniques, large, ultra radio-pure detectors, located in a very low radioactivity environment are required. Moreover, the background from cosmic rays is reduced by placing the dark matter detectors in underground laboratories.

The XENON project is located at LNGS, below an average thickness of rock of 1.4 km and exploits the direct detection of released by a WIMP scattering off a liquid xenon target, contained in a dual-phase TPC. The XENON1T experiment released the results from the first Science Run of data (SR0), lowering of about two orders of magnitude the limits on spin-independent WIMP-nucleon interactions set in 2012 by the previous XENON100 experiment. In particular, the minimum cross section for spin-independent WIMP-nucleon elastic scattering is $7.7\times10^{-47}\mathrm{cm}^2$ for a 35 GeV/c^2 WIMP mass at 90% C.L.

The work of this thesis is based both on XENON100 and XENON1T.

In XENON100 a study on the electromagnetic background, due to electrons or gammas scattering off xenon electrons and inducing Electron Recoils (ERs), has been developed. The ERs are efficiently discriminated from the Nuclear Recoils (NRs), a typical dark matter signal. Anyway, a small fraction of ERs falls into the discrimination band and can not be rejected, representing a dangerous background. A detailed MC simulation that predicts the electromagnetic background is even more important for XENON1T, in which the large self-shielding power of liquid xenon does not allow to reach the inner fiducial volume through usual calibration sources located outside the TPC.

A full MC simulation for the ERs has been developed, starting from matching the results with XENON100 data. The phenomenological model

used to predict the number of photons and electrons released by a particle hitting the xenon target is NEST. The first part of the simulation is uniquely related to the xenon as target material. Then, the conversion of photons and electrons into the measurable signals S1 and S2 (considering the light collection efficiency, the PMTs quantum efficiency, the multiplication of electrons in the liquid-gas interface of xenon, *etc.*), are taken into account as the detector response.

A validation of the MC simulation through comparison with ER calibration data in XENON100 is one of the subject of this work. In particular, we have simulated the detector response to 39.6 keV and 80.2 keV gamma lines from ^{129}Xe and ^{131}Xe isotopes activated by neutron inelastic scattering from AmBe; low energy Compton electrons from ^{232}Th source; beta particles from CH_3T.

From a MC-Data comparison of the S1 and S2 anti-correlated and Gaussian distributed signals as response to 39.6 keV and 80.2 keV gamma lines, we can conclude that NEST reproduces quite well the ER calibration data. Here are some conclusions:

- we can trust our MC in predicting the average values of the S1 and S2 signals;
- statistical fluctuations are different in MC and data. This fact indicates that the spread implemented in the code is too large;
- the S1-S2 rotation angle representing the anti-correlation between the signals (and the S1 and S2 sigmas) agrees with an analysis of 41.5 keV line from ^{83m}Kr in the MC;
- the rate of inelastic interactions is in a very good agreement for the 39.6 keV line.

The matching between MC and Data of the fit on the ER mean band, calculated from low energy Compton electrons from ^{232}Th source, is quite good. The number of leakage events (*i.e.* those events below the ER/NR discrimination line) predicted with MC follows the expectation in the 5-15 PE range of S1. The high number of leakage events agrees also with the results from AmBe calibrations, where the statistical fluctuations of the detector response predicted with MC were bigger than in the data. As a consequence, the ER band reproduced via MC would be affected by greater statistical fluctuations, and the leakage events, calculated with respect to the rejection lines obtained by the data, would be automatically higher.

Finally, a MC-Data comparison of the ER band has been performed also with tritium calibration data. The mean values of the discrimination parameter $\log_{10}(S2_b/S1)$ are very similar in the data and MC, while the fluctuations are smaller in the data case and decrease with S1. Again, the bigger fluctuations in the ER band predicted with MC agree with the fact that leakage events calculated by ^{232}Th simulations results are more numerous than in the expected one.

Tritium calibrations allowed us also to test the MC in reproducing the Combined Energy Scale, important for the analysis: it consists in reconstructing the energy by using both S1 and S2 signals. The agreement between MC and data (and real energy spectrum) is very good above 5 keV, supporting the validity of the S1 and S2 combined procedure to retrieve the energy. Moreover, the the MC predictions describe very well the behavior of the detector above 2 keV (bbelow this energy the hardware S2 threshold removes the majority of events), fully covering the low energy region. Also, from the ratio of the event rates in the data to the MC (basic and quality cuts have been applied to the data) we got the total acceptance of the cuts as function of the energy.

The results from MC predictions on the signal fluctuations in S1, S2 and ER band, required to tune the MC model for electromagnetic background to calibration data in XENON100. In particular, we have used data from tritium calibrations. A refined matching between MC and measured data has been achieved within a Bayesian statistical approach. Thus, the photon yield and its fluctuation represent the parameters for the electromagnetic background, which are defined per each bin of energy released in the detector (photon yield map). The phenomenological model used to predict the number of photons and electrons, due to the detector response to impinging radiations, is again NEST. Then, the conversion to photons and electrons into S1 and S2 signals respectively, is closely related to the physics of the detector, following exactly the same steps which have been developed for the MC simulation.

The Bayesian description of the electromagnetic background in XENON100 has been firstly validated through:

1. $\{S1, S2\}$ pseudo-data have been drawn from the likelihood by using a simple rejection sampler. In order to check the auto-consistency of the likelihood, we ensured that the following quantities are the same as those obtained by NEST:

   - anti-correlated S2 *vs.* S1 distribution of 1000 events from a 39.6 keV gamma line,
   - ER band from 5000 events with uniform energy in the range [2,20] keV.

2. Reconstruction of one bin in the light yield map using a MCMC scheme to converge to a posterior distribution of the mean of light yield, while keeping fixed the value for sigma. In this case 10 events have been drawn from the likelihood of S1 and S2, and fed into MCMC.

3. The same as in the previous step, but considering also the sigma of the photon yield as free parameter (20 events have been fed to MCMC in order to converge to a better resolution for the sigma).

4. Reconstruction of the entire photon yield, at 0-50 keV in energy and using 1 keV bin width. In this case we still draw events from the likelihood of S1 and S2 (5 events per each energy bin).

In conclusion, the posterior distributions reconstructed using the S1 and S2 signals separately present a worse resolution than that obtained using both S1 and S2, as expected. All three distributions include the true value, which means the Bayesian procedure is working well and we have been able to proceed with tuning the light yield map by using data from tritium calibrations. Thus, the posterior distribution of the photon yield has been retrieved, allowing to improve the NEST model. The results provide new information that is relevant to the design, operation and calibration of future liquid xenon based dark matter detectors; a dedicated paper is in preparation. Moreover, the photon yield extracted from this work is currently used to predict the electromagnetic background in XENON1T.

The XENON1T experiment has been meant to improve the sensitivity to WIMP interactions set by the previous XENON100 by two orders of magnitude. In order to reach such sensitivity, all sources of background have been minimized. In particular, the TPC is located inside a cylindrical tank filled with ultra pure water, that acts as a passive shield against the rock radioactivity (low energy gammas and neutrons) and as a Muon Veto (muons inducing high energy neutrons). The muon-induced events are tagged by 84 photomultipliers, installed in the water tank, sensitive to the Cherenkov photons emitted by a charge particle passing inside.

The MV system has been taken care of by the author of this thesis since the very beginning, from the installation of the PMTs inside the water tank in 2014, to the hardware setup, calibrations, trigger, *etc.*, and its operation in the final state. This task was as a natural consequence of the work developed in the Master thesis, mainly based on MV PMTs calibration, in air and in water, in a dedicated setup. Among other measurements, a fit on the gain calculated at different PMT voltages, allowed us to find the voltage settings per each PMT in order to have 1 pC as charge of single photoelectron ($6.2{\cdot}10^6$ of gain). An equalized gain is important at the analysis phase, in order to avoid signal corrections due to different PMT gains. Thus, the voltage settings have been used for the PMTs installed in the water tank. From a single photoelectron calibration we have confirmed that the PMTs are equalized in gain, within 10%, and the width of the single photoelectron charge distribution is equal to 37%.

The MV and TPC are meant to be two independent systems, able to run separately, even if the other system is down. A synchronization using muons crossing almost instantaneously MV and TPC has been performed. From the time difference between a TPC event and the closest MV trigger one can clearly see a narrow population of events at around 450 ns. This delay is in agreement with the hardware time for creating a MV trigger. Moreover, the charge distribution of those events in the

TPC looks flat above $\sim 2 \cdot 10^7$ PE, likely due to muons crossing entirely the TPC; their rate is 1.2 μ/hour, in agreement with expectations from MC. From this study we are able to define a MV cut: we conservatively veto a time of 1 ms after a MV trigger (where we expect muon-induced neutrons) and 1 μs before a MV trigger (to reject muons crossing both MV and TPC). The acceptance for this cut is 99.96%

Finally, a muon analysis to tag muon-induced neutron events is part of the results released by the XENON1T Collaboration for the SR0, collecting 34.2 live days of data acquired between November 2016 and January 2017. The MV performance parameters during the SR0 were:

- the MV was active for 95% of the time,
- trigger: $N \geq 8$ PMTs in coincidence above Thr=1 PE in Δt=300 ns time window, with consecutive samples over threshold TOT=1,
- the tagging efficiency for muon events (muons passing into the water tank) is 99.5% and for shower events (muons interacting with the material outside the detector and inducing neutrons inside the water tank) is 43%,
- the residual nuclear recoil background from muon-induced neutrons in SR0 after applying the MV cut is $1.2 \cdot 10^{-3}$ events in 1t FV, with a reduction factor of 2.5,
- given the low MV trigger rate (around 0.35 Hz), the rate of accidental coincidences between MV and TPC (TPC rate is about 5 Hz during ordinary dark matter runs) results in a negligible loss of the live time.

A total of 63 events pass the selection criteria for the WIMP search in 1T fiducial volume (before ER/NR discrimination), but no one has been rejected by the MV cut. Moreover, a further check on the 14 leakage events below the 50% NR discrimination line and inside 1.25T fiducial volume have been performed, but no correlations were found with a MV trigger.

Bibliography

[1] F. Zwicky, *Die Rotverschiebung von extragalaktischen Nebeln*, 1 933, Helvetica Physica Acta 6, 110

[2] K. G. Begeman, A. H. Broeils and R. H. Sanders, *Extended rotation curves of spiral galaxies - Dark haloes and modified dynamics*, 1991, MNRAS (ISSN 0035-8711) 249, 523

[3] J. F. Navarro et al., *A Universal Density Profile from Hierarchical Clustering*, 1997, Ap. J. 490, 493

[4] F. W. Dyson, A. S. Eddington, and C. Davidson, *A Determination of the Deflection of Light by the Sun's Gravitational Field, from Observations Made at the Total Eclipse of May 29, 1919*, 1920, Phil. Trans. Roy. Soc. Lond. A 220, 291

[5] D. Walsh, R. F. Carswell, and R. J. Weymann, *0957 + 561 A, B - Twin quasistellar objects or gravitational lens*, 1979, Nature 279,381

[6] J.[U+2010]P. Kneib, R. S. Ellis and I. Smail, *Hubble Space Telescope Observations of the Lensing Cluster Abell 2218*, Astrophys. J. 471, 2

[7] D. Clowe, A. and M. Markevitch, *Weak lensing mass reconstruction of the interacting cluster 1E0657-558: Direct evidence for the existence of dark matter*, 2004, Astrophys. J. 604, 596

[8] P. A. R. Ade et al., *Planck 2013 results. XV. CMB power spectra and likelihood*, 2013, A&A 571, A15

[9] M. Milgrom, *A Modification of the Newtonian dynamics as a possible alternative to the hidden mass hypothesis*, 1983, Astrophys. J. 270, 365

[10] Jacob D. Bekenstein, *Relativistic gravitation theory for the MOND paradigm*, 2004, Phys. Rev. D 70, 083509

[11] C. Alcock et al, *The MACHO project: Microlensing results from 5.7 years of LMC observations*, 2000, Astrophys. J. 542, 281

[12] Simon D.M. White, C.S. Frenk, and M. Davis, *Clustering in a Neutrino Dominated Universe*, 1983, Astrophys. J. 274, L1

[13] Stephen P. Martin, *A Supersymmetry primer*, 1998, Adv. Ser. Direct. High Energy Phys. 18, 1

[14] F. Kahlhoefer, *Review of LHC Dark Matter Searches*, 2017, Int.J.Mod.Phys. A32, 1730006

[15] W. B. Atwood et al., *The Large Area Telescope on the Fermi Gamma-ray Space Telescope Mission*, 2009, Astrophys. J. 697, 1071

[16] A. Achterberg et al., *First year performance of the IceCube neutrino telescope*, 2006, Astropart. Phys. 26, 155

[17] A. Kounine, *The Alpha Magnetic Spectrometer on the International Space Station*, 2012, Internat. Journ. Mod. Phys. E 21, 300

[18] M. Pato et al., *Complementary of Dark Matter Direct Detection Targets*, 2011, Phys.Rev. D 83, 083505

[19] F. Agostini, *Studio delle interazioni delle WIMP dell'alone galattico*, 2011, Bachelor Thesis

[20] WebElements Periodic Table, www.webelements.com

[21] Thermophysical Properties of Fluid System, webbook.nist.gov/chemistry/fluid

[22] J. B. Albert et al., *Improved measurement of the $2\nu\beta\beta$ half-life of with the EXO-200 detector*, 2014, Phys. Rev. C89(1), 015502

[23] A. C. Hollis Hallet, *Argon, Helium and the Rare Gases*, 1961, Interscience Publishers, vol. I (New York/London)

[24] E. Aprile and T. Doke, *Liquid Xenon detectors for particle physics and astrophysics*, 2010, Rev. Mod. Phys., vol. 82(3), 2053

[25] R. L. Platzman, *Total ionization in gases by high-energy particles: an appraisal of our understanding*, 1961, J. Appl. Radiat. Isot., vol. 10, 116-127

[26] T. Takahashi et al., *Average energy expended per ion pair in liquid xenon*, 1975, Phys. Rev. A12,1771

[27] T. Doke et al., *Performance of a Prototype of Liquid Xenon Scintillation Detector System for Positron Emission Tomography*, 2002, Jpn. J. Appl. Phys. 41, 1538

[28] G. F. Knoll, *Radiation Detection and Measurement*, 2000, John Wiley & Sons, 3rd Ed.

[29] M. Berger et al., ASTAR, Stopping Power and Range Tables for Helium Ions, 2005, physics.nist.gov/PhysRefData/Star/Text/ASTAR.html

[30] M. Berger et al., ESTAR, Stopping Power and Range Tables for Electrons, 2005, physics.nist.gov/PhysRefData/Star/Text/ESTAR.html

[31] J. F. Ziegler, Stopping and ranges of ions in matter, 2011, www.srim.org

[32] M. Berger et al., XCOM: Photon Cross Section Database, 2010, physics.nist.gov/xcom

[33] M. Chadwick et al., *ENDF/B-VII.0: Next Generation Evaluated Nuclear Data Library for Nuclear Science and Technology*, 2006, Nuclear Data Sheets, vol. 107, 2931

[34] J. Jortner et al., *Localized Excitations in Condensed Ne, Ar, Kr, and Xe*, 1965, J. Chem. Phys. 42, 4250

[35] S. Kubota et al., *Recombination Luminescence in Liquid Argon and in Liquid Xenon*, 1978, Phys. Rev. B 17, 2762

[36] N. Ishida et al., *Attenuation Length Measurements of Scintillation Light in Liquid Rare Gases and Their Mixtures Using an Improved Reflection Suppresser*, 1997, Nucl. Instrum. Meth. Phys. Res., Sect. A 384, 380.

[37] V. Solovov et al., *Measurement of the Refractive Index and Attenuation Length of Liquid Xenon for its Scintillation Light*, 2004, Nucl. Instrum. Meth. Phys. Res., Sect. A 516, 462

[38] E. P. De Lima et al., *Fano factors of rare gases and their mixtures*, 1982, Nucl. Instr. Methods 192, 575

[39] S. Kubota, M. Hishida, and J. Ruan, *Evidence for a triplet state of the self-trapped exciton states in liquid argon, krypton, and xenon*, 1978, J. Physics, vol.11, 2645

[40] A. Hitachi et al., *Effect of ionization density on the time dependence of luminescence from liquid argon and xenon*, 1983, Phys. Rev. B 27, 5279

[41] E. Aprile et al., *Response of the XENON100 dark matter detector to nuclear recoils*, 2013, Phys. Rev. D 88, 012006

[42] G. Plante *et al.*, *New measurement of the scintillation efficiency of low-energy nuclear recoils in liquid xenon*, 2011, Phys. Rev. C 84, 045805

[43] W. R. Leo, *Techniques for Nuclear and Particle Physics Experiment*, Ed. Springer

[44] J. Lindhard, V. Nielsen, M. Scharff and P.V. Thomsen, 1963, Mat. Phys. Medd. Dan. Vid. Selsk. 33 10

[45] U. Fano, *Ionization Yield of Radiations. II. The Fluctuations of the Number of Ions*, 1947, Phys. Rev. 72, 26

[46] G. Bakale, U. Sowada and W. F. Schmidt, *Effect of an electric field on electron attachment to sulfur hexafluoride, nitrous oxide, and molecular oxygen in liquid argon and xenon*, 1976, J. Phys. Chem. 80, 2556

[47] A. Hitachi, *Properties of liquid xenon scintillation for dark matter searches*, 2005, Astropart. Phys. 24, 247

[48] E. Aprile et al., *Scintillation response of liquid xenon to low energy nuclear recoils*, 2005, Phys. Rev. D 72, 072006

[49] P. Sorensen and C. E. Dahl, *Nuclear recoil energy scale in liquid xenon with application to the direct detection of dark matter*, 2011, Phys. Rev. D 83, 063501

[50] E. Aprile et al., *Simultaneous Measurement of Ionization and Scintillation from Nuclear Recoils in Liquid Xenon as Target for a Dark Matter Experiment*, 2006, Phys. Rev. Lett. 97, 081302

[51] E. Conti et al., *Correlated Fluctuations Between Luminescence and Ionization in Liquid Xenon*, 2003, Phys. Rev. B 68, 054201.

[52] E. Aprile, et al., *Observation of Anticorrelation Between Scintillation and Ionization for MeV Gamma Rays in Liquid Xenon*, 2007, Phys. Rev. B 76, 014115

[53] J. Angle et al., *First results from the XENON10 dark matter experiment at the Gran Sasso national laboratory*, 2008, Phys. Rev. Lett. 100, 021303

[54] J. Angle et al., *Limits on spin-dependent WIMP-nucleon cross sections from the XENON10 experiment*, 2008, Phys. Rev. Lett. 101, 091301

[55] M. Ambrosio et al., *Vertical muon intensity measured with MACRO at the Gran Sasso laboratory*, 1995, Phys. Rev. D 52, 3793.

[56] E. Aprile et al., *Dark matter results from 225 live days of XENON100 data*, 2012, Phys. Rev. Lett. 109, 181301

[57] J. Seguinot et al., *Liquid xenon ionization and scintillation: studies for a totally active vector electromagnetic calorimeter*, 1992, Nucl. Instrum. Meth. Phys. Res. A 323, 583

[58] E. Aprile et al., *First Dark Matter Search Results from the XENON1T Experiment*, arXiv:1705.06655 (submitted to PRL)

[59] . Aprile et al., *The XENON100 Dark Matter Experiment*, 2012, Astropart. Phys. 35, 573

[60] E. Aprile et al., *The XENON1T Dark Matter Experiment*, in preparation

[61] M. Yamashita et al., *Scintillation Response of Liquid Xe Surrounded by PTFE Reflector for Gamma Rays*, 2004, Nucl. Instr. Meth. Phys. Res. Sect. A 535, 692

[62] E. Aprile et al., *Study of the electromagnetic background in the XENON100 experiment*, 2011, Phys. Rev. D 83, 082001

[63] A. Hitachi et al., *Effect of ionization density on the time dependence of luminescence from liquid argon and xenon*, 1983, Phys. Rev. B 27, 5279

[64] W. Lippincott, et al., *Scintillation Time Dependence and Pulse Shape Discrimination in Liquid Argon*, 2008, Phys. Rev. C, 78, 035801

[65] E. Aprile et al., *Limits on spin-dependent WIMP-nucleon cross sections from 225 live days of XENON100 data*, 2013, Phys. Rev. Lett. 111, 021301

[66] J. D. Lewin and P. F. Smith, *Review of mathematics, numerical factors, and corrections for dark matter experiments based on elastic nuclear recoil*, 1996, Astropart. Phys 6, 87

[67] J. Engel, S. Pittel and P. Vogel, *NUCLEAR PHYSICS OF DARK MATTER DETECTION*, 1992 Int. J. Mod. Phys. E 1, 1

[68] R. H. Helm, *Inelastic and Elastic Scattering of 187-Mev Electrons from Selected Even-Even Nuclei*, 1956, Phys. Rev. 104, 1466

[69] K. Ni, *Development of a Liquid Xenon Time Projection Chamber for the XENON Dark Matter Search*, PhD Thesis (2006)

[70] E. Aprile et al., *Design and Performance of the XENON10 Dark Matter Experiment*, 2011, Astropart. Phys. 34, 679

[71] E. Aprile et al., *Material screening and selection for XENON100*, 2011, Astropart. Phys. 35, 43

[72] E. Aprile et al., *First Axion Results from the XENON100 Experiment*, 2014, Phys. Rev. D 90, 062009

[73] E. Aprile et al., *Exclusion of Leptophilic Dark Matter Models using XENON100 Electronic Recoil Data*, 2015, Science 349 no. 6250, 851

[74] E. Aprile et al., *Search for Electronic Recoil Event Rate Modulation with 4 Years of XENON100 Data*, 2017, Phys. Rev. Lett. 118, 101101

[75] E. Aprile et al., *XENON100 dark matter results from a combination of 477 live days*, 2016, Phys. Rev. D 94, 122001

[76] E. Aprile et al., *Lowering the radioactivity of the photomultiplier tubes for the XENON1T dark matter experiment*, 2015, Eur. Phys. J. C 75, 546

[77] E. Aprile et al., *Conceptual design and simulation of a water Cherenkov muon veto for the XENON1T experiment*, 2014, JINST 9, P11006

[78] R. F. Lang et al., *Characterization of a Deuterium-Deuterium Plasma Fusion Neutron Generator*, arXiv:1705.04741

[79] J. Billard, L. Strigari, E. Figueroa-Feliciano, *Implication of neutrino backgrounds on the reach of next generation dark matter direct detection experiments*, 2014, Phys. Rev. D 89, 023524

[80] Geant4, geant4.cern.ch/

[81] S. Agostinelli et al., *Geant4 — a simulation toolkit*, 2003, Nucl. Instr. Meth. Phys. Res. A 506, 250

[82] root.cern.ch/

[83] Szydagis et al., *NEST: A Comprehensive Model for Scintillation Yield in Liquid Xenon*, 2011, JINST 6, P10002

[84] Szydagis et al., *Enhancement of NEST Capabilities for Simulating Low–Energy Recoils in Liquid Xenon*, 2013, JINST 8, C10003

[85] N.E.S.T. Noble Element Simulation Technique, NEST.PHYSICS.UCDAVIS.EDU/SITE

[86] J. Séguinot, J. Tischhauser, and T. Ypsilantis, *Liquid xenon scintillation: photon yield and Fano factor measurements*, 1995, Nucl. Instrum. Meth. A 354, 280

[87] T. Doke et al., *LET dependence of scintillation yields in liquid argon*, 1988, Nucl. Instrum. Meth. A 269, 291

[88] J. Thomas and D. A. Imel, *Recombination of electron-ion pairs in liquid argon and liquid xenon*, 1987, Phys. Rev. A 36, 614

[89] N.E.S.T. Benchmark Plots , nest.physics.ucdavis.edu/site/?q=benchmarks

[90] E. Aprile et al., *Observation and applications of single-electron charge signals in the XENON100 experiment*, 2014, J. Phys. G: Nucl. Part. Phys. 41, 035201

[91] E. Aprile et al., *Response of the XENON100 dark matter detector to nuclear recoils*, 2013, Phys. Rev. D 88, 012006

[92] Analysis of Kr-83m calibration data in run14, xecluster.lngs.infn.it/dokuwiki/doku.php (requires password)

[93] D.P. Gregory and D.A. Landsman, *Average Decay Energy of Tritium*, 1958, Phys. Rev. 109, 2091

[94] D. Foreman-Mackey, D. W. Hogg, D. Lang, J. Goodman, *emcee: The MCMC Hammer*, 2012, arxiv:1202.3665

[95] E. Aprile et al., *Response of the XENON100 Dark Matter Detector to Low Energy Electronic Recoils*, in preparation

[96] D. S. Akerib et al., *Tritium calibration of the LUX dark matter experiment*, 2016, Phys. Rev. D 93, 072009

[97] M. Aglietta et al., *Muon depth-intensity relation measured by LVD underground experiment and cosmic-ray muon spectrum at sea level*, 1998, Phys. Rev. D 58, 92005

[98] M. Ambrosio et al., *Measurement of the residual energy of muons in the Gran Sasso underground Laboratories*, 2003, Astropart.Phys. 19, 313

[99] D.-M. Mei, A. Hime, *Muon-induced background study for underground laboratories*, 2006, Phys. Rev.D 73, 053004

[100] XENON1T Data Acquisition, xenon1t-daq.lngs.infn.it (requires password)

[101] F.Agostini, *Caratterizzazione e calibrazione dei fotomoltiplicatori del sistema di veto di muoni per l'esperimento XENON1T*, 2013, Master Thesis

[102] A. Rocchetti, *Monte Carlo simulation of the XENON1T experiment and first comparison with the Muon Veto data*, 2017, Master Thesis